Design, Construction and Testing of a Six-Component Force Balance for the LNEC Wind Tunnel

Francisco Rei Barata Monteiro Vaz

Thesis to obtain the Master of Science Degree in

Aerospace Engineering

Supervisors: Prof. André Calado Marta
Dr. Fernando Virgílio Pires de Oliveira

Examination Committee

Chairperson: Prof. João Manuel Melo de Sousa
Supervisor: Eng. Fernando Virgílio Pires de Oliveira
Member of the Committee: Prof. Luís Alberto Gonçalves de Sousa

December 2025

To my family and friends,
who may not understand what’s written here,
but always understood why it mattered

Declaration

I declare that this document is an original work of my own authorship and that it fulfills all the requirements of the Code of Conduct and Good Practices of the Universidade de Lisboa.

Acknowledgments

Firstly and foremost, I would like to express my deepest gratitude to my supervisors, without whom this project would not have been possible. To Professor André Marta, for his invaluable expertise, guidance, and insightful advice throughout the development of this project. His passion and dedication, both inside and outside the classroom, have inspired and motivated me to learn and strive for a higher level. To Engineer Fernando Oliveira, for his continuous support, dedication, and practical insight during every stage of this work. Without his vote of confidence and constant encouragement, this project could not have come to life. Additionally, I would also like to extend my gratitude to Professor Luís Eça, who dispite not being a supervisor, unconditionally supported and advised this project throughout its entire duration.

I would like to extend my appreciation to LNEC for making this project possible and for entrusting me with this responsibility. It was through the funding of an LNEC Research Fellowship, within the *Programa de Investigação LNEC Modelação do Comportamento Estrutural - MEstr*, that this project became a reality. I am also grateful to everyone who contributed to bringing this work to life, especially my colleagues and fellow researchers at the Earthquake Engineering and Structural Dynamics Unit.

Among the many people who deserve a special mention, I would like to begin by thanking my friends and fellow researchers Diogo Santos and Lucas Lopes for their help, support, and advice throughout the months we worked together at the wind tunnel. To my colleague Afonso Henrique, for the companionship and for the conversations during long working days.

As this project represents the culmination of my entire academic journey, it would be impossible not to acknowledge those who supported me along the way. To the FST Lisboa team, to all the members I had the pleasure of working with, and especially to the Aerodynamics Department. To my dearest friend Beatriz Lopes, for her patience, laughter, strength, and encouragement throughout this journey. And to all the friends I cannot name individually but who have been an essential source of support and friendship during these past few years.

Lastly, I would like to thank my family and my girlfriend Leonor, not only for their support during this past year but for their unconditional understanding and encouragement throughout my entire academic path. Thank you for your calming presence during sleepless weeks, for giving me strength during difficult moments, and for inspiring me to always exceed my dreams and expectations. I am forever grateful.

Resumo

Os ensaios experimentais continuam a ser fundamentais na investigação em aerodinâmica, sendo os túneis de vento essenciais. O Laboratório Nacional de Engenharia Civil (LNEC) dispõe de túneis de vento que carecem de instrumentação dedicada à medição de cargas aerodinâmicas, o que limita as suas capacidades experimentais. Este trabalho propõe o desenvolvimento e calibração de uma balança aerodinâmica de seis componentes, ampliando as capacidades experimentais do LNEC.

A balança foi dimensionada conforme os requisitos do LNEC, considerando as especificações dos túneis de vento e ensaios típicos. O conceito foi definido pelo Processo Hierárquico Analítico, permitindo a seleção da configuração com base em critérios mecânicos e operacionais. O projeto baseou-se na configuração em plataforma de Stewart, com seis barras instrumentadas que medem as três forças e três momentos aerodinâmicos através das forças axiais. Uma análise de singularidades assegurou a resolução de todas as componentes de carga, e análises analíticas e numéricas validaram o projeto mecânico.

As medições de força foram realizadas com células de carga que associadas a um sistema de aquisição da National Instruments™ e uma interface desenvolvida em LabVIEW™ permite a visualização e registo em tempo real. A calibração foi conduzida em duas etapas: caracterização dos sensores e calibração do sistema pelo Método Ponderado dos Mínimos Quadrados com um modelo de segunda ordem.

Quatro modelos foram testados para garantir a precisão e a fiabilidade da balança, permitindo também detetar várias limitações. A balança apresentou medições precisas e consistentes, modernizando os túneis de vento do LNEC e apoiando futuros estudos aerodinâmicos.

Palavras-chave: Balança aerodinâmica de seis componentes, Aerodinâmica experimental, Ensaios em túnel de vento, Projeto mecânico, Célula de carga, Calibração metrológica

Abstract

Experimental testing remains a key element in aerodynamic research, with wind tunnels playing a crucial role. The Laboratório Nacional de Engenharia Civil (LNEC) operates several wind tunnels which currently lack dedicated instrumentation for aerodynamic load measurements, limiting their experimental scope. The present work focuses on the development of a six-component aerodynamic force balance to enhance LNEC's experimental capabilities.

The force balance was dimensioned according to LNEC's requirements, considering the specifications of its wind tunnels and typical test configurations. The conceptual design was supported by the Analytic Hierarchy Process, enabling a systematic selection of the optimal configuration based on predefined mechanical and practical criteria. The design adopted a Stewart platform configuration, where six sensing bars measure aerodynamic loads through their axial forces. A singularity analysis ensured accurate resolution of all load components, and both analytical and FEM analyses were used to validate the structural design and sizing.

Force measurements were implemented using beam load cells connected to a National Instruments™ data acquisition system. A dedicated interface was developed in LabVIEW™ for real-time visualization and acquisition. Calibration was carried out in two stages: individual load cell characterization and full-system calibration using the Weighted Least Squares Method with a second-order polynomial model.

Four models were tested to ensure the accuracy and reliability of the force balance, while allowing to detect several limitations. The final balance demonstrated an accurate and repeatable six-component load measurement, upgrading LNEC's wind tunnel facilities and supporting future aerodynamic research.

Keywords: Six-component aerodynamic balance, Experimental aerodynamics, Wind tunnel testing, Mechanical design, Load cell instrumentation, Metrological Calibration

Contents

List of Tables

List of Figures

Nomenclature

Greek symbols

α	Angle of attack; Stewart platform parameter.
β	Sideslip angle; Stewart platform parameter.
Δ	Variation.
ϵ	Error.
ζ	Pressure loss coefficient.
θ	Angular measurement.
λ	Scale factor; Quality index.
μ	Molecular viscosity coefficient.
ν	Number of degrees of freedom.
ρ	Density.
σ	Normal stress; Standard deviation.
τ	Shear stress.
ϕ	Roll angle.
χ^2	Chi-squared.
χ^2_ν	Reduced chi-squared.

Roman symbols

A	Area.
a	Top platform side length.
AR	Aspect ratio.
b	Reference length; Wing span; Bottom platform side length.
C	Calibration Matrix.

c	Chord length; Calibration coefficient.
C_D	Drag coefficient.
C_F	Force coefficient.
C_L	Lift coefficient.
C_M	Moment coefficient.
C_m	Pitching moment coefficient.
C_Y	Sideforce coefficient.
d	Diameter.
E	Young's modulus.
F	Generic force. Aerodynamic loads vector.
f	Generic aerodynamic load.
f_s	Sampling frequency.
h	Stewart platform height.
I	Moment of inertia.
K	Effective length factor.
L	Length.
l	Stewart Platform bar length.
M	Generic moment.
P	Stewart Platform bottom pickup point.
p	Pressure.
Q	Stewart platform top pickup point.
R	Sensing bars axial forces vector.
r	Axial Force on a sensing bar.
R^2	Coefficient of determination.
Re	Reynolds number.
$\hat{S}$	Plücker coordinates for a sensing bar.
S	Reference area; Wing area; Function of squared errors.
T	Temperature.

U	Voltage.
u_F	Force measurement uncertainty.
u_M	Moment measurement uncertainty.
$\vec{V}$	Vector of a Stewart Platform bar.
V_R	Calibration uncertainty matrix.
V_W	Sensing bar uncertainty matrix.
W	Weighting matrix.
x_{CP}	Pitching moment coefficient.
xx	X axis.
yy	Y axis.
zz	Z axis.

Subscripts

∞	Free-stream condition.
0	Initial Condition
$buckling$	Related to buckling conditions.
i, j, k	Computational indexes.
m	Maximum value.
x, y, z	Cartesian components.
$yield$	Related to yield conditions.

Superscripts

$\wedge$	Fitted Value.
T	Transpose.

Glossary

AHP	Analytical Hierarchy Process
AoA	Angle of Attack
AWG	American Wire Gauge
AWT	Aeronautical Wind Tunnel
BLWT	Boundary Layer Wind Tunnel
BOM	Bill of Materials
CAD	Computer Aided Design
CBOM	Costed Bill of Materials
CFD	Computational Fluid Dynamics
CFRP	Carbon Fibre Reinforced Polymer
CG	Centre of Gravity
CP	Centre of Pressure
DAQ	Data Acquisition System
DoF	Degrees of Freedom
FEM	Finite Elements Modelling
FS	Full Scale
FST	Formula Student Técnico
GoF	Goodness of Fit
IST	Instituto Superior Técnico
LNEC	Laboratório Nacional de Engenharia Civil
LSM	Least Squares Method
MRC	Moment Reference Centre
NI	National Instruments
PVC	Polyvinyl Chloride
SF	Safety Factor
TDMS	Technical Data Management Streaming
UADinE	Unidade de Aerodinâmica de Estruturas
UI	User Interface
VI	Virtual Instrument

Chapter 1

Introduction

1.1 Motivation

The development of wind tunnels marked a paradigm shift in engineering, enabling the repeated and consistent testing of scale models that would otherwise be impractical. Even with the advent of computational models, wind tunnel testing continues to play an indispensable role in the validation process. It not only accelerates the design workflow but also enables the detection of unforeseen phenomena that computational simulations might overlook.

One of the most significant advantages of wind tunnels is their ability to analyse true aerodynamic loads with minimal interference compared to tests conducted under real-world conditions. To achieve accurate results, it is essential for wind tunnel facilities to be equipped with appropriate instrumentation capable of measuring all relevant aerodynamic forces acting on the tested model.

Wind tunnels serve a wide range of applications, extending beyond the obvious aeronautical and aerospace sectors, where they are used to evaluate the aerodynamic performance of aircraft and rockets, to civil engineering, where they help study the aerodynamic behaviour of buildings and structures. It was within this civil engineering context that the first wind tunnel for the Laboratório Nacional de Engenharia Civil (LNEC) was designed and constructed [1]. However, the absence of an adequate force balance system for this wind tunnel, has limited the scope of several studies. Given the highly specific requirements for such instrumentation, commercial solutions are often excessively expensive or, in some cases, unavailable. Consequently, the most practical approach is to custom-design the proper instrumentation, ensuring it meets the requirements while remaining cost-effective.

As such, the motivation of this thesis is to equip the LNEC wind tunnels with reliable and versatile instrumentation to measure forces and moments on test models. This equipment must not only provide accurate results but also adapt to a wide variety of testing scenarios, enhancing the facility's capabilities.

1.2 LNEC Wind Tunnel Facilities

The design of civil engineering structures can be significantly influenced by fluid-dynamic loads. In particular, extreme wind conditions can be catastrophic for a structure if not correctly anticipated and accounted for. The increasing importance of studying wind effects on buildings and structures since the 1940s, in particular following to the Tacoma Bridge collapse [1], led to advent of Wind Engineering. This field primarily focuses on ensuring the structural integrity of constructions, though aspects such as safety and occupant comfort are also considered.

As the importance of wind engineering grew, the necessity for dedicated facilities capable of studying atmospheric wind phenomena and testing their impacts on structures became evident. LNEC followed up on this demand, establishing a laboratory dedicated to aerodynamic studies. The Structural Aerodynamics Laboratory, *Unidade de Aerodinâmica de Estruturas* (UADinE), currently operates four wind tunnels designed for a broad range of tests. These facilities support diverse applications, from the behavioural study of building structures and the aerodynamic stability of bridges to assessing pedestrian comfort and safety in open spaces. Additionally, some experiments extend beyond civil engineering, including the aerodynamic characterization of aircraft and ground vehicles, wind energy potential assessments, and anemometer calibration.

Among these facilities, the most frequently used is a closed-circuit aeronautical wind tunnel with variable speeds up to $45\,\mathrm{m/s}$, shown in Figure 1.1a. With a closed test section measuring 3 x 1 x $1.2\,\mathrm{m}$, it is primarily used for anemometer calibration and evaluating the aerodynamic properties of buildings, structures, and vehicles. Another tunnel of significant interest is the atmospheric boundary layer tunnel, shown in Figure 1.1b. Aimed at accurately recreating the flow fields and effects of atmospheric winds, this open circuit tunnel has the largest test section of all, with a closed section of 9 x 3 x $2\,\mathrm{m}$.

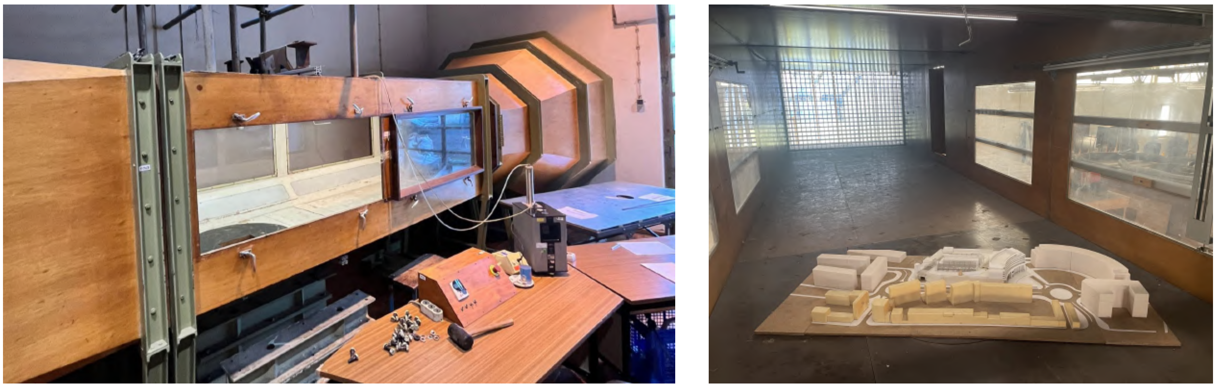
(a) Subsonic low speed aeronautical wind tunnel.

(b) Atmospheric boundary layer wind tunnel.

Figure 1.1: Wind tunnels located at LNEC.

1.3 Objectives and Deliverables

The ability to validate aerodynamic loads on a wind tunnel model is crucial for virtually any experimental wind tunnel test. Therefore, the lack of instrumentation to do so represents a major set back for any wind tunnel infrastructure. This is the case for LNEC's aeronautical wind tunnel. An instrument that is reliable and consistent, measuring multiple of forces and moments, yet versatile enough to allow compatibility with different models, would represent a great leap in the capabilities of this facility. As such, the main purpose of this work is to provide the LNEC wind tunnels with a fully operational aerodynamic force balance that is adequate for its needs.

The adaptability of this instrument to different studies is one of the most important concept and design constraints. Therefore, the force balance needs to be able to measure forces and moments in the six degrees of freedom. In other words, the force balance needs to measure three aerodynamic forces (Lift, Thrust/Drag and Side Force) and three aerodynamic moments (Yaw, Roll, Pitch). The design process for the balance, both on the mechanical and electrical aspects, will follow a requirement based design approach. Once a design is agreed upon, the manufacture and assembly of the force balance need to be executed as well as a calibration process which is crucial to obtain a fully functioning instrument. In addition to the force balance itself, the final product must be comprised of a custom built UI to facilitate the data visualization in real-time and subsequent post processing and a jig to allow the accurate calibration of the force balance.

With this being said, the deliverables for this project are:

- Development of a six-component aerodynamic force balance to be used in LNEC's wind tunnels;
- A user's guide to aid in calibration, set up and use of the force balance.

1.4 Thesis Outline

This thesis is divided into 9 chapters including the present one, introduction. The structure of the remaining chapters is as follows:

Chapter 2 explains the appearence and relevance of experimental aerodynamics, showing relevant modern day situations in which it is applied;

Chapter 3 introduces the concept of force balance, explaining in detail how they work, what are the different design concepts and what previous work has already been made;

Chapter 4 analyses LNEC's wind tunnels and studies several case study experimental test to define the constraints and requirements for the overall design of the force balance using a requirements based design approach;

Chapter 5 details the design of the mechanical components of the force balance. A finite elements model is developed and used to ensure the reached upon design meets all the mechanical requirements;

Chapter 6 presents the different options for the sensors and data acquisition system and determines all the electronics necessary for the final design;

Chapter 7 details a manufacturing and assembly plan for the the force balance, as well as costed bill of materials;

Chapter 8 describes the calibration process for the aerodynamic force balance;

Chapter 9 showcases the capabilities of the instrument with an experimental test using the wind tunnel;

Chapter 10 presents the final conclusions of the project and provides ideas of future work to improve the design and use of the aerodynamics force balance.

Chapter 2

Experimental Aerodynamics

2.1 Historical Background

Since the mid-18th century, when Benjamin Robins experimentally measured the drag of a musket ball and disproved Newton's theory that drag force increases with the square of velocity [2], experimental testing has been recognized as an essential complement to theoretical aerodynamics. Initially focused on ballistics, this field expanded significantly with the development of gliders in the early 20th century and the subsequent rise of powered flight. These advancements required consistent, frequent and reliable aerodynamic testing. In response, various wind tunnels were constructed, which benefited the study of emerging key aerodynamic concepts such as Mach number, Reynolds number, and boundary layer effects. This led to significant progress in both theoretical and experimental methods, which became increasingly crucial as aircraft designs grew more complex and their speeds increased [3].

The introduction of computational approaches in the 1960s further transformed the study of aerodynamics by enabling more detailed and complex analyses. Nevertheless, experimental testing remains indispensable for validating theoretical and computational results, identifying unforeseen phenomena or even accelerating the design process [4–6]. While individual methods—experimental, theoretical, or computational—can be used to solve aerodynamic problems, a combined approach leveraging all three tends to yield the most robust solutions [7].

2.2 Experimental Testing

Several tools have been used to solve aerodynamic problems, such as test flights, wind tunnels, drop tests, rocket sleds, swirling arms, among others [8–11]. In general, it is important for an experimental test to reproduce the real world conditions as closely as possible. Tests such as on-track testing, for ground vehicles, or test flights, for aerial vehicles, are used to exactly replicate the real conditions. However, these can become impractical mainly due to high cost, time constraints or a necessity to isolate some of the variables at play. For these reasons, wind tunnel testing is a widely used form of experimental testing.

The value of experimental tests comes from the data gathered through various types of validation methods. Validation procedures, which are used to determine the behaviour of the model or the airflow, whether it be the forces applied on the model or the flow field, can take many forms. For more rudimentary and relatively inexpensive tests, there is a vast array of qualitative techniques. The most used are wool tufts, flow-vis paint and smoke visualisation [12–14]. Although they tend to not provide the most accurate results, they can be extremely useful, since they can not only indicate the flow alignment, but also show regions of flow separation, or even the point of boundary layer transition, in the case of flow-vis paint. This proves to be an advantage, since the vast majority of quantitative methods cannot evaluate these phenomena. In addition, these techniques can be applied in almost any experimental test, such as on-track testing, as shown in Figure 2.1a.

(a) Wool tufts used on the rear wing of a Formula Student car. Courtesy of FST Lisboa.

(b) Pressure taps inserted inside a building model[15].

Figure 2.1: Examples of qualitative and quantitative validation methods.

While qualitative validation is frequently used in wind tunnel testing, ultimately, any test benefits from the use of quantitative validation procedures. Again, there is a great variety of instruments that can be used. One relatively common example of is the use of pressure taps, as shown in Figure 2.1b, which allow to obtain the pressure profile at the surface of the test model [15–17]. Given enough taps, the data acquired can be used to accurately validate computational models. Though this tool might be extremely useful it is usually expensive and not easily adaptable for different test conditions. As such, the force balance provides a versatile and easy to setup instrument that can be used with a wide range of models. A force balance is an instrument used to measure the loads, forces and/or moments, acting on the test model. There are various types of force balances, varying in degrees of freedom, complexity, adaptability and cost.

2.3 Wind Tunnels

The purpose of a wind tunnel is to consistently provide a steady uniform flow throughout the test section [7]. The types of wind tunnels range from small low speed wind tunnels aimed at studying incompressible flows for aeronautical purposes [18], to large atmospheric boundary layer wind tunnels designed to test civil engineering structures[17], or even transonic, supersonic and hypersonic wind tunnels to test aircraft and rockets in these extreme regimes [3, 19, 20].

All applications require certain forms of validation to ascertain some aspect about the test subject, which in most cases, tends to be a scale model. Usually using a scale down factor, models tend to require less space, are faster to build, cheaper and involve less forces when compared to the real size counterparts [21].

In many civil engineering applications, such as the study of the influence of the wind on buildings, bridges or even antennas, lower speeds ($M < 0.3$) are required, where the compressibility of the air can be neglected. This is also the case for some aircraft or cars which are frequently tested to evaluate their aerodynamic properties. These tunnels, that work in the incompressible regime, are referred to as low speed wind tunnels.

In terms of wind tunnel circuit configurations, there are two basic types of configuration and two types of test sections, where either one can be open or closed.

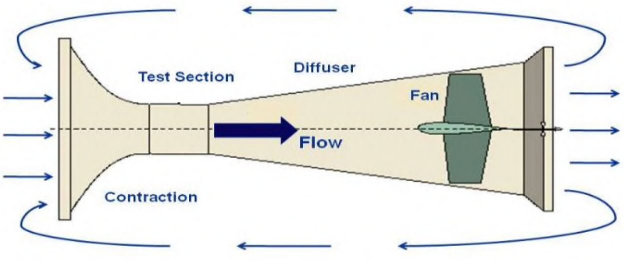

(a) Open circuit. Courtesy of NASA.

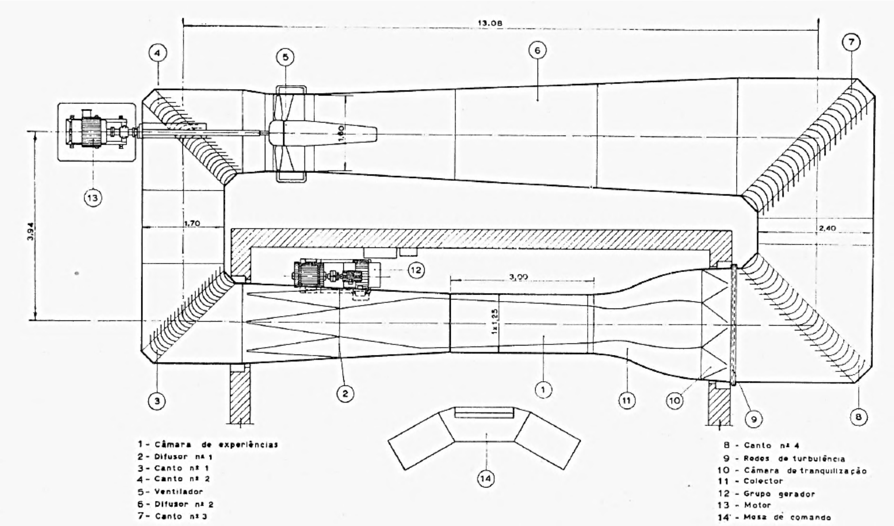

(b) Diagram of the closed circuit wind tunnel at LNEC [1].

Figure 2.2: Types of wind tunnel configurations.

2.3.1 Open and Closed Circuit

A wind tunnel with an open circuit is essentially a straight path with a contraction at the test section [22, 23]. The most important difference with this type of wind tunnel is that it does not forcibly recirculate the air, which depending on the test in question might be an advantage. As shown in Figure 2.2a, the basic layout consists of a converging nozzle placed at the inlet where filters are usually placed to prevent damage to the wind tunnel and screens to improve the flow quality. After the nozzle, a straight portion of constant area acts as the test section, where the flow velocity is consistent throughout. At the end of the tunnel, the diffuser gradually reduces the flow velocity before releasing it into the atmosphere. It is in this section that the fan (or fans) that forces the air though the tunnel is located. This is done in an attempt to reduce the effect of the swirl induced by the fan in the test section. There are advantages and disadvantages that come with this configuration. The major advantage is the reduced construction cost in comparison to closed circuit tunnels, which usually require a dedicated facility to be built. Another advantage is that, since the air is not recirculated from the outlet to the inlet, certain tests, which use of internal combustion engines or smoke to allow flow visualization, to not require a purging of the exhaust. As for the disadvantages, it is noted that these wind tunnels require additional measures to ensure the same flow quality as their counterparts. In addition, open circuit tunnels tend to be notably nosier and less efficient than closed circuit ones [7].

The idea behind a closed circuit is to recirculate the air, moving it from the outlet to the inlet, in attempt to improve flow quality and efficiency of the tunnel [24]. The aeronautical wind tunnel at LNEC [1], shown in Figure 2.2b, is an example of the conventional layout of a closed circuit wind tunnel. Having a similar design to the open circuit tunnel, the difference arises at the outlet, where the flow is redirected, in this case even outside of the building where the test section is located, back to the inlet. It is in this region that the fan is located. This allows the flow to stabilize properly before entering the test section once again. In comparison to the other type of wind tunnel, closed circuit wind tunnels have enhanced flow quality and increased efficiency. This is important for testing facilities that, not only require very precise and consistent results, but are also used with considerable frequency. However, their construction costs are higher and purging exhaust gases and fumes can be problematic [7].

2.3.2 Test Section

The majority of wind tunnel have a closed test section, meaning that the test section is enveloped by solid boundaries for steadier flow and reduced noise. The existence of solid and flat boundaries can also be beneficial for some tests, such as the testing of buildings or ground vehicles. This, however, is not the case for the testing of aircraft or some structures, such as bridges, which are not usually subject to that level of proximity to boundary surfaces.

Open test sections allow the removal of most of the boundaries of the wind tunnel, which provide a more realistic setting for various tests [25, 26].

The shape of the cross section can vary depending on the wind tunnel. A circular shaped section can help prevent flow separations by removing the corners, while a rectangular or polygon shaped one might be more suitable for larger applications, since the placement of the model is facilitated by the existence of a flat floor.

Chapter 3

Force Balances

A force balance is one of the most essential devices in terms of quantitative wind tunnel validation. It enables the measurement of both forces and moments. The decoupling of the forces and moments with a simple structural design is complex and not always achievable. Also, high maximum load capacity and tight accuracy for minimum loads can increase the complexity of the design [7].

For the design to be adequate, a series of requirements must be met. Some of the requirements are given by the wind tunnel characteristics or the type of applications it will be used for. This is the case for the maximum load or the load measurement resolution and sensitivity [7], the number of load components to be measured by the force balance, from one to six, or a constraint on the concept of the force balance, whether it be mechanical or on the load sensors.

3.1 Design Concepts

The general concept of a force balance lies in having a rigid structure attached to the model, either internally or externally, by the use of support structures, which can incorporate load sensors that will measure the loads applied on the model.

3.1.1 Internal Configuration

The internal force balances are placed inside the test model. As such, this concept has to work around a restricted space within the model. Their main disadvantage lies in the complexity of the design that has to be mostly custom made for every model. However, this can prove useful since a force balance that can be custom made for a single model can benefit from having greater range for some loads or a more sensitive reading for others [7]. Another advantage is that they aim at minimizing the interaction with the flow which is something external designs cannot. Although some applications can be found in subsonic testing, the vast majority of internal balances are in transonic and supersonic wind tunnel tests [27].

There are many ways in which to devise an internal balance. In general, the main differences between them lie in the sensors used. One of the approaches is the usage of piezoelectric elements, which provide a measurement of the force applied on the sensor. These provide a good frequency response and are remarkably stiff, reducing the required deformation of the balance to measure the loads [28]. However, they are unreliable to measure static loads. The second option, and by far the most used, are strain gauges, which require deformation of some parts of the balance to calculate the loads [29]. They are commonly used in monolithic balances, which are made from a single part and are designed to concentrate strain in certain regions where the strain gauges are placed.

3.1.2 External Configuration

The external force balance concept is by far the most used in subsonic wind tunnel applications. In comparison to the internal balances, the external ones are more versatile, being easily adapted to different models. As the name suggests, the balance is external to the model, being placed inside the test section or, if possible, outside the wind tunnel using a support structure to attach to the model.

The concepts can be divided into four categories based their primary load carrying members [7]: wire, platform, yoke and pyramidal.

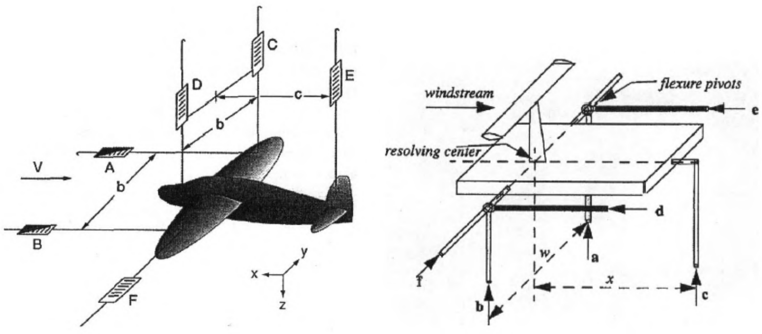

(a) Wire Balance.

(b) Platform Balance.

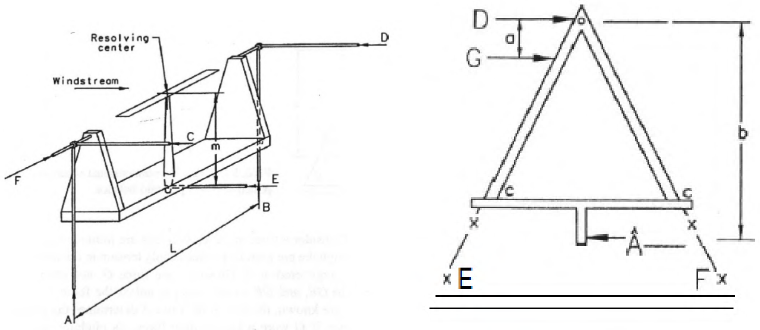

(c) Yoke Balance.

(d) Pyramidal Balance.

Figure 3.1: Basic categories of external force balances [7].

Wire Balances

The wire force balances are one of the earliest types of balance. Multiple wires are connected to the model and to a scale, as illustrated in Figure 3.1a. The force measurement can be taken using the scales and, given enough wires and scales, the six aerodynamic loads can be determined [30].

Despite being easy to set up and relatively inexpensive, this type of force balance has mostly fallen out of use because the wires cannot carry compressive loads. This means that every wire needs to be under tension at all times for the measurement to be accurate. This evidently hinders the test, since the placement of the wires has to be carefully planned. Other common problems were the frequent change in the models attitude due to deflections, the snapping of the wires and the added drag from the wires.

Platform Balances

In contrast to wire balances, the remaining types use a support structure to mount the models. This is beneficial since it allows the remaining parts of the device to be placed outside of the wind tunnel, increasing accessibility to the instruments, reducing the influence on the airflow interacting with the model, among others. In addition to this, since the models are not permanently attached to the wind tunnel, the support structure allow for quicker adjustments in terms of position or angle, such as the angle of attack or the yaw angle.

The platform force balance is one of the most used options. It has a platform that is supported by multiple legs, upon which a support structure can be mounted. The amount of legs and their configuration can vary but the most usual approach is to have three legs supporting the platform, as shown in Figure 3.1b, which allows the measurement of up to six loads [31].

A variation of this balance concept is the Stewart platform. This platform is commonly used as a parallel manipulator with six degrees of freedom, as shown in Figure 3.2, used for equipment such as seismic shaking tables [32] and flight simulators. It is constituted by two platforms, one fixed and one mobile, connected by six linear actuators. Since the actuators are non collinear, the top platform can move in all six degrees of freedom. To transform the manipulator into a load measuring device, the linear actuators must be replaced with sensing arms, equipped with load sensors [33–35].

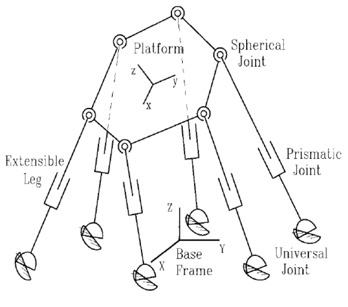

Figure 3.2: Stewart platform manipulator [36].

This concept has some clear disadvantages. For one, for the resolving centre of the mathematical equations to be the on the model, they need to take into account the position and dimension of the support structure. If this is not taken into account, the resolving centre is placed on the platform, as in Figure 3.1b, and some forces will inevitably contribute to some of the moments, which is undesirable. In addition to this, there is a very tight coupling of the loads, since moments will be given as the difference of forces. In the case of small moments and large forces, this can lead to large uncertainties.

Yoke Balances

The yoke balance in Figure 3.1c consists of a long main structure, the yoke, which supports the support structure that holds the model. The yoke can revolve around an axis that passes through the centre of the wind tunnel. This attempts to overcome some of the issues found in platform balances. Mainly, this configuration placed the resolving centre at the centre of the wind tunnel, where the model is placed.

However, yoke balances are larger and need to span the entire test section. In comparison to the platform balance, this means that there is an increased potential for deflections when in operation which hinders the results [7, 37].

Pyramidal Balances

The pyramidal balance concept, illustrated in Figure 3.1d, is an improvement on the two previous balances. By implementing 6 separate measurement units, one for each load, the pyramidal balance can completely decouple the forces and moments, since each load is given by a single measurement, reducing errors and uncertainties. In addition to this, the resolving centre, as in the yoke balance, is placed exactly in the centre of the wind tunnel [38].

However, the design is more complex, since it aims at separating the forces and the moments. This means that not only the manufacturing, but also the calibration, are similarly complicated. In addition to this, slight deformations and deflections have a much greater impact on the results of the moments [7].

3.2 Sensors

Besides the main mechanical structure, a force balance requires a set of sensors in order to measure the required loads. Force balances can be split into groups based on the types of measuring devices. The most common type of force transducers fall into the electrical category, meaning they require an electrical signal to measure the load.

3.2.1 Strain Gauge

Strain gauges are one of the most basic types of force transducers, which directly relate the strain of the sensor to its electrical resistance [39]. The most common type of strain gauge, and arguably the simplest, are the metal strain gauges. As any electrical conductor changes its resistance with the introduction of mechanical stresses, it is possible to devise a sensor that complies with the strain of the body where the forces are acting in order to measure its strain and, as a consequence, the applied force.

Figure 3.3 shows the typical configuration of a metal strain gauge which consists of a measuring grid (b) made out of a thin sheet of metal, held in place by a carrier substrate (a). The gauge is designed to only be affected by strain in one direction, horizontal in the case of Figure 3.3. As the sensor must have the same strain as the surface of the object it is measuring, a very close bonding is needed between the two surfaces.

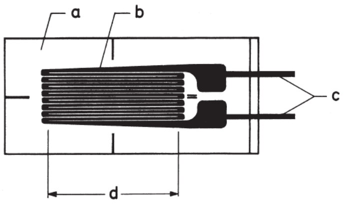

Figure 3.3: Etched metal-foil strain gauge [39].

Although the strain gauge has the ability to measure the strain on the surface of an object when subject to a force, it still presents some challenges. For one, the changes in resistance are small and require a robust and effective method to amplify the signal before measuring it accurately. On the other hand, a strain gauge simply measures strain in a certain location which, for many applications where a measurement of force is required, is insufficient. The solution for the latter problem is to arrange a series of strain gauges into a force transducer known as a *Wheatstone Bridge*.

3.2.2 Wheatstone Bridge

The Wheatstone bridge is a type of circuit that is used to compare resistances and detect small changes in resistance [40]. The basic design of a full bridge is composed of four resistances (R_1 to R_4) arranged in a diamond shape, according to Figure 3.4. The diagonals of the circuit represent the excitation ports and the measurement ports. In the excitation ports, a known voltage U_E is applied and the output of the circuit is measured at the measurement ports by the voltage U_A. As such, the output of the circuit is only dependent on the ratio of the resistors, R_1/R_2 and R_4/R_3.

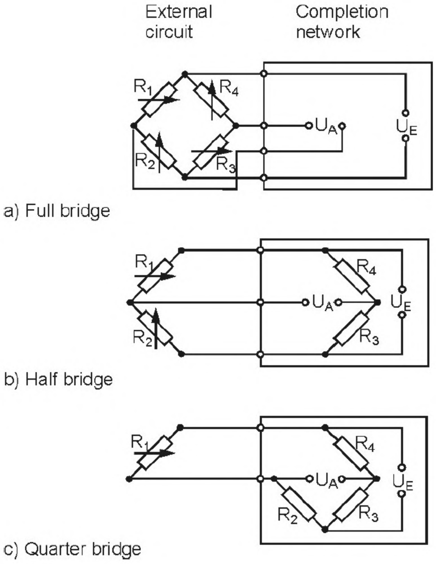

Figure 3.4: Different Wheatstone bridge configurations [40].

Considering the ratio between the output and input voltages, the general equation for the circuit can be written as the ratio

$$\frac{U_E}{U_A} = \frac{R_1 R_3 - R_2 R_4}{(R_1 + R_2)(R_3 + R_4)} \tag{3.1}$$

If the resistors have variable resistance, as strain gauges do, the equation can be rewritten as a function of the relative change in each resistance. If the resistors are substituted for strain gauges, the relative change can be linked to the strain .

The practical application of the Wheatstone bridge with strain gauges is in experimental stress analysis. Depending on the problem at hand, the strain gauges can be positioned in adequate orientations to measure tension, compression, bending or torsion. In addition to this, some measurements do not require as many as four strain gauges. Therefore, the circuit can be adapted using fixed resistors, as shown in Figure 3.4. In the case where no strain gauges are replaced by fixed resistors, the circuit is called a full bridge circuit. The other two types of configurations are referred to as half bridge and quarter bridge, which as the names imply, use two and one strain gauges respectively.

3.2.3 Load Cells

The term load cell is used to describe a device that is essentially a force transducer, which can convert a force or moment into an electrical signal to be measured. In contrast with strain gauges, which have to be attached to the body to be studied, load cells are pre-made devices that, by themselves, can measure forces and output an electrical signal. Therefore a load cell can be integrated into a design of a force balance in a much more seamless manner than strain gauges.

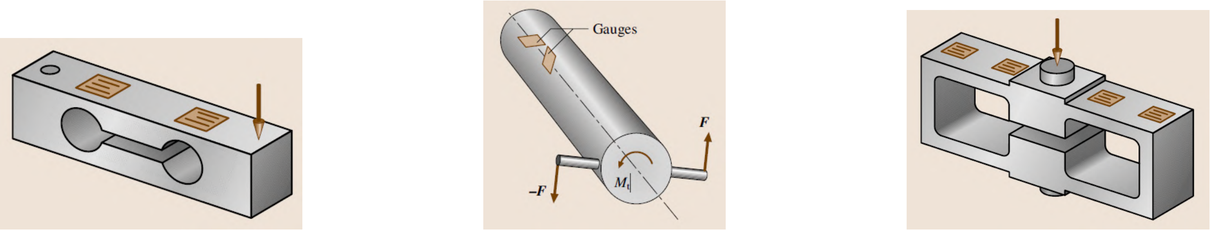

(a) Bending-type load cell.

(b) Shear-type load cell for torque measurement.

(c) Tension and compression load cell.

Figure 3.5: Types of single-force load cells [41].

There are different types of load cells, depending on the type and number of loads to be measured and how the electrical signal is produced. A large majority of load cells employ resistive strain gauges in order to register the loads applied on the cell and are designed to measure a single type of load. The different types of loads that are usually measured using single-force load cells are: Bending, Shear and Tension/Compression, as shown in Figure 3.5.

All of these types of load cells require elastic deformation of the structure to measure the loads. In some situations, such as the study of a unsteady phenomena, this fact might be undesirable. This led to the necessity for more rigid load cells which require less deformation, a requirement that is met by piezoelectric load cells.

The piezoelectric effect, shown in Figure 3.6a, is characterized by the generation of electric potential in a substance as the pressure applied on said substance changes [42]. Materials that have piezoelectric properties, such as quartz (SiO_2), other crystals (ZnO, GaN and InN) or certain ceramics, are made out of ions or polarized molecules and have structures with no centre symmetry. When a load is applied to the material, its internal structure deforms, which creates a polarization of the entire crystaline structure [41]. A typical piezoelectric load cell usually has an annular shape, containing a quartz plate located between two steel plates. As the load cell is compressed, a voltage can me measured between the two steel plates. Depending on the type of load, more disks can be added in order to measure shear stresses, as shown in Figure 3.6b.

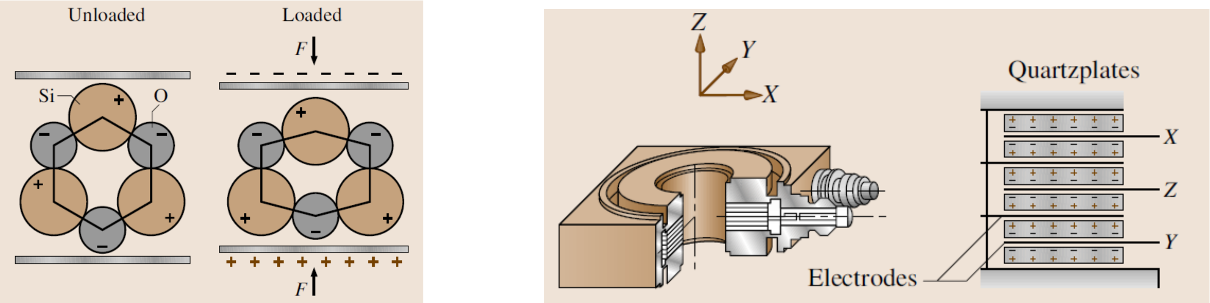

(a) Crystaline structure with piezoelectric effect.

(b) Three component piezoelectric load cell.

Figure 3.6: Piezoelectric force measuring [41].

Although this type of load cells remove the elastic deformation problem, they are considerably more expensive than conventional strain gauge load cells, and they have remarkably larger errors when measuring static loads. When a static load is applied to the sensor, the induced charge reduces exponentially with time [43]. Despite attempts to correct and minimize these problems, conventional strain gauge sensors still remain the preferred choice to measure static loads, while piezoelectric sensors present major advantages in measuring dynamic or quasistatic loads.

3.3 Data Acquisition Systems

Data acquisition refers to the process of taking analogue signals and converting the information into a digital form to be processed by a computer [44]. This process is crucial for any sensor and a force balance is no exception. Regardless of the sensors used for the load measurement the output is always a voltage which does not directly translate into a force measurement. Hence, the analogue signal must be transformed into digital to be processed by a computer, firstly, to provide the load measured by the sensor and, secondly, to accurately combine all the measured loads and calculate the overall aerodynamic forces acting on the model.

The Data Acquisition System (DAQ) is one of the most important systems of the entire force balance, communicating between the sensors and the computer, where the final results are calculated and presented. Besides transforming the analogue signal into a digital signal, the DAQ must also condition the signal, removing unwanted noise, and amplifying it. These steps are crucial and present an additional layer of complexity to the system, since the introduction of errors is possible, yet undesirable.

There are various commercial options to be employed as a DAQ in load measurement applications. One example is the *NI-9237*, from National Instruments™, shown in Figure 3.7. These options present various advantages, namely the accuracy and the ease of communication to a computer through a custom UI. Alternatively, custom DAQs can provide cost reduction and for customisation of its parameters.

Figure 3.7: DAQ from National Instruments™, *NI-9237*.

Chapter 4

Requirements

To properly define the requirements for the force balance, it is essential to understand the specific needs it must address. The most critical aspect of this step is identifying the testing scenarios in which the force balance is expected to operate, ensuring that the design accounts for these conditions. Once the requirements are defined, it is important to verify and validate if the set requirements at multiple steps along the project, since a vast number of projects fail due to lack of requirements or non compliance with the defined requirements.

The full requirement list, along with the respective verification and validation processes, are shown in table A.1. The following sections intend on providing an explanation for some of the requirements.

4.1 Concept Selection

4.1.1 Analytical Hierarchy Process

A force balance can present various different concepts, as shown previously in Section 3.1.2. Each of these concepts has strong points and clear disadvantages when compared to other. Although there are multiple processes to determine the most appropriate concept, the Analytic Hierarchy Process (AHP) presents a methodical process of ranking multiple options and, therefore, is the most widely used. An AHP is a multiple criteria decision-making tool which boils the complexity of the problem down to simple pairwise comparisons, combining both quantitative and qualitative measurements [45]. In addition to comparing the multiple choices in a pairs, the process also requires the evaluation criteria to be evaluated in a similar fashion, leading to a set of weighted criteria which enhance the final selection process.

For the selection process of the force balance concept, the AHP will be based on the selection process conducted by Fernandes [33], which also intended to deciding on a concept for a force balance. The AHP evaluates six different balances with different design concepts: platform, rotating platform, pyramidal, pyramidal platform and two innovative design concepts. These options are evaluated according to twelve criteria divided in two areas: construction and operation. These criteria are as follows:

Construction

- Robustness (A)
- Simplicity (B)
- Fabrication (C)
- Instrumentation (D)
- Structurally adaptable (E)
- Innovative design (F)
- Cost (G)

Operation

- Wind tunnel attachment (H)
- Support versatility (I)
- Measurement accuracy (J)
- Force and torque decoupling (K)
- Results processing (L)

The pairwise evaluation process in an AHP, is usually conducted using values ranging 1 to 9, where 1 represents equal importance and 9 represents extreme importance. In the case that a criteria or an option presents less importance in a pairwise comparison, the inverse should be used (i.e. $\frac{1}{9}$ represents extremely less important). Using this grading system, the criteria pairwise comparison matrix can be constructed, as shown in Table A.2, as well as the resultant weight of each criteria. In comparison to the AHP conducted by Fernandes [33], this pairwise comparison was adjusted. In particular, changes were made to increase the weight of certain criteria, such as the robustness, the structural adaptability and the wind tunnel attachment. For example, to evaluate the robustness criterion, it was compared with each of the other criteria. It was evaluated with a 6 when compared to the innovative design criterion, since the former was considered to be significantly more important than the later. The evaluation of each criterion and each force balance is presented in Appendix A.

The results of the process are shown in Figure 4.1. Despite the changes in the criteria, the platform balance still presents the maximum score, thus it was selected as the design concept.

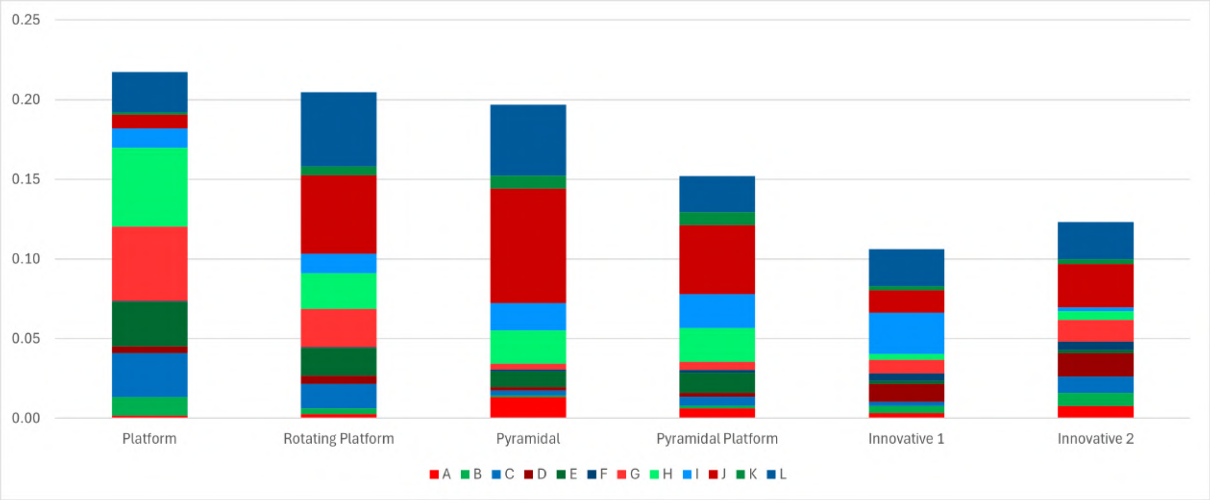

Figure 4.1: Results of the AHP.

4.1.2 Stewart Platform

As discussed in Section 3.1.2, there are multiple types of platform force balance designs. One of the aforementioned designs is the Stewart platform, which is an adaptation of a parallel manipulator into a load sensor. The design of the Stewart platform was originally proposed as a parallel manipulator allowing motion of the top platform in all six degrees of freedom with precise positioning and good dynamic performance in high load carrying scenarios [36]. By replacing the actuator arms with load sensing arms, the force balance can retain the precision that is characteristic of the manipulator, while keeping the simplified design that is characteristic of platform balances.

Over the years, there have been multiple variants of Stewart platforms. These can be divided in three general types, shown in Figure 4.2, where each number specifies the number of vertices of each platform. In the case of the type 3-3, which is the simplest design in a conceptual sense, both platforms have the shape of equilateral triangles where each vertex connects to two distinct bars though a spherical joint. However, this design poses some complications in terms of construction, since each vertex would require a double spherical joint to link to each bar. This exact issue also arises in the 3-6 platform, which was one hexagonal platform while the other keeps the triangular shape. This problem brings about the need for the type 6-6 platform, which is a generic case that represents any manipulator, or balance, with six vertices on each platform.

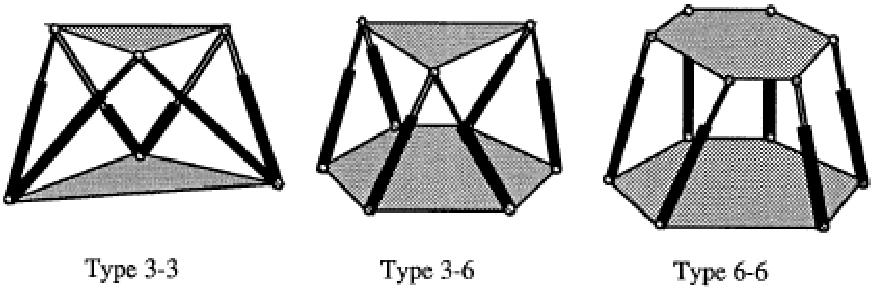

Figure 4.2: Different types of Stewart platforms [46].

The design will be a 6-6 platform derived from the ordinary 3-3 design, as shown in Figure 4.3. Considering a generic type 3-3 platform, the configuration can be determined by three variables. Two of the variables, a and b, correspond to the length of the sides of the top and bottom platforms, respectively. Variable h relates to the height between both platforms. Using the same notation as in the diagram, it is possible to relate any generic platform to a simplified 3-3 platform using only two additional coefficients, α and β. When multiplied by the side of the respective platform, these variables correspond to the separation between the two new vertices and the original position of the vertex. It is important to note that any generic Stewart platform can be determined using these variables, since a type 3-3 only requires both coefficients, α and β, to be null and a 3-6 platform requires only one of the coefficients to be null.

4.2 Wind Tunnel Specifications

4.2.1 Aeronautical Wind Tunnel (AWT)

The aeronautical wind tunnel at LNEC is a low speed closed circuit wind tunnel [1]. Its test section has an octagonal prism constant cross sectional area of $1.311\,\mathrm{m}^2$ and length of $3\,\mathrm{m}$. The detailed dimensions

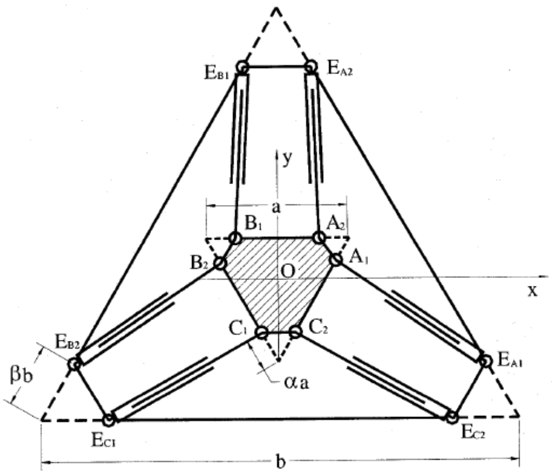

Figure 4.3: Type 6-6 platform device with corresponding notation [47].

and respective pressure losses are shown in Table 4.1, where the index i represents the notation of Figure 2.2b.

Table 4.1: AWT detailed dimensions and pressure loss coefficients [1].

i	Designation	L_i [m]	A_i [m²]	ζ_i
0	Test section	3,00	1,311	0,028
1	Between corners 1 and 2	1,54	2,270	0,009
2	Between corners 3 and 3	0,64	4,524	0,003
3	Tranquilising chamber	0,70	4,524	0,003
4	Diffuser 1	—	2,010	0,146
5	Diffuser 2	—	2,010	0,166
6	Corner 1	2,40	2,270	0,062
7	Corner 2	2,80	3,402	0,062
8	Corner 3	3,30	4,524	0,062
9	Corner 4	3,80	4,524	0,062
10	Between corner 2 and the turbine	0,45	2,270	0,093
11	Collector	2,25	2,270	0,009
12	Protection net	—	2,270	0,375
13	Turbulence net	—	2,270	0,375
14	Joints, leaks, etc.	—	1,131	0,021

The wind tunnel has two distinct ways of controlling the air speed, either by changing the fan motor's frequency or by varying the angle of attack of the fan blades. The latter has to be done manually through the inside of the tunnel, in what can be considered a cumbersome process. Hence, the speed control is most frequently done by changing the frequency in an open loop fashion, requiring the operator to manually change the input frequency of the turbine's motor, calculate the air speed using a pitot tube and adjust the frequency once again to correct any error. The curves relating turbine rotational speed to the air speed for various blade angles are shown in Figure 4.4, where the maximum air speed appears to be slightly higher than $50\,\mathrm{m/s}$. However, it is important to note that the test in question [1] was performed shortly after the tunnel was built and with an empty test section. This is relevant, since a large model with a large blockage ratio, the maximum air speed can only consistently reach $40\,\mathrm{m/s}$ at most. For this reason, this air speed will be considered to be the tunnel's maximum for all subsequent calculations.

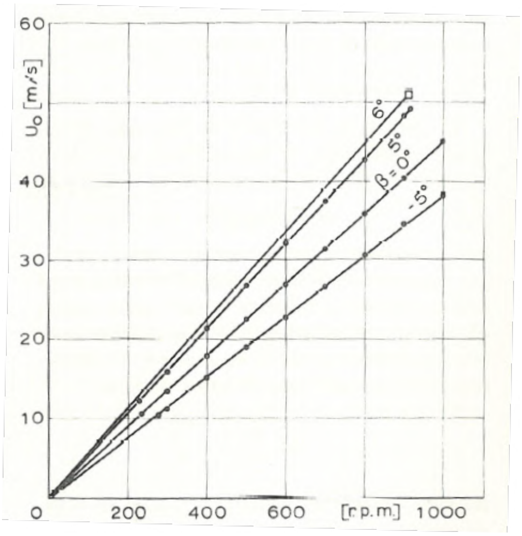

Figure 4.4: Wind speed with various turbine speeds and blade angles. [1].

As the goal of this wind tunnel is to generate a uniform velocity field in the test section, an important measurement to be considered is the turbulence. This is represented by the maximum velocity variation in a certain cross section. According to the study conducted in [1], the turbulence of LNEC's aeronautical wind tunnel is on the order of 1%.

4.2.2 Atmospheric Boundary Layer Wind Tunnel (BLWT)

The boundary layer wind tunnel is the largest wind tunnel found at LNEC [48]. This open circuit wind tunnel has a closed test section with a constant rectangular cross section of dimensions $3 \times 2\,\mathrm{m}$ and length $9\,\mathrm{m}$. The tunnel has six $11\,\mathrm{kW}$ turbines placed downstream of the test section. These are evenly distributed at the discharge interface to the atmosphere, where two of the turbines, the ones aligned with the tunnel central axis, are controlled using a variable frequency controller, allowing the velocity to be controlled up to $18\,\mathrm{m/s}$.

The test section has a rotating platform on the floor to allow multiple angles of incidence and the ability to change the angle of the test section's ceiling to control of the pressure gradient across the test section.

4.3 Reference Frame

It is important to define a reference frame according to which all the forces and moments will be measured. The origin is important since it defines the point about which the moments are calculated, the moment reference centre (MRC). Depending on the experiment it might be useful to place this point on different locations, such as the centre of gravity (CG) of the model. However, since the goal is to standardize the reference frame, the origin was set regarding only the balance itself, as the attachment point of the balance to the model.

As for the axis orientation, according to international standards, ISO 1151/2 which refers to the motion of aircraft and the atmosphere relative to the Earth, the xx axis is aligned with the flight path of the aircraft. Transposing the same principle to the wind tunnel, the xx axis can be aligned with the air flow, pointing upstream. By forcing the zz axis to be vertical, there are two different options for the orientation of the reference frame, as shown in Figure 4.5. The advantage of the first reference frame in Figure 4.5b lies in the fact that it is used as a convention in aircraft, where a positive angle of attack (AoA) represents a positive angle around the yy axis. Additionally, all of balance's components present positive values on the zz coordinates. However, the reference frame in Figure 4.5a presents an upward pointing zz axis. Since the latter is more conventional and more intuitive, since the zz axis physically points upwards, this was the chosen reference frame.

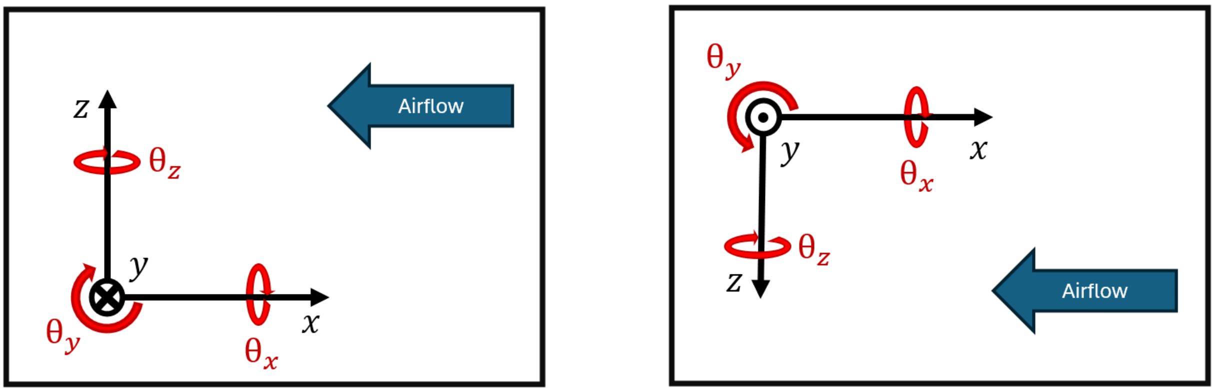

(a) Chosen reference frame.

(b) Another feasible reference frame.

Figure 4.5: Possible reference frames according to the predetermined criteria.

As the reference frame has six degrees of freedom, three directions and three rotations, there is a need to define the six loads, three forces and three moments related to these degrees of freedom. Table 4.2 presents the different notations and name of each load.

Table 4.2: Axis with respective forces and moments components.

Degree of Freedom	Respective Load	Load Designation
x	F_x	Thrust, Drag
y	F_y	Side Force
z	F_z	Lift, Downforce
θ_x	M_x	Rolling Moment
θ_y	M_y	Pitching Moment
θ_z	M_z	Yawing Moment

4.4 Testing Scenarios

The design of the force balance must be suited to the testing conditions and loads it is expected to measure. For this reason it is necessary to define what the expected testing scenarios are and extrapolate the load cases to determine the requirements. The load cases under analysis must be limiting scenarios, in which the mechanical or sensing limits of the balance should operate. Since all of the load cases were achieved through analytical calculations, it is important to define the standard operational conditions of the tests, which are defined in Table 4.3 that are considered on the testing scenarios.

Table 4.3: Standard air conditions.

Density (ρ)	Pressure (p)	Temperature (T)	Viscosity (μ)
$1.225kg/m^3$	$101325Pa$	$288K$	$1.81 \times 10^{-5}kg/m \cdot s$

In order to calculate the aerodynamic loads, either forces or moments, the aerodynamic coefficients must be defined. These are adimensional values, constant for each body and dependent on it's shape. Given these coefficients, the values for the forces and moments are calculated by the usual aerodynamic equations, 4.1 and 4.2, where F and M represent a generic force and moment, respectively. When the forces are not directly applied at the point where the moments are being calculated, an additional moment will occur as result of the force F and the arm r, i.e. the vectorial distance between the point where the moments are calculated and the force's application point, as stated in equation 4.3.

$$F = \frac{1}{2}\rho U_\infty^2 C_F S \tag{4.1}$$

$$M = \frac{1}{2}\rho U_\infty^2 C_M S b \tag{4.2}$$

$$\vec{M} = \vec{r} \times \vec{F} \tag{4.3}$$

In total, five testing scenarios were considered to establish the testing conditions: Flat Plate, Half Wing Model, Formula Student Model Car, Suspension Bridge and Communications Antenna.

4.4.1 Flat Plate

A majority of the experimental tests that are run on LNEC's wind tunnels are of large structures, such as bridges and buildings. Even using a scale down factor, the models still tend to be large in comparison to the test section. Therefore it was considered an extreme case in which a flat rectangular plate is positioned perpendicular to the airflow, maximizing the drag coefficient.

The size of the plate, for the AWT, was determined taking into consideration the largest models used in previous tests, which tend to be bridge sections with a maximum blockage ratio of 30%. This means that, using the test section area found in Table 4.1, the area of the plate can be calculated. In order to define the proportions of the rectangle, it was defined a length of $1m$ for the plate, as in a previous suspension bridge study [49], and the height was set accordingly (see Figure 4.6). The same process was used to define the flat plate to be used in the BLWT, using the same rectangle proportions to define the length and height.

The resultant forces and moments are calculated assuming a C_D of 1.28 [50] and take into account the maximum air speed of either wind tunnel in order to achieve the maximum aerodynamic loads. It

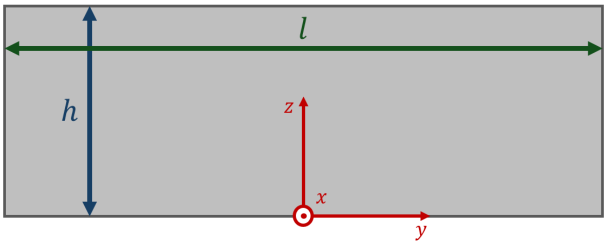

Dimension	AWT	BLWT	Units
Test Section Area	1.311	6.000	m^2
Blockage Ratio	0.300	0.300	-
Flat Plate Area	0.393	1.800	m^2
Length (l)	1.000	2.139	m
Height (h)	0.393	0.841	m
Drag Coefficient (C_D)	1.280	1.280	-

Figure 4.6: Flat plate dimensions for both wind tunnels.

is important to note that, although a flat plate would naturally only generate drag, the presence of a moment, M_y, in the final load cases is the result of the arm between the balance attachment point and the plate's centroid. As shown by the origin in Figure 4.6, the attachment point is at the bottom edge of the plate. Since the drag force is applied at the centre of pressure, in this case the centroid of the rectangle, this causes the drag force to generate a moment at the attachment point. The results from these calculations show that the testing scenarios in each wind tunnel is a maximum, one in terms of force, F_x, and the other in terms of moment, M_y, as shown in table 4.7.

4.4.2 Half Wing Model

One common experimental test that is conducted in aeronautical wind tunnels is the test of aircraft wings to evaluate the aerodynamic loads and detect phenomena such as flutter or flow separation for various speeds and angles of attack. Usually, when testing a wing, the model is only of the half wing, attached by the root, forcing the results to be extrapolated for the full wing. To define the load case, the parameters of the wing have to be set, such as the dimensions and the wing profile as well as its aerodynamic characteristics. To achieve a limiting scenario it is important to choose a profile with a high coefficient of lift, such as those found in the wings of light weight STOL aircraft. Therefore, the model will be based around these type of aircraft, whose wings tend to have a constant cross section, no dihedral angle nor any sweep angle and low aspect ratios.

To determine the wing profile, an analysis was conducted between two different wing profiles: the NACA 2412, which is the wing profile at the root of the Cessna 152, and the NACA 6516 which closely resembles the wing profile of some STOL aircraft such as the Zenith STOL CH750 SD. To determine the aerodynamic coefficients of either airfoil, the XFLR5, v6.61 software was used to conduct the analysis. By simulating each foil in various angles of attack, ranging from $0°$ to $25°$, it was possible to determine that the NACA 6516 airfoil has the highest lift coefficient and, therefore, the latter aircraft was chosen to model the half wing. In Table 4.4 are presented the aerodynamic properties of the foil for maximum lift is obtained ($\alpha = 18°$). The remaining results from the simulations are presented in Annex A.4

Table 4.4: NACA 6516 aerodynamic coefficients for $\alpha = 18°$.

$\alpha[°]$	C_L	C_D	C_m	X_{CP}
18	1.7898	0.07594	-0.087	0.263

The aspect ratio ($\mathcal{R}$) of a wing represents the relation between the mean chord and span. Using $\mathcal{R}= 6.7$ for the wing of the aircraft, the half wing model will have half of the span and, therefore, $\mathcal{R}= 3.4$. To ensure that the model's dimensions are adequate, it is necessary to ensure that $b < 1m$ since the wing will be mounted vertically in the wind tunnel, whose test section is limited to $1m$ tall. By limiting the half span to $0.8m$, it was possible to achieve a half wing with appropriate dimensions for the aeronautical wind tunnel.

Using the same equations as in the previous load case, it is possible to calculate the aerodynamic forces applied on the half wing model and the moments acting on the root of the wing which is also the attachment point to the balance at quarter chord distance from the leading edge. The results are presented in Table 4.7. It is noteworthy that, since the wing is placed upright in the tunnel, the generated lift is represented by F_y.

4.4.3 Formula Student Model Car

Formula Student is an international engineering competition where students are challenged to design, build and compete with a formula car. As the car's aerodynamic components are designed, there is a need to test them or validate the CFD models that are used. Since on-track testing is expensive, complex and time consuming, teams that have the ability to conduct experimental validations using wind tunnels, leap at the opportunity, as was the case for the Instituto Superior Técnico (IST) team, FST Lisboa, back in 2022 in as study conducted by Pacheco [34]. This particular test is of especially relevant since the model was tested at considerably high speeds, close to the upper limit of the tunnel.

Considering a model with a scale factor of $\lambda = 1/3$ to ensure that the model fits appropriately inside the tunnel, it is possible to estimate the aerodynamic loads of the model. As a courtesy, FST Lisboa provided some data regarding the latest prototype designed by the team, the FST 14. The data regarding the forces, shown in Table 4.5, is given in terms of force coefficients multiplied by the reference area of the $1/3$, with corrections according to the scale factor using the formula $C_F S' = C_F(\lambda^2 S)$, where C_F represents any of the force coefficient, S' represents the scaled down area and λ is squared since there is, in fact, the scaling of an area. Regarding the moments, the data was corrected by $C_M(Sb)' = C_M\lambda^3(Sb)$.

Table 4.5: Aerodynamic coefficients of the FST14 and the required corrections using the scale factor.

	$C_D S[m^2]$	$C_Y S[m^2]$	$C_L S[m^2]$	$C_{M_x} Sb[m^3]$	$C_{M_y} Sb[m^3]$	$C_{M_z} Sb[m^3]$
Straight Line	0.18	0.00	-0.56	0.000	0.014	0.000
Cornering	0.17	0.02	0.50	-0.002	-0.015	-0.013

The available data presents values regarding both straight line and typical cornering conditions. Using equations 4.1 and 4.2, it is possible to calculate the model's loads at the maximum speed of $40m/s$ on the wind tunnel test. The limit loads, considered the maximum of each component between the straight line and cornering conditions, as summarised in Table 4.7.

4.4.4 Suspension Bridge

The testing of bridges is one of studies performed by LNEC that make use of aeronautical wind tunnel. Typically on this type of studies, a sectional model of the bridge is tested at various speeds and incidence angles, to determine its aerodynamic properties and detect specific phenomena, such as galloping, divergence or flutter. This was the case with the 516 Arouca bridge, a suspended pedestrian bridge that was tested at LNEC [49].

A scaled model with $\lambda = 1/4$ was developed for testing, resulting in one of the largest tested using the aeronautical wind tunnel, corresponding roughly to 30% of blockage ratio, as estimated in the calculation of the flat plate load case in Section 4.4.1. Given that these types of tests are some of the most common ones in the laboratory, the bridge load case provide a sense of the nominal loads for the force balance, as well as the limiting scenarios at high speeds.

The aerodynamic coefficients of the bridge section are presented in Table 4.6.

Table 4.6: Aerodynamic coefficients of the 516 Arouca bridge (from [49]).

C_D	C_L	C_m
3.03	-0.32	0.05

To calculate the respective forces and moment, the report [49] defines the reference area using the value $d = 0.301m^2/m$, corresponding to the exposed area per unit length of the bridge deck. The exposed area represents the area of the exposed solid beams, placed on the deck beam, handrails and frame of the bridge. Since the model is exactly $1m$ long, the reference area can be assumed to be $S = 0.301m^2$. The reference length necessary to calculate the moment is provided as the distance from the centre of gravity to the suspension, $x = 0.628m$. Using once again the aerodynamic load equations, 4.1 and 4.2, the loads can be estimated to define the load case, as summarised in Table 4.7.

4.4.5 Communications Antenna

The design of a force balance is not only defined by its upper limiting scenarios. It is necessary to analyse some of the tests with minimal loads in order to define the requirements for the resolution of the force balance for either forces and moments. One of the tests conducted at LNEC's aeronautical wind tunnel fits this description: the testing of antennas, which vibrate due to the wind interaction, in order to develop methods of reducing the wind effects. With velocities as low as $4.4m/s$, this experimental test presents relatively small loads that can be used to define the requirements regarding the resolution of the force balance.

Although the actual data regarding the study cannot be discussed, the method for achieving the actual loads was similar to the previous load cases, i.e. using equations 4.1 to calculate the aerodynamic forces, and 4.3 to calculate the moments generated by those forces on the attachment point. The results of the calculations define the final load case to be considered, which are resumed in Table 4.7. From the results it is possible to define a minimal resolution of at least $0.2N$ for all forces and $0.04Nm$ for the moments.

4.5 Load Cases and Displacements

Having defined the different testing scenarios, it is necessary to define a limit for each of the loads in order to define the requirements. The summary of load cases and limits for each load are presented in Table 4.7.

Table 4.7: Load cases for each testing scenario and corresponding load limits.

Load case	F_x [N]	F_y [N]	F_z [N]	M_x [N·m]	M_y [N·m]	M_z [N·m]
Flat Plate in the AWT	-493	0	0	0	-97	0
Flat Plate in the BLWT	-457	0	0	0	-192	0
Half Wing	-14	333	0	-133	-6	4
Formula Student Car	-177	20	-550	-1	-15	-13
516 Arouca Bridge	-80	0	-8	0	1	0
Antenna	-0.20	0	0	0	-0.04	0
Limit Loads	-493	333	-550	-133	-192	-13

The balance must withstand all loads within the limits without damage in the form of fracture or plastic deformation. In addition, for a force balance to function properly, the model must experience minimal deflection, since this will affect the aerodynamic loads. For this reason, it is also necessary to define requirements regarding the maximum allowed angular and linear displacements at the attachment point of the support structure to the model at a height of of $100\,\mathrm{mm}$. This height was chosen since it is considered to be an average testing height for the majority of the models.

The most important requirement is to restrict the angular displacements, since these correspond to the aerodynamic angles - angle of attack (α), yaw angle or sideslip angle (β) and roll angle (ϕ) - which directly affect the aerodynamic loads. For this reason, the limit was set at $2°$ for all angular displacements ($\theta_x, \theta_y, \theta_z$). Although ideally the restriction would be much tighter, this limit represents a conservative limit, while ensuring that this requirement can be verified once the balance is built. Additionally, since the limit displacement is defined for the limiting loads, the actual displacement for nominal loads will be far more acceptable. In terms of linear displacements, the limit was set at $10\,\mathrm{mm}$ in every direction, which is not as restrictive since it has less impact on the loads acting on the model.

4.6 Mechanical Design Safety Factors

When designing any mechanical system, it is important to set safety factors which represent a ratio between the failure strength of a part and the stress it is expected to nominally sustain [51]. It is important to define a safety factor taking into account all possible uncertainties in the design and manufacturing process of the force balance. One of the methods that can be used to determine this factor is Pugsley's method [51].

The method determines a safety factor, N, that is dependent on two independent factors, N_1 and N_2, which respectively measure the uncertainty and the risk of failure. The first factor is dependent on three variables, labelled A, B and C, representing the quality of materials, workmanship, maintenance, and inspection, the control over applied loads and the accuracy of stress analysis, respectively. Each of the variables can take up one of four a grades: poor, fair, good, very good. The second factor depends solely on two variables, D and E, which represent respectively the danger to people and the economic impact. The grade of these variables only has 3 possible values - not serious, serious, very serious.After grading each variable the factors can be calculated using Tables A.5 and A.6. To determine the overall safety factor, the two independent factors are multiplied as $N = N_1 \cdot N_2$. By applying the method to the design and construction of this force balance, a final value of $N = 1.45$ was achieved, as demonstrated in table 4.8. For the design of the force balance, the safety factor will be applied on the load cases, meaning that all the mechanical requirements must be met when loads 1.45 times higher than the load cases are applied.

Table 4.8: Calculation of the safety factor using Pugsley's Method.

A	B	C	D	E	N_1	N_2	N
G	VG	G	NS	S	1.45	1.00	1.45

In addition to this safety factor, there are others that could be applied in the design of a force balance. In a previous force balance design by Oliveira [35], precautions were taken to ensure the safety of the sensing bars, which are the most critical part of the design. The sizing of the sensing bars took into consideration two important aspects - the plastic deformation and the buckling of the bars. The design required the that the maximum axial experienced by the bar did not surpass 60% of the yield force and 80% of the critical force for buckling. Although the former did not prove to be an issue, there was the occurrence of buckling in one of the sensing bars. Although it is possible that this did not occur during testing, a change in this parameter might prevent the repetition of this critical failure. Taking this into consideration, a new requirement can be defined, ensuring that the maximum axial force in any of the sensing bars does not exceed 60% of the yield force and 70% of the critical force for buckling.

Chapter 5

Mechanical Design

The design process will encompass the overall dimensioning of the force balance, the detailed design of each component as well as a numerical FEM analysis to ensure all requirements are met.

The initial design will take advantage of a previous design of a force balance developed by LNEC, based on the force balance design by Ferreira [52]. Since both platforms were already manufactured, an attempt was made to use these with minimal changes. However, the design of the sensing bars and attachment mechanism had to be designed taking into account the requirements already defined, since these were not yet constructed. The design and computational analysis was carried out using *SolidWorks*® by *Dassault Systèmes*.

5.1 Analytical Model and Singularity Analysis

To define the overall dimensions of the force balance, given by the five variables previously mentioned in section 4.1.2 (a, α, b, β, h), it is necessary to understand how the force balance measures each of the loads and how each of the variables affects the performance of the force ballance.

5.1.1 Analytical Model

Considering a generic force balance, as shown in Figure 5.1, it is possible to define the coordinates (x, y, z) of each of the vertices which correspond to the extremities of each bar.

$$
\begin{aligned}
P_1 &= \left(\frac{b(2-3\beta)}{2\sqrt{3}}, -\frac{\beta b}{2}, -h\right) & Q_1 &= \left(\frac{a}{2\sqrt{3}}, \frac{a(2\alpha-1)}{2}, 0\right)\\
P_2 &= \left(\frac{b(2-3\beta)}{2\sqrt{3}}, \frac{\beta b}{2}, -h\right) & Q_2 &= \left(\frac{a}{2\sqrt{3}}, \frac{a(1-2\alpha)}{2}, 0\right)\\
P_3 &= \left(\frac{b(3\beta-1)}{2\sqrt{3}}, \frac{b(1-\beta)}{2}, -h\right) & Q_3 &= \left(\frac{a(1-3\alpha)}{2\sqrt{3}}, \frac{a(1-\alpha)}{2}, 0\right)\\
P_4 &= \left(\frac{-b}{2\sqrt{3}}, \frac{b(1-2\beta)}{2}, -h\right) & Q_4 &= \left(\frac{a(3\alpha-2)}{2\sqrt{3}}, \frac{a\alpha}{2}, 0\right)\\
P_5 &= \left(\frac{-b}{2\sqrt{3}}, \frac{b(2\beta-1)}{2}, -h\right) & Q_5 &= \left(\frac{a(3\alpha-2)}{2\sqrt{3}}, \frac{-a\alpha}{2}, 0\right)\\
P_6 &= \left(\frac{b(3\beta-1)}{2\sqrt{3}}, \frac{b(\beta-1)}{2}, -h\right) & Q_6 &= \left(\frac{a(1-3\alpha)}{2\sqrt{3}}, \frac{a(\alpha-1)}{2}, 0\right)
\end{aligned}
\tag{5.1}
$$

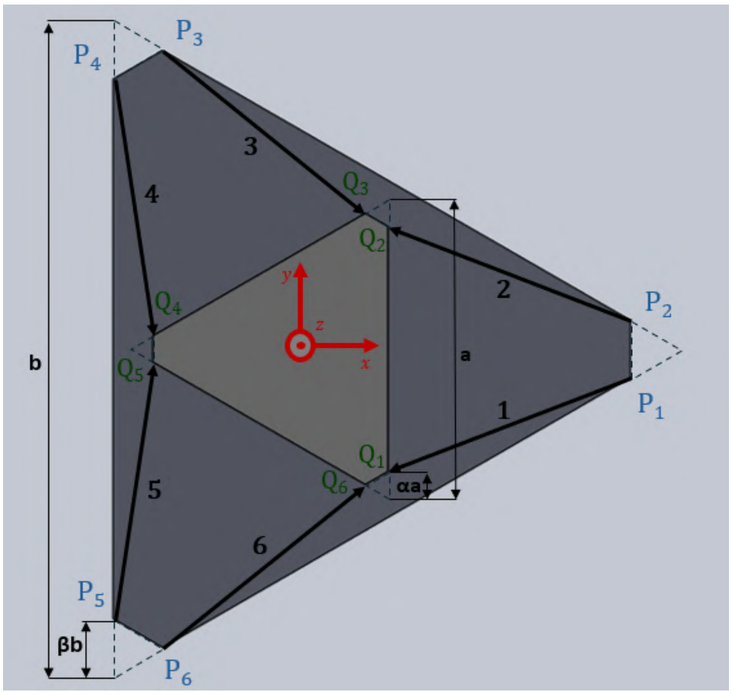

Figure 5.1: Diagram of a generic force balance.

The axial force in each bar can be decomposed into three distinct components acting on the top platform, at the Q_i vertices, where i represents the number of the bar from one to six. To decompose the forces, they can be multiplied by the unit vector V_i corresponding to a vector with the direction of the bar, pointing form the bottom to the top platform,

$$\vec{V_i} = \left(V_{i_x}, V_{i_y}, V_{i_z}\right) = \frac{Q_i - P_i}{l}\,, \tag{5.2a}$$

with

$$l = \sqrt{\frac{1}{3}(a^2(3\alpha^2 - 3\alpha + 1) + ab(3\alpha\beta - 1) + b^2(3\beta^2 - 3\beta + 1) + 3h^2)}\,. \tag{5.2b}$$

By substituting the coordinates for each point in Equation (5.2a), the unit vectors for each bar can be written with respect to the five design variables.

$$\vec{V_1} = \frac{1}{l}\left(\frac{a - b(2 - 3\beta)}{2\sqrt{3}}, \frac{a(2\alpha - 1) + \beta b}{2}, h\right) \tag{5.3a}$$

$$\vec{V_2} = \frac{1}{l}\left(\frac{a - b(2 - 3\beta)}{2\sqrt{3}}, \frac{a(1 - 2\alpha) - \beta b}{2}, h\right) \tag{5.3b}$$

$$\vec{V_3} = \frac{1}{l}\left(\frac{a(1 - 3\alpha) - b(3\beta - 1)}{2\sqrt{3}}, \frac{a(1 - \alpha) - b(1 - \beta)}{2}, h\right) \tag{5.3c}$$

$$\vec{V_4} = \frac{1}{l}\left(\frac{a(3\alpha - 2) + b}{2\sqrt{3}}, \frac{\alpha a - b(1 - 2\beta)}{2}, h\right) \tag{5.3d}$$

$$\vec{V_5} = \frac{1}{l}\left(\frac{a(3\alpha - 2) + b}{2\sqrt{3}}, \frac{-\alpha a - b(2\beta - 1)}{2}, h\right) \tag{5.3e}$$

$$\vec{V_6} = \frac{1}{l}\left(\frac{a(1 - 3\alpha) - b(3\beta - 1)}{2\sqrt{3}}, \frac{a(\alpha - 1) - b(\beta - 1)}{2}, h\right) \tag{5.3f}$$

Once all the bar's axial forces are decomposed and applied to the vertices of the top platform, the equation for all the loads can be derived. In the case of the forces, presented in equation 5.4, the forces applied on the top platform are given by the sum of the forces of all six bars. Therefore, the forces in the

x, y and z components are given respectively by

$$F_x = -\sum_{i=1}^{6} r_i \cdot V_{i_x} \, , \tag{5.4a}$$

$$F_y = -\sum_{i=1}^{6} r_i \cdot V_{i_y} \, , \tag{5.4b}$$

$$F_z = -\sum_{i=1}^{6} r_i \cdot V_{i_z} \, . \tag{5.4c}$$

Regarding the moments, a process similar to the force equations can be followed, including variable d_s, to represent the vertical distance above the centre of the top platform where the aerodynamic loads are applied. In an actual force balance, this distance represents the length of the support structure which attaches to the model. The ability to alter this parameter in the mathematical model will be useful when changing the balance configuration for a different geometry experiment.

$$M_x = \sum_{i=1}^{6} -r_i \cdot V_{i_z} \cdot Q_{i_y} + \sum_{i=1}^{6} -r_i \cdot V_{i_y} \cdot d_s \, , \tag{5.5a}$$

$$M_y = \sum_{i=1}^{6} r_i \cdot V_{i_z} \cdot Q_{i_x} + \sum_{i=1}^{6} r_i \cdot V_{i_x} \cdot d_s \, , \tag{5.5b}$$

$$M_z = \sum_{i=1}^{6} r_i \cdot V_{i_x} \cdot Q_{i_y} + \sum_{i=1}^{6} -r_i \cdot V_{i_y} \cdot Q_{i_x} \, . \tag{5.5c}$$

5.1.2 Singularity Analysis

It is necessary to define the values for the five variables that control the overall design of the platform (a, α, b, β, h). The relationship between these values is inherently linked to the performance and load carrying capabilities of the force balance.

The performance of a Stewart platform force balance can be defined as the ability to measure, with accuracy, loads in all six degrees of freedom. In a similar fashion, in the case of a Stewart platform manipulator, the performance is determined by the ability to translate or rotate the top platform across all six degrees of freedom. To determine the quality of a certain manipulator, and in particular for this force balance, a quality index, λ, is employed. The index, found in Equation (5.6), is given by the ratio between the determinant of the Jacobian matrix of the configuration and the determinant of the Jacobian matrix of an optimal configuration. Since the determinant is always maximum for an optimal configuration, corresponding to a type 3-3 octahedral manipulator, $0 \leq \lambda \leq 1$ [47], where 0 corresponds to a singularity, a states where the force balance cannot support a one or more of the load's components.

$$\lambda = \frac{|J|}{|J|_m} \tag{5.6}$$

The Jacobian matrix of a Stewart platform configuration is a 6×6 matrix where each column is the vector of the Plucker coordinates of the i^{th} bar, denoted by $\hat{S}_i$. This vector comprises two vectors, each one with 3 elements: the first three elements, denoted by d, are related with the distance between the two connections points of the bar that link to the platform; the last three, denoted by m, are related to the resultant moments at the origin due to a force applied axially on the bar. Assuming that all six $\hat{S}_i$ vectors point from the bottom platform to the top platform, as shown in Figure 5.1, the Jacobian matrix can be constructed according to

$$J = \begin{bmatrix} \hat{S}_1 & -\hat{S}_2 & \hat{S}_3 & -\hat{S}_4 & \hat{S}_5 & -\hat{S}_6 \end{bmatrix} , \tag{5.7a}$$

where

$$\hat{S}_i = \begin{bmatrix} d_x & d_y & d_z & m_x & m_y & m_z \end{bmatrix}^T . \tag{5.7b}$$

Using the general case of the i^{th} bar, connecting points P_i and Q_i and considering the notation of Figure 5.1, the $\hat{S}_i$ vector can be given by the second order determinants of the matrix

$$\begin{bmatrix} 1 & x_{P_i} & y_{P_i} & z_{P_i} \\ 1 & x_{Q_i} & y_{Q_i} & z_{Q_i} \end{bmatrix} . \tag{5.8}$$

This way, the coordinates for vectors d and m can be calculated according to

$$d_x = \begin{vmatrix} 1 & x_{P_i} \\ 1 & x_{Q_i} \end{vmatrix} , d_y = \begin{vmatrix} 1 & y_{P_i} \\ 1 & y_{Q_i} \end{vmatrix} , d_z = \begin{vmatrix} 1 & z_{P_i} \\ 1 & z_{Q_i} \end{vmatrix} . \tag{5.9a}$$

$$m_x = \begin{vmatrix} y_{P_i} & z_{P_i} \\ y_{Q_i} & z_{Q_i} \end{vmatrix} , m_y = \begin{vmatrix} x_{P_i} & z_{P_i} \\ x_{Q_i} & z_{Q_i} \end{vmatrix} , m_z = \begin{vmatrix} x_{P_i} & y_{P_i} \\ x_{Q_i} & y_{Q_i} \end{vmatrix} . \tag{5.9b}$$

Combining equations (5.7b) and (5.9), the $\hat{S}_i$ vector can be obtained as

$$\hat{S}_i = \begin{bmatrix} x_{Q_i} - x_{P_i} & y_{Q_i} - y_{P_i} & z_{Q_i} - z_{P_i} & y_{P_i} z_{Q_i} - y_{Q_i} z_{P_i} & x_{P_i} z_{Q_i} - x_{Q_i} z_{P_i} & x_{P_i} y_{Q_i} - x_{Q_i} y_{P_i} \end{bmatrix}^T \tag{5.10}$$

Using the notation defined in Figure 4.3, i.e. explicitly dependent on the five variables (a, α, b, β, h), the determinant of the Jacobian matrix of a conventional type 6-6 Stewart platform can be written in a single expression, as in Equation (5.11a). However, the quality index, λ, is given by the ratio between this value and the maximum value for the determinant of the Jacobian, which is found by changing the height between the platforms to the optimal value, given that the other variables remain constant. Differentiating Equation (5.11a) with respect to h it is possible to calculate the optimal value for the height, which can then be substituted in the original equation to give the maximum determinant of the Jacobian matrix, as shown in Equation (5.11b).

$$|J| = \frac{81\sqrt{3}a^3 b^{\frac{3}{2}} h^3 (3\alpha\beta - 2\alpha - 2\beta + 1)^3}{4\left(a^2(3\alpha^2 - 3\alpha + 1) + ab(3\alpha\beta - 1) + b^2(3\beta^2 - 3\beta + 1) + 3h^2\right)^3} \tag{5.11a}$$

$$|J|_m = \frac{27a^3b^3(3\alpha\beta - 2\alpha - 2\beta + 1)^3}{32\left(a^2(3\alpha^2 - 3\alpha + 1) + ab(3\alpha\beta - 1) + b^2(3\beta^2 - 3\beta + 1)\right)^{\frac{3}{2}}} \tag{5.11b}$$

Using the design from the partially constructed force balance based on the design of Ferreira [52], it was possible to evaluate the five dimensions of the overall design using the distances between the pickup points of each of the bars, as presented in Table 5.1. As seen, the quality index of this design is far from an optimal value of 1. For this reason, since the objective was to alter the already constructed platforms as minimally as possible, the only variable that could be changed was the height between the pickup points, h. By reducing the height to $205\,\mathrm{mm}$, it was possible to bring the quality index closer to the optimal value, reaching a value of 0.9970.

Table 5.1: LNEC's balance dimensions in millimetres and quality index.

	Original Design	Optimized Design
a	306	306
α	0.1025	0.1025
b	497	497
β	0.0741	0.0741
h	250	205
λ	0.9158	0.9970

5.2 Detailed Design

This section describes in detail each subsystem of the force balance, explaining what was taken into consideration to design each part, what materials were chosen and what design choices were made to ensure compliance with the requirements. The final design is shown in Figure 5.2 and the technical drawings of the full assembly are in Annex B. The remaining drawings are presented in the balance's user guide [53].

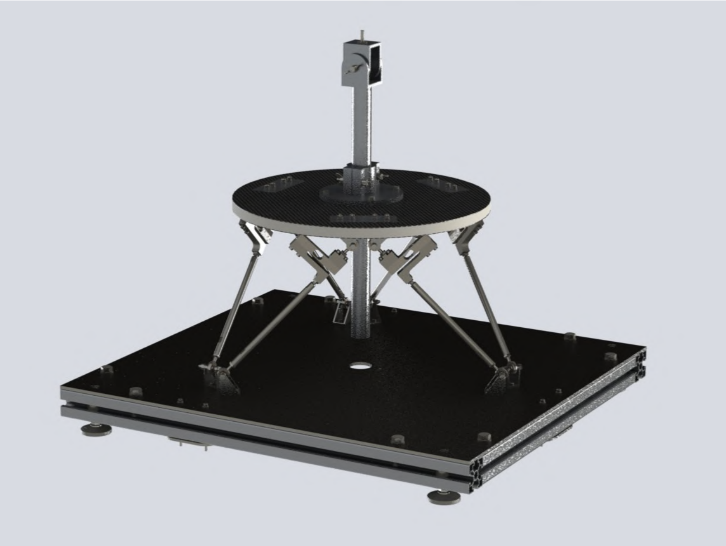

Figure 5.2: Force balance's final design.

5.2.1 Sensing Bars

The sensing bar subsystem is the most critical component of the overall assembly. It not only supports the top platform and the applied loads, but also measures the axial forces exerted in each bar, allowing to determine the applied aerodynamic loads. In addition to the load cell, a connecting rod is required to bridge the remaining length between the pickup points. To ensure that the sensing bars are subjected exclusively to axial forces, rod end bearings are used to connect the bars to both the top and bottom platforms. The final design of the sensing bar assembly is presented in Figure 5.3.

Several considerations were addressed to ensure that the design fulfilled the requirements. First, the load cell was positioned as close as possible to the top platform. Additionally, threaded connections were implemented using a combination of right-hand and left-hand threads, facilitating straightforward length adjustments of the sensing bars.

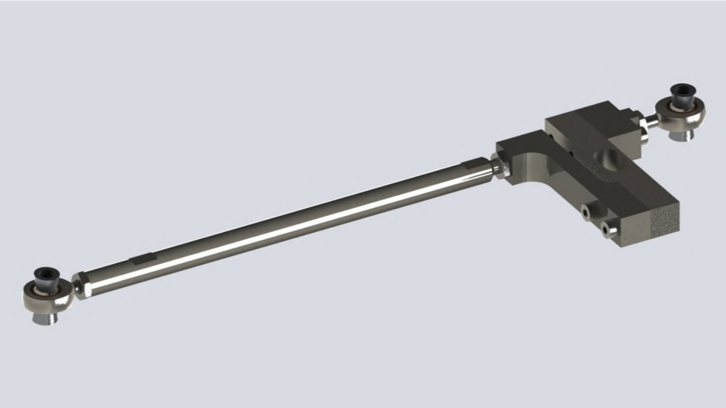

Figure 5.3: Sensing bar's design.

Load Cell Adaptor

The most critical component of the sensing bar subsystem is the load cell, which is responsible for measuring the axial forces acting on each bar. After selecting the adequate load cell (see details on Section 6.1), a custom adapter was designed to enable the beam load cell to connect to the bar and accurately measure axial forces. As it will also be explained in the aforementioned section, the balance was designed to be able to fit both the beam load cells and the S-type load cells. Therefore, an initial constraint was made to define the limiting dimensions of the adaptor.

The load cell adaptor consists of two main components: the rod end connector and the lever arm. The rod end connector is designed to attach the rod end bearing to one side of the load cell. The lever arm, on the other hand, enables the beam load cell to measure axial forces by inducing shear stresses at its central section. It attaches to the opposite end of the load cell and transmits force in a manner that activates the internal strain gauges. The connecting rod is attached to the other end of the lever arm, which is positioned directly beneath the rod end connector. This configuration ensures that the two applied forces are aligned along the same axis, thereby replicating an axial loading condition. This disposition, and respective loading condition, is shown in Figure 5.4b.


(a) Beam load cell. (b) Load cell with adaptor.

Figure 5.4: Loading scenarios for a beam load cell and one with the load cell adaptor.

For the material, it was important to consider not only the weight of the parts but also the strength of each part, since it is crucial to minimize deformations in every part except for the load cell. For both parts, a decision was made to choose steel, particularly AISI 304, a stainless steel to prevent corrosion of the parts without the need for a protective coating. For the rod end connector, the weight was a far more relevant factor since this part is placed above the load cell, where additional mass will influence the reading. Therefore, it would make sense to choose a lighter material, such as aluminium. However, a thread placed in an aluminium part usually require reinforcement with a steel insert. Due to limited space, this option was not viable. On the other hand, the lever arm is far more prone to deformations and the weight is not as relevant. For this reason, steel was considered for this part.

The lever arm design incorporates two fillets of relatively large radii to reduce stress concentrations. All the parts have a simplistic design in order to reduce the cost of manufacturing.

Connecting Rod

Material selection for the rod was driven by the need to meet strength and stiffness criteria, particularly in terms of yield and buckling resistance. Thus, maximizing the Young's modulus (E) and yield strength (σ_{yield}) was essential. Since the mass of the rod lies below the load cell, steel was selected due to its superior mechanical properties compared to common alternatives such as aluminium.

Another key design variable was the rod's diameter, which directly influences its resistance to yield and buckling. Based on the specified safety factors and the maximum axial force expected in a given bar, the minimum required diameter was determined analytically [54]. For yield, assuming a maximum axial force of $500\,\mathrm{N}$, slightly higher than any axial force calculated using the analytical model, the yield criterion assumed in Section 4.6, a minimum diameter of $2.06\,\mathrm{mm}$ is obtained through

$$d_{yield} = \sqrt{\frac{4F_{max}}{0.60\pi\sigma_{yield}}}\,, \tag{5.12a}$$

where

$$F_{max} = 0.60F_{yield}\,, \tag{5.12b}$$

with

$$F_{yield} = \sigma_{yield} \cdot A \,. \tag{5.12c}$$

To satisfy the buckling criterion, the full length of the bar corresponding to the distance between the pickup points, bar area moment and the Young modulus of the material were used to calculate the minimum buckling force, using Equation 5.13c. Using Equation 5.2b, as well as the buckling criteria considered in Section 4.6, the minimum diameter required to prevent buckling was found to be $4.88\,\mathrm{mm}$.

$$d_{buckling} = \left(\frac{64 F_{max} L^2}{0.70 \pi E} \right)^{1/4} \,, \tag{5.13a}$$

where

$$F_{max} = 0.70 F_{buckling} \,, \tag{5.13b}$$

with

$$F_{buckling} = \frac{\pi^2 E I}{K L}, \quad K = 1 \,. \tag{5.13c}$$

As a result, the final design incorporates a minimum diameter of $6\,\mathrm{mm}$, which is sufficient to satisfy both yield and buckling constraints.

Rod End Bearings

Originally, the LNEC force balance prototype was fitted with EARM-05 and EALM-05 rod end bearings, from igus® [55], at each end of the sensing bar. These components are made of igumid G and iglidur® W300, both of which are polymers characterised by their high resistance to wear and low friction coefficient. This makes these rod end bearings not only lightweight, but also reduces the need for maintenance and lubrication. A major drawback of using these components, when compared to the more conventional steel rod end bearings, is the lower capacity, both in a radial and in an axial direction. In the case of the EARM-05, the maximum tensile load is $550\,\mathrm{N}$ for short term loads and only $275\,\mathrm{N}$ in the case of long term loads. Given that some of the load cases lead to higher tensile loads, the rod end bearing be changed.

The chosen rod end bearings were the SAKB 5 F and SALKB 5 F [56], from SKF, with right hand and left hand threads, respectively, with a dynamic load rating of $3.25\,\mathrm{kN}$.

After the hole diameter was set to $5\,\mathrm{mm}$, the limit load of $500\,\mathrm{N}$ was checked to ensure the bolt would not suffer from shear failure. Finding the minimum diameter of a bolt or pin under shear loading, $d_{min} = \sqrt{\frac{4F_{max}}{n \pi \tau_{allowed}}}$ given that n represents the number of shear planes (2 in this case), it is necessary to define the maximum allowed shear stress $\tau_{allowed} = \frac{\tau_{yield}}{SF} = \frac{\sigma_{yield}}{\sqrt{3} SF}$. The yield shear stress is calculated using the von Mises criterion, which is divided by the safety factor of 1.45 to give the maximum allowed shear stress. Considering a bolt of grade 4.4, and using the values provided by Budynas and Nisbett [54] the minimum bolt diameter resulted in $1.83\,\mathrm{mm}$, significantly smaller than the diameter of an M5 bolt.

5.2.2 Bottom Platform

The bottom platform was adapted from the original force balance, as this subsystem had already been manufactured. The original design was made with rigidity and ease of manufacturing in mind, providing a solid platform for the balance to be constructed upon. However, given the new balance's design and some inherent flaws of the existing platform, certain modifications were necessary.

The platform consists of a $5\,\mathrm{mm}$ thick sheet steel base mounted on an extruded aluminium frame, made from 45×45 mm Bosch Rexroth profiles. To allow a precise levelling of the balance, the design incorporates four levelling feet, one in each corner of the platform, as seen in Figure 5.5a.

One modification made was the introduction of a circular hole, $40\,\mathrm{mm}$ in diameter, at the centre of the platform, to allow the support structure that attaches to the test model to pass through it. Another improvement performed on the bottom platform was the corrosion prevention of the steel base. Figure 5.5 shows the bottom plataform after the design modifications.

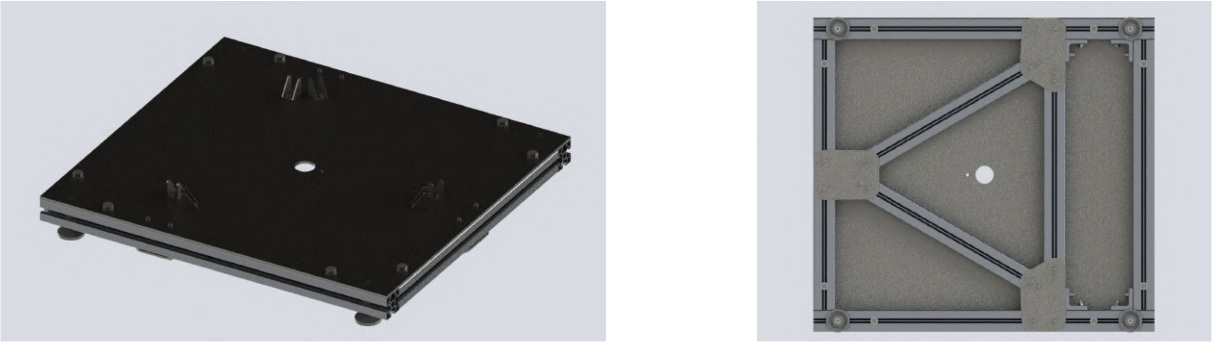
(a) Bottom platform's design.

(b) Aluminium frame.

Figure 5.5: Bottom platform assembly.

5.2.3 Top Platform

The top platform has a more complex design when compared to the bottom platform. In addition to connecting to the sensing bars, it must also integrate the support structure, requiring additional components to securely fix this subsystem. Moreover, minimizing the platform's mass is of the utmost importance, given that any additional mass will affect the load measurements. Given that the stiffness of the platform must also be taken into consideration, the actual manufactured composite sandwich panel, made of 2 sheets of carbon fibre and foam core, was kept for this project. A detailed view of the top platform in its final version is shown in Figure 5.6a.

The composite panel consists of a RohaCell® foam core, with a thickness of $15\,\mathrm{mm}$, sandwiched by two carbon fibre reinforced polymer (CFRP) sheets, each with multiple layers bidirectional fibres in various orientations. While the first component provides structural integrity and increases the platform's moments of inertia, the latter provides the high stiffness and strength. Since bolted connections can apply large forces on the composite, large backing plates where used to distribute the loads and avoid the collapse of the foam core.

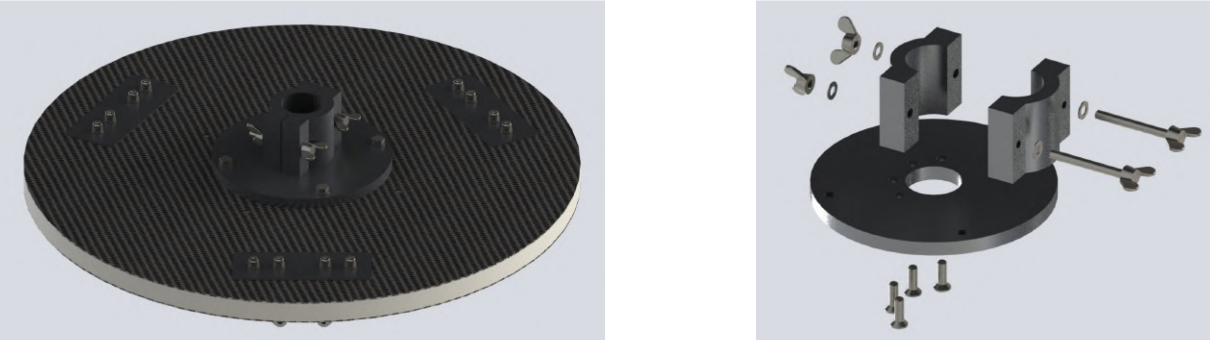

(a) Top platform. (b) Flange.

Figure 5.6: Top platform assembly.

The position of the pickup points was kept unchanged to incorporate the pre-existing components. The only changes to the platform were new holes to secure the flange that holds the support structure. The hole layout is seen in Figure 5.6a and detailed in Appendix B.

Flange

The flange must secure the support structure in all testing scenarios without allowing for excessive deflections or movement of the support structure. While its connection to the top platform is relatively straightforward, the connection to the support structure must be rigid and adjustable to position the support structure. Additionally, the flange's mass needs to be as minimal as possible. The final design of the flange is comprised of three separate parts: the base, the top and the clamp, as shown in Figure 5.6b.

The three-part configuration required less material and reduced machining time. The design relies on a clamping mechanism that engages with a large area along the tube's length to avoid deformations or damage.

The three parts were manufactured from aluminium, as the mass was a critical constraint. The base and top are joined using four M5 countersunk bolts. To reinforce the aluminium threads, steel threaded inserts were used in the top component. Once mounted to the platform, the clamping force is applied via the flange's clamp, which is secured with two wing bolts and nuts, enabling tool-free tightening. A rotating adjustment fit H9d9 was used to ensure a secure interface between the flange and support structure [57].

5.2.4 Support Structure

The support structure, as the top platform, has also a strict constraint on the mass of the components. Nevertheless, the support structure must minimise deflections, since these will directly impact on the attitude of the model, while also providing adjustment of the height, angle of attack and yaw angle of the model. The latter can be adjusted in height, through the coupling with the flange. The final design can be seen in Figure 5.7.

The adjustment of the angle of attack requires more consideration since an additional mechanism is needed to provide this feature. The adjustment mechanism, seen in Figure 5.7b, has two coupling parts which allow for rotation on the yy axis, thus altering the angle of attack. To fix the rotation, a bolt clamps both parts together, while a cylindrical spacer in between guarantees that the clamping forces do not deform the parts.

The other important component is the support structure's tube, which connects to the flange. As previously explained, this part was created with a rotating tolerance fit. Therefore, it was necessary to apply the corresponding tolerance (d9) to the tube's outer surface. Regarding the interface between the tube and the attachment mechanism, an interference fit H7p6 was chosen. Once the parts are connected, they lock into place due to this interference and, additionally, a set screw is added though the tube and the lower attachment. This avoids welds which can unintentionally warp the parts.

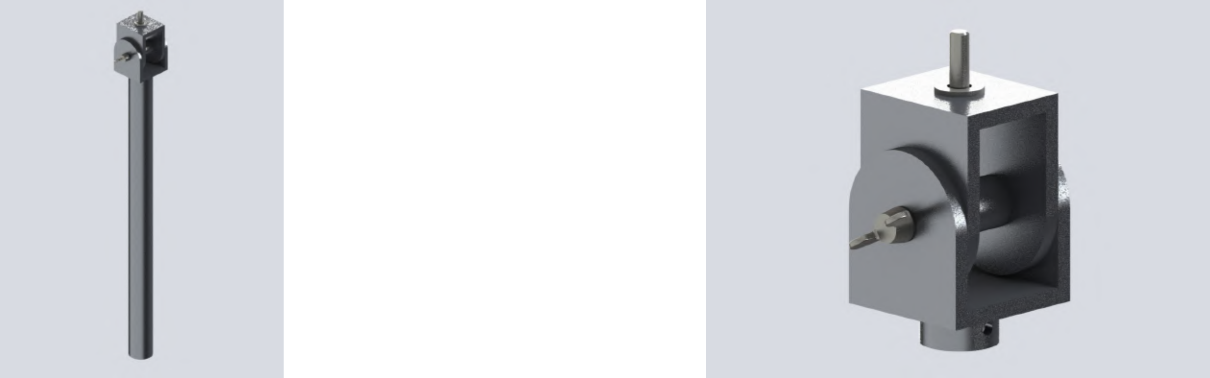

(a) Support structure assembly.

(b) Attachment with angle ajustment mechanism.

Figure 5.7: Support structure design.

5.3 Finite Elements Modelling and Analysis

An important step to ensure that the mechanical design of the force balance is in accordance with the stipulated requirements is to use computational analysis. Multiple FEM analysis were conducted to validate the linear and angular displacements on all the testing scenarios. All of these simulations, which were run on *SolidWorks*® were used to iterate and validate the design.

5.3.1 Initial Considerations

As the simulation requires a large amount of time and computation effort, less relevant aspects to the simulation were approximated or neglected. All simulations consisted of static analysis with a direct sparse solver in which the acceleration of gravity was neglected, since only the aerodynamic loads were relevant to define the deformations.

In order to comply with the requirement regarding the safety factor of the mechanical design all of the simulations were performed with a load 1.45 times higher than the defined load case.

Another important issue on the FEM is the definition of the parts' materials. The top and bottom platform in particular are available components that were already manufactured for a the previous prototype, for which there is no documentation proving the exact materials used. Therefore, a choice was made to use the same materials as the ones used by Ferreira [52], since the prototype also followed this design.

As the bottom platform can be considered rigid, it was excluded from the simulation. To fix the model, a fixture was created at the bottom surface of each bracket, simulating the connection to the bottom platform. Another simplification was the removal of all fasteners, including backing plates. Instead, bonded contacts were used to connect all parts, speeding up the simulation process. The only exceptions were the flange's bolted connections. To retain the nature of these crucial connections, the bolts were simulated using the bolted connection in the software and the surfaces were inhibited from penetrating into each other.

As crucial components to the behaviour of the force balance, the rod end bearings must be simulated in a manner that replicates their actual motion. To ensure a smooth motion of the bearing, the contact between the eye of the bearing and the outer casing was defined as a non penetration contact with no friction. Provided that the mesh at the contact is refined enough, the rod end bearings will only transmit axial loads to the bars.

It is also important to note that some parts are over-dimensioned, due to some design constraints. Despite this, FEM analysis were still performed on certain individual components, such as the flange and the load cell adaptor. These simulations were primarily used to refine and iterate the design. However, they will not be analysed in this chapter, as the focus here is placed exclusively on the simulations of the complete force balance assembly. The results of some of these simulations can be found in appendix C.

5.3.2 Mesh Definition and Convergenge Study

An important step to insure the accuracy of any analysis that uses finite elements is to determine the type and size of the elements to use. In *SolidWorks*®, a solid mesh can be created using two types of tetrahedral elements: linear or parabolic [58]. While the linear tetrahedral elements are defined by four corner nodes, connected by six straight lines, the parabolic elements require six additional nodes, which define a parabola between each of the corner nodes.

As each parabolic element requires more nodes, creating a parabolic mesh tends to take more time and computational effort. However, when considering two similar meshes which only differ in the type of element, the parabolic mesh tends to provide more accurate results. Therefore, the latter type of element was chosen for all simulations.

One of the best ways to determine the mesh size is to create a mesh convergence study. In this study, multiple meshes where created while varying some parameters which affect the element count. By extracting the results, it is possible to see what is the influence of the number and size of the elements in the accuracy of the results. The data from this study is presented in Figure 5.8.

In total, ten different meshes were generated, with the number of elements ranging from 4.7×10^4 to 2.1×10^5. To control the number of elements in each mesh, the maximum and minimum element

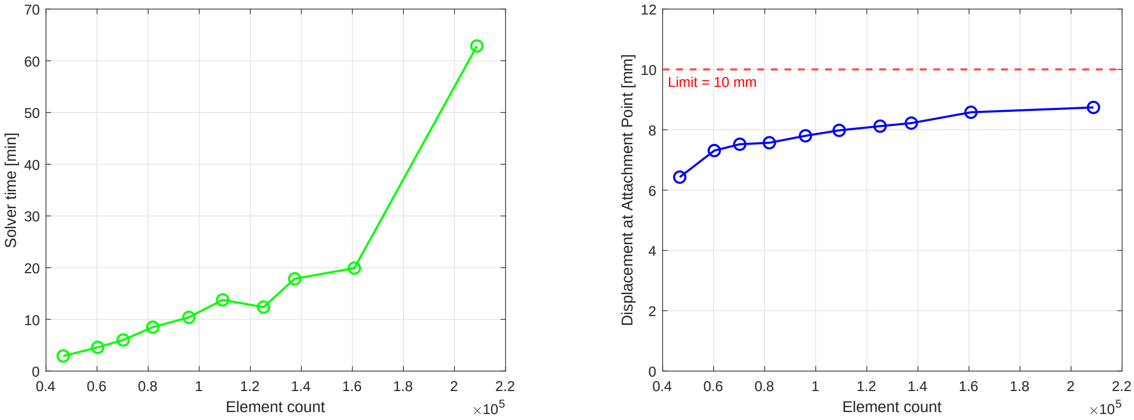

(a) Solver Time (b) Linear displacements at the attachment point

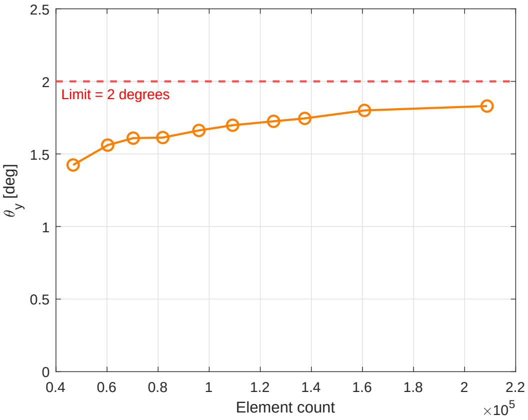

(c) Angular displacements at the attachment point

Figure 5.8: Results of the mesh convergence study

sizes were used, checking the quality of the mesh before proceeding with the remaining study. It is also important to note that some parts of the model are more critical than others when it comes to refining the mesh. One example is the rod end bearings, which ensure the accurate behaviour of the force balance, requiring a more refined mesh than other parts such as the top platform. To refine the mesh in such areas, the curvature-based mesh option was used, which increases the amount of elements in areas of high curvature, such as those in the rod end bearings.

To evaluate the convergence of the results, the linear and angular displacements at the attachment point was used, as shown in Figure 5.8. Not only are these values important to ensure compliance with the requirements, but they also represent a fairly smooth and global quantity which is less sensitive to the local mesh refinement, reducing the chance of singularities at a specific element affecting the overall result.

As it can be inferred from figure 5.8a, a larger number of elements would be far too costly in terms of computational effort. However, it can be noted that the results of both displacements mostly converge below the limit defined by the requirements. To balance the accuracy of the results to the computational cost, a compromise was made to proceed with a mesh with 1.25×10^5 elements.

5.3.3 Results and Analysis

On this study, only the first three load cases were considered, since they represent the limiting scenarios of the force balance. However, the suspension bridge load case was also simulated since it gives a more accurate representation of the conventional tests that are performed at LNEC. The results of the linear and angular displacements are presented in Table 5.2

Table 5.2: Linear and angular displacements results from FEM simulations.

Load Case	Linear Displacement [mm]	θ_x [°]	θ_y [°]	θ_z [°]
Flat Plate	8.12	0.01	1.73	0.01
Half Wing	5.04	0.97	0.01	0.02
Formula Student Car	1.31	0.01	0.26	0.05
516 Arouca Bridge	0.40	0.02	0.06	0.00

The results prove that the most excessive displacements will be found in the flat plate load case, whose displacement plot is shown in Figure 5.9, which was already expected. None of the remaining load cases exceed the limits defined in the requirements.

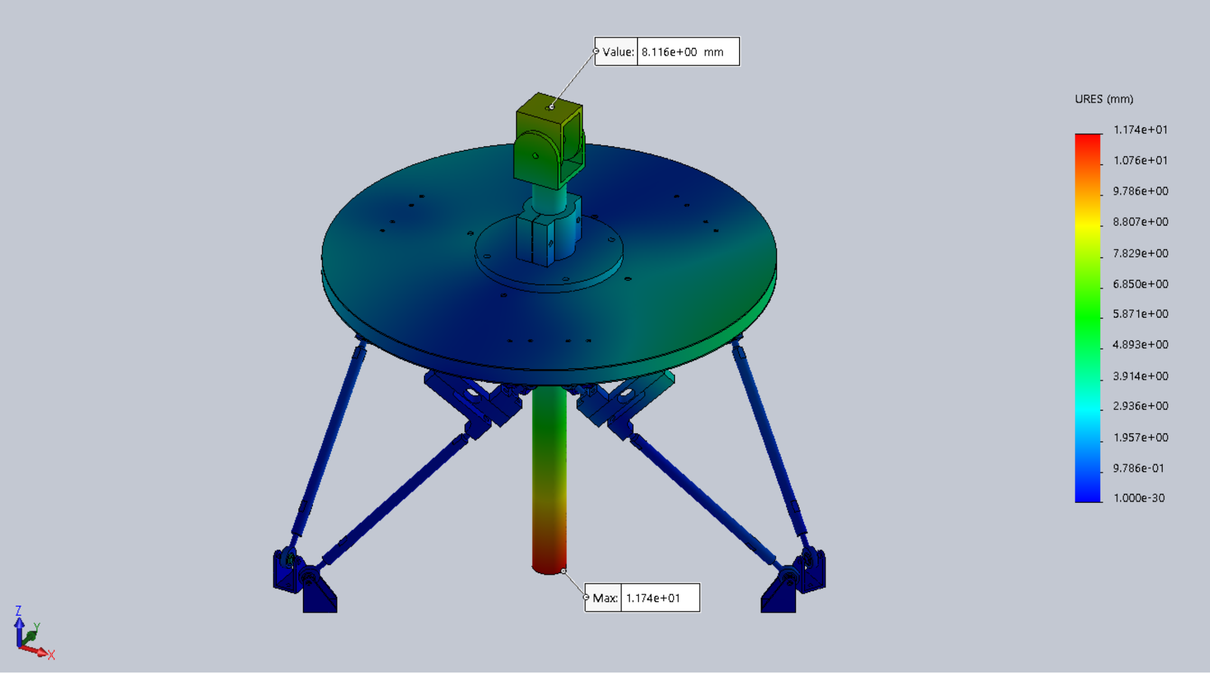

Figure 5.9: Displacement plot for the plate load case.

Chapter 6

Sensors and Instrumentation

This chapter focusses on the sensors used to measure the axial forces acting on each bar as well as the data acquisition system responsible for obtaining the data from the sensors, conditioning the signal and communicate with the computer's user interface.

6.1 Sensor Selection

6.1.1 Type of Sensors

One of the defined requirements, E.C.1, found in Appendix A.1, states that the load sensors must be commercially available. Three types of load cells were considered for the final design: S-type load cells, canister load cells and beam load cells.

S-type Load Cells

S-type load cells present an S shaped body which deforms under compressive and tensile loads applied on the upper and lower sections. Placed within the central portion of the cell are strain gauges which are used to accurately measure the strain and, as a consequence, the axial load. Although these type of cells are more commonly used to measure tensile loads, they can present enough accuracy under compressive loads.

Compared to other types of load cells considered, these offer certain advantages, including ease of integration with the sensing bars and relatively low cost. However, as one of the most rudimentary types of tension/compression load cells, their precision may be limited. Additionally, identifying load cells with the desired capacities proved challenging, as most commercially available options are designed for industrial applications and typically exceed the desired capacity by a factor of 10 to 100.

Canister Load Cells

Canister-type load cells typically have a cylindrical shape and measure axial forces via strain gauges fixed to the canister walls. In contrast to S-type load cells, these do not convert axial loads into shear loads, instead measuring the strain provided by the axial stresses on the cell body.

Although canister cells are generally more compact and provide greater precision for both tensile and compressive measurements, their availability was limited, and their cost prohibitively high. Consequently, this type of load cell was excluded from further consideration.

Beam Load Cells

Beam load cells have a beam-like geometry, fixed at one end with the load applied at the opposite end. The applied force is measured using strain gauges, which detect strain resulting from bending stresses along the beam's walls (tensile on one side and compressive on the other side, completing a full Wheatstone bridge), as shown in Figure 6.1a. Despite their simplicity, beam load cells are inherently incapable of directly measuring axial forces. As such, a custom adaptor must be designed to enable axial force measurement, as illustrated in Figure 6.1b.

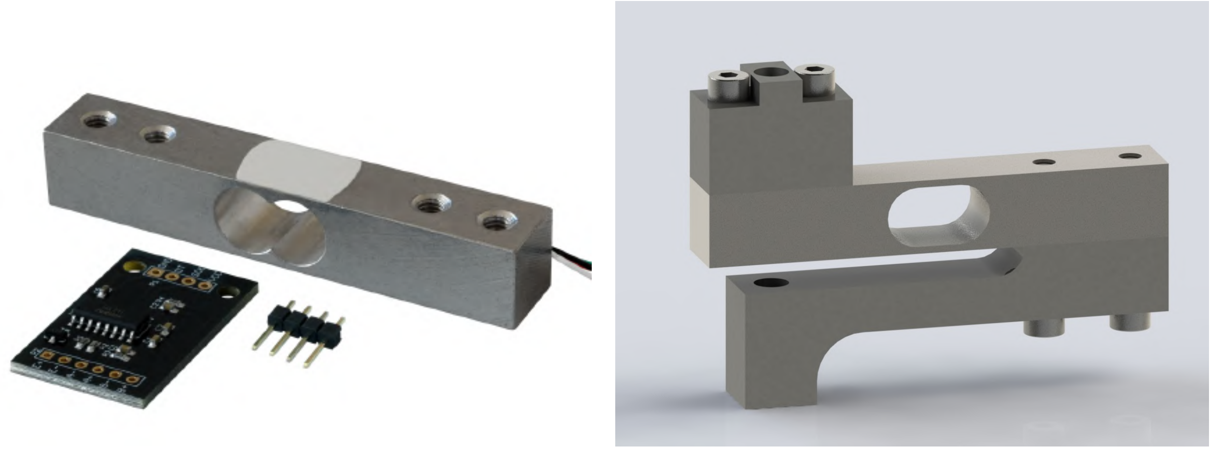

(a) *HX711-05* Load Cell by Simac Electronics GmbH [59].

(b) Load cell with adaptor to measure axial forces.

Figure 6.1: Beam load cell.

Typically, beam load cells are larger, heavier and often less accurate. However, beam load cells are considerably more affordable, enabling the use of multiple ranges rather than being limited to a single capacity. This flexibility enhances adaptability across a variety of experimental setups. Furthermore, beam load cells are more widely available and come in a broader range of load capacities. While their inherent accuracy is lower, this can be mitigated through metrological calibration, allowing for precise characterization across the full operational range.

For these reasons, the beam load cell was selected for the final design. Nevertheless, the design was kept compatible with the originally considered S-type load cells to preserve adaptability.

6.1.2 Measurement Ranges

To determine the full measuring range of the force balance, it was necessary to define the limiting scenarios in which the force balance should work. Using the load cases previously explained in Section

4.4 and the analytical in Section 5.1.1 it was possible to determine the axial forces acting in each bar for each of the testing scenarios.

Figure 6.2 presents the full range of axial forces for each load case. The lower end of the range, shown in green, corresponds to the loads at the minimum expected speed for each load case, while the upper end, shown in blue, represents the maximum loads for each load case. Intermediate load levels are depicted in grey. This visual representation allows for an evaluation of the complete load spectrum across all possible velocities, thereby allowing an informed selection of sensors, which are displayed in the lower half of the chart. For each sensor, the full measurement range is indicated. To account for the potential non-linearity typically observed near the limits of the operating range of a load cell, the top and bottom 10% of each sensor's range are highlighted in red and yellow, respectively.

Although each load cell may experience both compressive and tensile forces, the analysis assumes symmetrical behaviour in both directions. As such, the absolute value of the axial forces is used for sizing purposes. Furthermore, as some load cases approaching near-zero values, Figure 6.2 employs a logarithmic scale on the axial force axis to facilitate a more detailed assessment of the sensor response under very low load conditions.

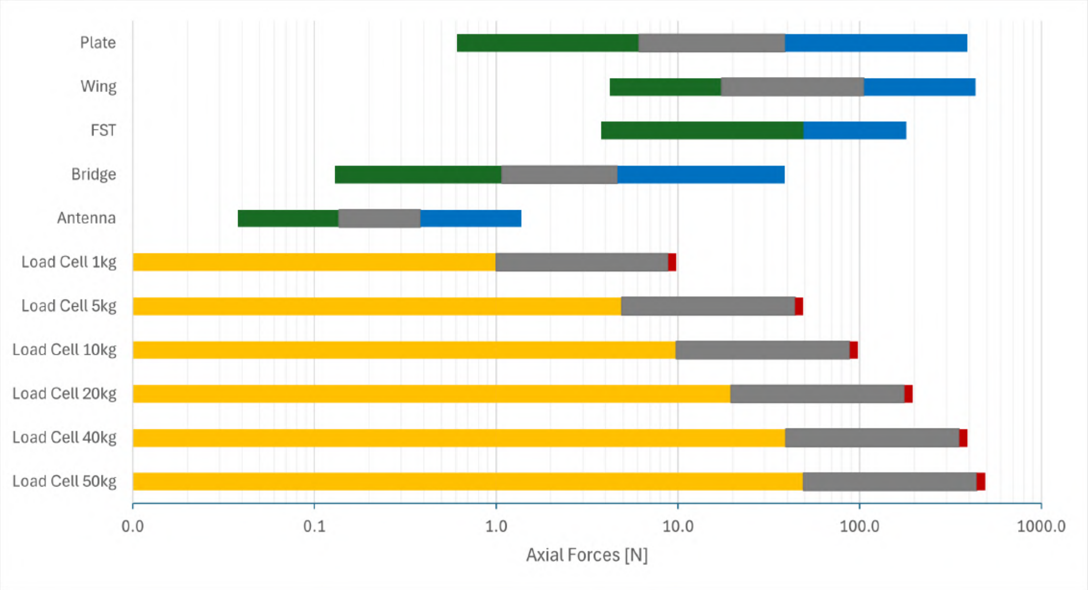

Figure 6.2: Ranges of the axial forces for each load case and each load cell.

A preliminary analysis clearly shows that the wide variety of load cases, combined with varying testing speeds, results in a broad range of axial forces acting on the sensing bars. This diversity significantly affects load cell selection. Selecting a load cell with a high capacity ensures it can withstand the maximum loads, but it comes at the cost of reduced resolution at lower force levels. Conversely, choosing a low-capacity load cell improves sensitivity for small forces but risks overloading under high loads.

Given these constraints, two approaches were considered: using a single high-capacity load cell with fewer linearity issues across the range, or employing multiple load cells, each optimized for a specific region of the force spectrum, allowing different configurations depending on the test conditions. The former was ultimately rejected due to its high cost and lack of certainty. The latter was selected as a more viable and flexible solution.

Beyond simply covering the full range of axial loads, it was necessary to ensure continuity between the selected load cells. Ultimately, a $5kg$ and a $50kg$ load cell were chosen, which offers a suitable compromise: sufficient resolution for low loads and an acceptable transition between sensors. Notably, the upper limit of the $5kg$ load cell corresponds approximately to the lower 10% threshold of the $50kg$ cell. Although this introduces a slight discontinuity, it was deemed acceptable, with plans to mitigate its effects through metrological calibration of the load cell assembly. For the moment, only the $5kg$ load cells were acquired.

The acquired load cells were the *HX711-05* by Simac Electronics GmbH. These relatively inexpensive load cells are available in a wide variety of capacities, allowing for larger versatility in future experimental tests. The compact design of the cells, although not as small as many others, fitted inside the design space with enough clearance and the attachment is achieved by 4 M4 screws, providing an almost unrestricted platform for the adaptor to be designed.

6.2 Data Acquisition

There are multiple options when considering which DAQ to use. As mentioned in Section 3.3, a choice can be made to prioritise cost, accuracy, noise reduction, among others. One of these examples are the *NI-9237* modules, from National Instruments™, shown in Figure 3.7. This module is specifically designed for the data acquisition of full or half Wheatstone bridges, allowing an extremely simple setup and facilitates the processing on the side of the user interface.

These modules are available in two distinct configurations, with either RJ50 or DSUB input gates. Although they essentially function in the same manner, allowing up to 4 bridges to be connected simultaneously, the DSUB uses only a single input gate requiring all bridges to be instrumented to a single connector. On the other hand, the RJ50 module allows for more adaptability, having four separate RJ50 gates, one for each bridge. Using the latter, the connection of a full Wheatstone bridge can be achieved according to Figure 6.3.

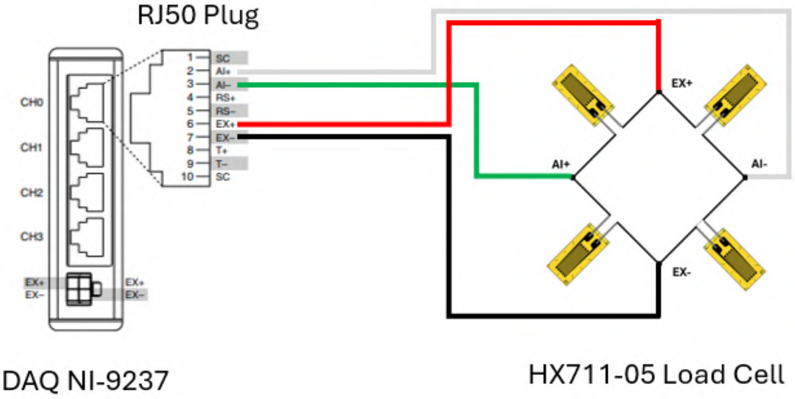

Figure 6.3: Wiring diagram for the *NI-9237* modules.

LNEC has already available three *NI-9237* modules with RJ50 gates, enough to connect the six required load cells, as well as a *cDAQ-9178* chassis, allowing up to eight modules to be connected at once.

6.3 Wiring

Although the wiring that was previously presented in Figure 6.3 can be used as is to connect each of the load cells to the DAQ, there were issues that needed to be solved which add some complexity to the final wiring scheme. As such, the full wiring diagram for a single load cell is shown in figure 6.4. The three main issues were the noise reduction of the signal, the connection to the RJ50 plug and the ability to remove the load cells from the force balance to be replaced.

Starting with the latter, since the load cells can be replaced to alter the range of the force balance depending on the test, or might need to be replaced due to damage, it was necessary to ensure that the instrumentation of a single load cell was as simple as possible and independent from the remaining wiring. Thus, the connector had to be introduced into the wiring, allowing the load cell to be disconnected. DB15 connectors were chosen, providing up to fifteen connections when only four are strictly required, for their robustness, electromagnetic shielding and compatibility to other load cells, which LNEC already has that were already instrumented. These were to be used with a different DAQ, the *Spider8* from *HBM*, which utilises DB15 connectors as the input gates for each Wheatstone bridge. The wiring configuration, respecting the correct pins for the *Spider8* according to *HBM*, is shown in Figure 6.4.

The final issue to be solved was the connection to the RJ50 plug which had to be durable and robust. This plug is designed to receive a ten component cable, where each component is a solid wire with a cross sectional area of $0.13\,\mathrm{mm}^2$ to $0.20\,\mathrm{mm}^2$ (26-24 AWG). For this reason, and in order to avoid unnecessary soldered connections, a single cable with ten components and shield was chosen.

As shown in the wiring diagram, the load cell comes with four separate wires. As these have a length of approximately $0.20\,\mathrm{m}$, it was necessary to extend these wires to a length of roughly $0.60\,\mathrm{m}$. To do so, a four wire shielded cable from Lapp GMBH (UNITRONIC LiYCY 4x0,50) was used. The other end of this cable is attached to the DB15 male connector according to the pin configuration provided by HBM for the *Spider8* DAQ. The female connector is attached to the lid of a junction box which is fixed to the bottom platform. This effectively creates a connector box, to which all the load cells will be able to connect to. In addition it also contains all the remaining wiring. On the other half of the wiring scheme, attached to the DB15 female connector is the ten component cable with shielding (UNITRONIC LiYCY 10x0,14), which spans a distance of approximately $3\,\mathrm{m}$, enough to go from the balance's position, underneath the tunnel, to the tunnel operator's table.

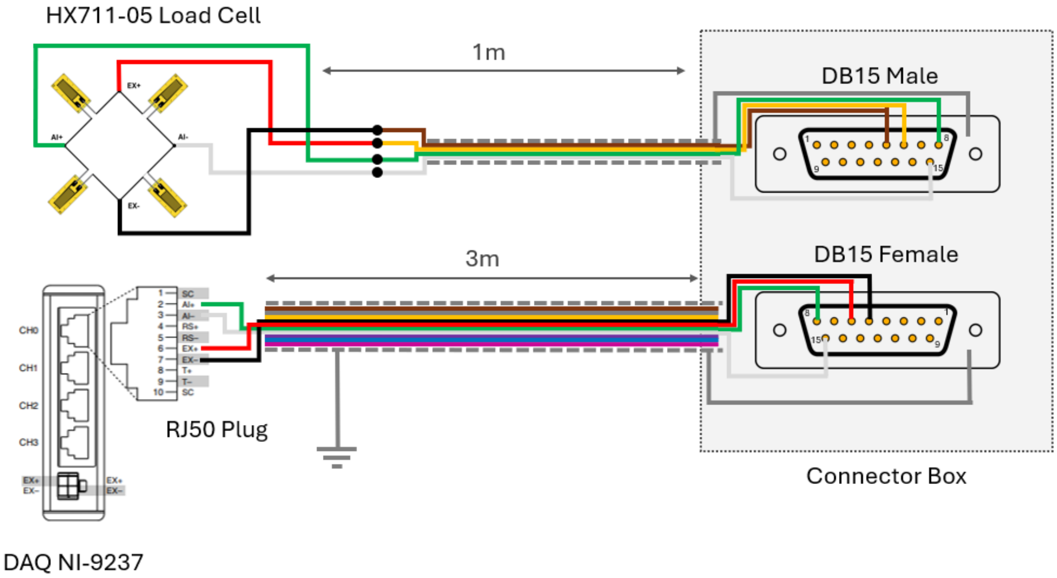

Figure 6.4: Complete wiring diagram for a single load cell.

6.4 User Interface

The user interface is an integral part of the force balance since it allows the user to input parameters or retrieve information from the force balance. Therefore, a well designed user interface can facilitate the acquisition and post-processing of data in any experimental test. For this equipment, the interface was designed in LabVIEW™, from National Instruments, which provides an almost seamless connection between the data from a NI DAQ and the final user interface.

The code behind the user interface centres around a loop which is in charge of the data acquisition using the typical LabVIEW™ VIs. The results from this acquisition are written in a TDMS file for later post processing and shown on the user interface, through charts and indicators for each of the loads in the central portion of the front panel, shown in Figure 6.5. The interface provides the user with various options regarding both the visualisation and the acquisition. Regarding the acquisition, the interface allows to change the acquisition rate, the output file and whether to remove any offset before starting the acquisition. Most importantly, the interface allows the user to choose which data to register as well as what data is shown in the interface itself in real time. It provides three different data sets: the axial forces, the loads calculated through the analytical model, and the loads calculated using the calibrated model. By allowing all of these different options, the acquisition can be tailored to each specific test.

It is important to note that, apart from the main user interface, two additional interfaces and respective VI's were created to facilitate the calibration processes of both the balance and each load cell. The major difference in these interfaces is that the acquisition occurs inside a time based loop, whose length and delay, respectively named acquisition and settling times, can be adjusted along with the number of load steps. This facilitates the procedure it self and the subsequent post processing of the data.

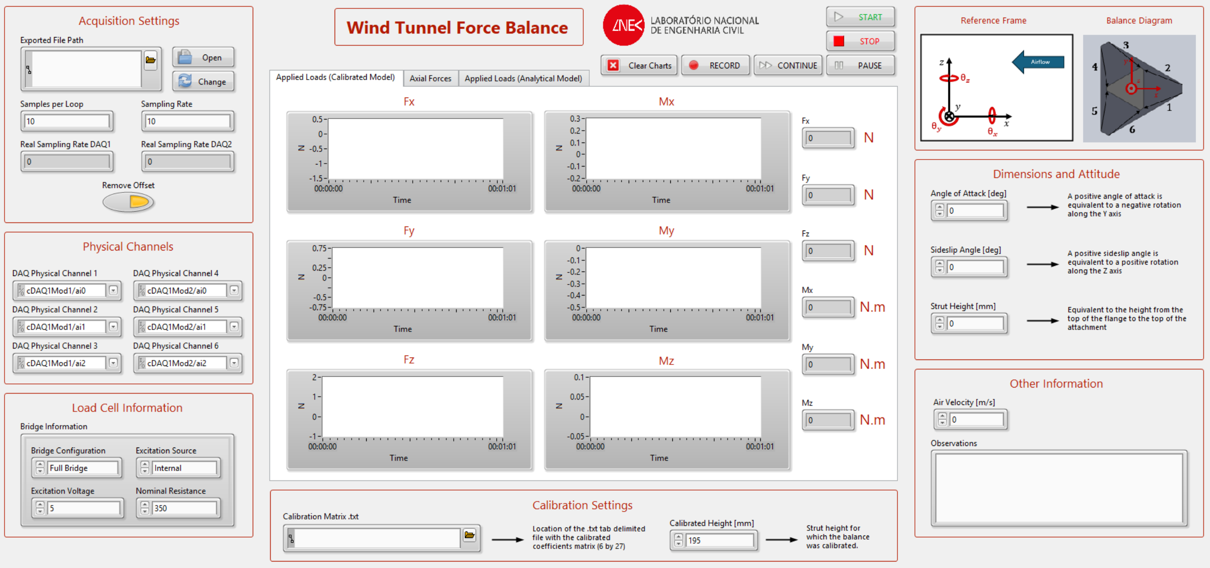

Exported File Path:

Samples per Loop: 10

Sampling Rate: 10

Real Sampling Rate DAQ1: 0

Real Sampling Rate DAQ2: 0

DAQ Physical Channel 1: cDAQ1Mod1/ai0

DAQ Physical Channel 2: cDAQ1Mod1/ai1

DAQ Physical Channel 3: cDAQ1Mod1/ai2

DAQ Physical Channel 4: cDAQ1Mod2/ai0

DAQ Physical Channel 5: cDAQ1Mod2/ai1

DAQ Physical Channel 6: cDAQ1Mod2/ai2

Bridge Information

Bridge Configuration: Full Bridge

Excitation Source: Internal

Excitation Voltage: 5

Nominal Resistance: 350

Fx: 0 N

Fy: 0 N

Fz: 0 N

Mx: 0 N.m

My: 0 N.m

Mz: 0 N.m

Angle of Attack [deg]: 0 → A positive angle of attack is equivalent to a negative rotation along the Y axis

Sideslip Angle [deg]: 0 → A positive sideslip angle is equivalent to a positive rotation along the Z axis

Strut Height [mm]: 0 → Equivalent to the height from the top of the flange to the top of the attachment

Air Velocity [m/s]: 0

Observations:

Calibration Matrix .txt → Location of the .txt tab delimited file with the calibrated coefficients matrix (6 by 27)

Calibrated Height [mm]: 195 → Strut height for which the balance was calibrated.

Figure 6.5: Front panel of the user interface.

Chapter 7

Manufacturing, Assembly and Cost

This chapter focuses on the construction of the force balance, including the manufacture of the required parts and their assembly into the final instrument. In addition, a bill of material is presented which list all of the parts, as well as their acquisition or manufacturing costs.

Some parts that were already manufactured, were reused, were only subject to small modifications, while the new parts were either purchased or machined by custom order.

7.1 Costed Bill of Materials

The Bill of Materials (BOM) is the complete list of the components of a system, presented in Table 7.1. It groups the parts into their respective assemblies and sub assemblies. In addition, this BOM presents the materials, manufacturing processes and costs of the parts, effectively creating a Costed Bill of Materials (CBOM).

Since some of the parts were already purchased or manufactured for the previous prototype, their cost was not considered in the CBOM. It is also worth to mention that fasteners and some small parts, such as the 3D printed ones, were not included in this final CBOM. Finally, only the force balance system was considered, meaning that the costs associated with calibration jigs, explained in chapter 8, were also not included.

7.2 In-house Modifications

The only two parts which required modifications were the platforms, which needed to conform to the new design. Regarding the bottom platform, a $40\,\mathrm{mm}$ circular hole was drilled at the centre of the plate. After finishing the drilling operation, the plate was removed from the platform assembly to remove the rust and paint with the corrosion-resistant spray paint.

The top platform required more careful planning, since various additional holes had to be drilled into specific positions on the platform and there was a lack of references on the platform itself. To facilitate the drilling procedure, a 3D printed jig was designed to allow the precise drilling of the eight holes of

Table 7.1: Bill of Materials with acquisition cost.

Assembly	Subassembly	Name	Quantity	Material	Make/Buy	Manufacturing Process	Cost (€)
Top Platform	Platform	Top Platform	1	-	Existent	Vacuum Resin Infusion	-
		Bracket Backing Plate	6	Al 2024-T3	Existent	Waterjet/Lasercut	-
		Top Bracket	6	Al 2024-T3	Existent	Machining	-
	Flange	Flange Top	1	Al 7075-T6	Make	Machining	435.00+IVA
		Flange Base	1	Al 7075-T6	Make	Machining	
		Flange Clamp	1	Al 7075-T6	Make	Machining	
		Flange Backing Plate	1	Al 2024-T3	Make	Waterjet/Lasercut	
Bottom Platform	-	Bottom Platform	1	-	Existent	-	-
Sensing Bar	Load Cell Adaptor	Beam Load Cell	6	-	Buy	Bought	37.56
		Lever Arm	6	AISI 304	Make	Machining	978.00+IVA
		Rod End Connector	6	AISI 304	Make	Machining	
	-	Connecting Rod	6	AISI 304	Make	Machining	
		EARM-05	6	-	Existent	-	-
		EALM-O5	6	-	Existent	-	-
		Cone Spacer	24	Al 7075-T6	Existent	Machining	-
Support structure	-	Strut Tube	1	Al 7075-T6	Make	Machining	500.00*
		Lower Attachment	1	Al 7075-T6	Make	Machining	
		Upper Attatchment	1	Al 7075-T6	Make	Machining	
		Cylindrical Spacer	1	Al 7075-T6	Make	Machining	
Electrical	-	NI 9237	2	-	Existent	-	5860.00+IVA
		cDAQ-9178	1	-	Existent	-	2745.00+IVA
		UNITRONIC LiYCY 4x0,50	6	-	Existent	-	-
		UNITRONIC LiYCY 10x0,14	20	-	Buy	-	46.64
		Junction Box	1	-	Buy	-	5.40
		DB15 Female Connector	6	-	Buy	-	4.20
		DB15 Male Connector	6	-	Buy	-	2.40
		DB15 Cover	6	-	Buy	-	2.70
		RJ50 Shielded Plug	6	-	Buy	-	2.88
Force Balance							10619.78+IVA

* Estimated Cost

$5\,\mathrm{mm}$ in diameter. This device, shown in Figure 7.1, was positioned on the two original holes in the centre of the platform to drill three of the eight holes, which were then used to position the jig for the remaining holes. The central hole ($30\,\mathrm{mm}$ in diameter) was then drilled after these operations were completed.

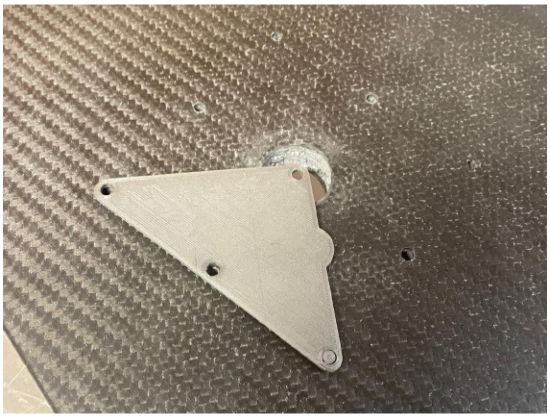

Figure 7.1: 3D printed jig to drill the additional holes on the top platform.

7.3 Subsystems Assembly

The assembly of the entire force balance, was performed by joining together all the mechanical components and electrical assemblies, as well as their connections. Since the platforms were already assembled, the remaining mechanical components to be assembled were the sensing bars, the support structure and the top platform's flange. Since the electrical components require connections to the load cells, and this is facilitated if these are not mounted on the balance, the assembly of the electrical components was performed before the mechanical assembly.

7.3.1 Electrical Assembly

The electrical connections of the force balance are comprised of all the wiring from the load cells to the DAQ, as detailed in Figure 6.4.

Before soldering any wires, the load cell wires were protected with heat shrink tubing. Afterwards, the connection between the load cell wires and the shielded four component cable was soldered. As shown in Figure 7.2a, the four individual connections were soldered and protected with heat shrink tubing. To further protect the wires and soldered connections, another layer of tubing was added to effectively form a single cable. The shielding is not connected on the load cell's side. As the shield is only grounded on one side, it avoids the flow of current through the shield which would affect the signal.

The connection of the four component cable to the DB15 male connector paid attention to the pin numbering for soldering each of the four wires. Additionally, to ensure the shielding was also connected across the connector, it was necessary to connect the shield to the metal case of the connector. To achieve this, the shield braid was unwoven and spun into a single wire, which was protected with heat shrink tubing, and soldered to the case, as shown in figure 7.2b. After the soldering was complete, the

(a) Soldering of the four wires from the load cell.

(b) Soldered connections on the DB15 male.

Figure 7.2: Soldered connections of the load cell assembly.

connector was encased with a plastic housing. On the female side of the connector, the process was fairly similar. Since this connector does not have an outer case, contrary to the male connector, and the soldered connection in each pin does not have as much contact surface for the solder to adhere, extra precautions were taken to secure the connections. As shown in Figure 7.3b, each pin soldering was protected with heat shrink tubing.

(a) 10 component cable with shielding.

(b) Soldered connections on the DB15 female.

Figure 7.3: Soldered connections inside of the connector box.

The connection to the DAQ on the other end of the ten component cable, required using an RJ50 connector. It was important to ensure that the shielding was in contact with the metal casing of the connector, otherwise the shielding would not be grounded in the DAQ.

To finalise the electrical assembly, the connector box needed to be mounted, as shown in Figure 7.4. This box is fixed on the bottom platform where the female connectors are fixed to allow a proper and quick connection between the two DB15 connector halves. A junction box was acquired to serve as the base for the connector box. The lid was cut to allow the attachment of a 3D printed part which houses the six female connectors.

7.3.2 Mechanical Assembly

Once the electrical assembly of the load cell was complete, the mechanical assembly could commence by assembling the load cell adaptors. As explained in Section 5.2.1, each load cell adapter is

(a) Glueing of the female connectors to the lid.

(b) Final assembly of the connector box.

Figure 7.4: Connector box's assembly.

comprised of two separate parts, which are bolted to the load cell, as shown in Figure 7.5. It is noteworthy that, before proceeding with the remaining assembly of the sensing bars, it is important to calibrate each of the load cells once the adapter assembly is complete since this process is simpler and more accurate than calibrating the entire bar. The reasoning behind this decision and the entire load cell calibration process are explained in detail in Section 8.1.

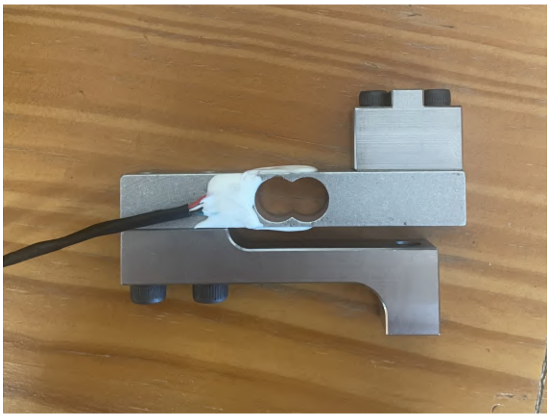

Figure 7.5: Assembly of the load cell adapter.

Once each of the load cells was calibrated, the rest of the sensing bars could be assembled, by threading the connecting rods and rod end bearings, along with the respective jamming nuts.

As the top platform was held at the correct height with the help of spacers, each sensing bar was secured with a bolt through each rod end, ensuring that the conical spacers fit correctly, locking all linear movements of the rod ends. At this point it was critical to ensure that each sensing bar was in the correct position before proceeding with the rest of the assembly. To verify the position of the top platform, a level was used on its top surface, as well as the vertical distance from to the bottom platform along the top platforms circumference. To correct any discrepancy, the length of each sensing bar was adjusted by untightening the jamming nuts of each connecting rod, twisting the rod to shorten or lengthen the bar and tightening the jamming nuts again.

To assemble the flange to the top platform, it was first necessary to assembly the flange itself by threading the threaded inserts into the top part and securing it into the bottom part. The chosen threaded inserts, depicted in Figure 7.6, are made of steel and possess locking tabs which bite into the treads of the aluminium part. To fix the inserts, they were first threaded into the top part. Once the inserts were in place, they could be secured by carefully hammering the tabs into the slots. To complete, the flange's top and base were attached using four M5 countersunk screws.


(a) Threaded inserts with locking tabs.

(b) Top part of the flange with inserts

Figure 7.6: Threaded inserts assembled in the top part of the flange.

To fix the flange to the top platform, the process was more straightforward. Using the holes which were drilled into the top platform, the flange can be bolted to the platform, ensuring the correct orientation and placing the backing plate on the bottom surface of the platform before placing the nylock nuts. To complete the assembly of the top platform, the flange's clamp is put in place and loosely secured with bolts and nuts.

The support structure designed for this project was not yet produced and thus the support structure from the force balance manufactured by Oliveira [35] was used for now on the validation of this instrument.


Figure 7.7: Final assembly of the force balance.

Chapter 8

Calibration

After assembly, it is necessary to calibrate each of the load cells, to obtain the transfer function the voltage output from each of the load cells into the axial force acting on each bar. Afterwards, it is necessary to calibrate the entire force balance, relating the forces in each of the bars to the aerodynamic loads applied at the attachment point.

It is important to note that the first step could be avoided, since the voltage output from each load cell could directly be related to the aerodynamic loads. However, this step provides crucial data to allow a metrological characterisation of the load cells to be performed. Additionally, having the exact values for the axial forces on each of the bars allows the analytical model, presented in Section 5.1.1, to be used. Although this model proves to be inaccurate since it disregards displacements, it is an important comparison tool to understand the effectiveness of the calibration procedure.

8.1 Load Cell Calibration

To calibrate a single load cell, an apparatus had to be designed in which a load cell could be mounted and axial loads, both tension and compression, could be applied. LNEC already had a calibration mechanism which could be adapted for this such purpose, as shown in Figure 8.1a, comprised of a base plate and a pulley system.

The load cell adaptor assembly is attached to the base plate by the attachment point at the lever arm. To subject the load cell to compressive loads, a 3D printed plate was bolted to the rod end attachment of the load cell allowing weights to be added and ensure that the load remains axial, as seen in Figure 8.1b. To perform the tensile loading conditions, a hook is attached to the rod end connector as illustrated in Figure 8.1c.

8.1.1 Procedure

The calibration process consisted in acquiring the voltage output while sweeping the entire measurement range. For each load cell, the calibration test was conducted 3 times, to assess the repeatability of the measurements, with each test consisting of 21 load steps.

(a) Apparatus. (b) Compression loads. (c) Tension loads.

Figure 8.1: Load cell calibration.

As the load cells have a load rating of $50\,\mathrm{N}$, in both tension and compression, the calibration test consisted in acquiring values within this range. Starting with the first load step at $0\,\mathrm{N}$, the load steps proceed with the compression in $10\,\mathrm{N}$ increments, up to $+50\,\mathrm{N}$. Once this limit is reached, the load steps decrease similar increments and continue up to the other limit, at the tensile load of $-50\,\mathrm{N}$. Afterwards, the load steps return to the initial value in the same $10\,\mathrm{N}$ increments. These 21 load steps are illustrated in Figure 8.2.

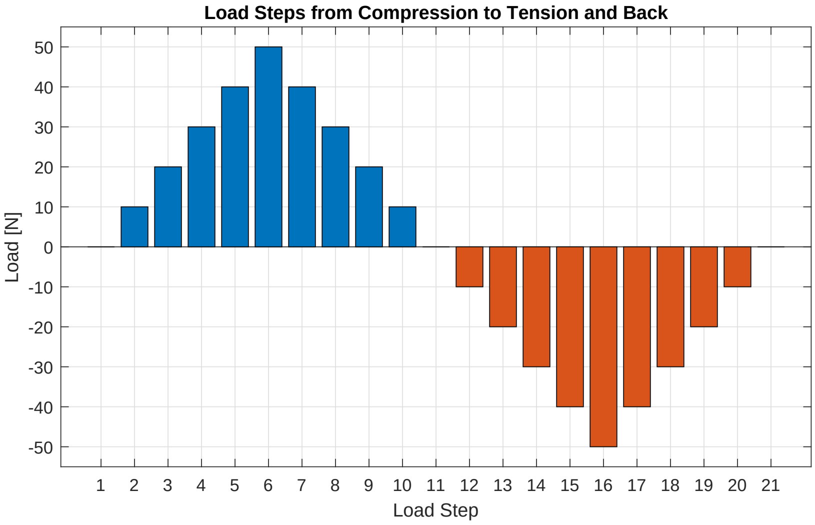

Figure 8.2: Load steps for each repetition of the load cell calibration test.

These load steps is not only cover the entire measurement range, but also provide two measurements for the same load, in both directions, that allows the estimation of the reversibility error, related to hysteresis.

8.1.2 Metrological Characterisation

The metrological characterisation is the process of assessing the accuracy and reliability of a measurement device. In this case, the objective was to assess the errors associated with the load cell and voltage measurements and estimate a measurement uncertainty. The process of achieving the errors and uncertainties is explained in detail by de Oliveira [60], which follows the recomendations of GUM - Guide to the Uncertainty in Measurement [61]. The process defines five separate sources of uncertainty: linearity, reversibility, repeatability, output voltage and excitation voltage. The adopted model relates the voltage output to the applied loads through a linear regression.

The final expanded uncertainties for each of the load cells, and the corresponding full scale percentage are presented in Table 8.1. In addition, as load cell 5 has the highest uncertainty, the complete uncertainty balance is presented in Table 8.2. The remaining uncertainty balances are shown in Annex D.

Table 8.1: Expanded uncertainties for each load cell.

Load Cell	1	2	3	4	5	6
Expanded Uncertainty (95%)	0.179 N	0.180 N	0.162 N	0.172 N	0.196 N	0.194 N
(%FS)	0.36	0.36	0.32	0.34	0.39	0.39

Table 8.2: Uncertainty balance for load cell 5.

Sources of uncertainty	Estimate	Standard uncertainty	Sensitivity coefficient	DoF	Contribution
Slope	52.9248 N/mV/V	0.0313 N/mV/V	0.9500 mV/V	2	0.030 N (9.5%)
Intercept	-0.0896 N	0.0169 N	1	2	0.017 N (3.0%)
Input Voltage	5 V	0.0055 V	-10.0557 N/V	50	0.056 N (33.2%)
Max Output Voltage	4.75 mV	0.0053 mV	10.5850 N/mV	50	0.056 N (33.8%)
Linearity	0 N	0.0417 N	1	2	0.042 N (18.6%)
Reversibility	0 N	0.0118 N	1	11	0.012 N (1.5%)
Repeatability	0 N	0.0053 N	1	23	0.005 N (0.3%)
Standard Load	50 N	0.0010 N	1	50	0.001 N (0.0%)
r(m,b)	-0.0033			22	0.002 N (0.0%)
Combined Uncertainty					0.097 N (100.0%)
Effective DoF					37
Expansion Factor					2.03
Expanded Uncertainty (95%)					0.196 N (0.39 %FS)

Despite the concerns regarding the accuracy of the beam load cells, the calibration demonstrates that given a correct calibration procedure, the load cells present low uncertainty and the results are consistent across all six load cells.

The largest contribution to the uncertainty is the estimated error of the voltage measurements. Ideally, a separate measurement of both the excitation and output voltage could provide important information such as the standard deviation of the voltage measurement of the DAQ. As this was not possible, the characterisation assumed a conservative value, estimated using the information provided in the instrument's datasheet (*NI-9237*, *National Instruments*™[62]).

8.2 Force Balance Calibration

The calibration of the entire force balance aims at relating the output from each of the sensing bars, to the actual loads being applied on the force balance. As previously stated, this can be achieved by using the raw output of the load cells (i.e. the voltage) or the measured axial force.

8.2.1 Calibrated Model

In its most basic form, the calibration intends on achieving a function which relates the outputs of each bar, r_j, to the six loads, f_i as represented by

$$f_i = f(r_1, r_2, r_3, r_4, r_5, r_6) \tag{8.1}$$

To link the outputs of each bar to the aerodynamic loads, there are multiple methods which could be used. One of these methods is using a first order polynomial which linearly relates the outputs to the loads,

$$\underbrace{f_i = \sum_{j=1}^{6} r_j c_{i,j}}_{1^{st} Order} + \epsilon_i \Leftrightarrow F = CR + \epsilon \tag{8.2}$$

where ϵ is the calibration error. In order to reduce this error, the second order polynomial can be used, which relate the loads to not only the outputs of each bar, but also to the crosswise multiplication of these outputs.

$$\underbrace{f_i = \sum_{j=1}^{6} r_j c_{i,j} + \sum_{j=1}^{6} \sum_{k=j}^{6} r_j r_k d_{i,j,k}}_{2^{nd} Order} + \epsilon_i \tag{8.3}$$

The second order polynomial expansion presents two separate sets of coefficients: $c_{i,j}$ for the direct outputs and $d_{i,j,k}$ related to the cross multiplied outputs. This model can be simplified with a single matrix of coefficients $c_{i,j}$, provided that the outputs are given in a single vector, containing the direct outputs and the cross multiplied outputs. The end result contains a coefficients matrix, denominated the calibration matrix. Given the reduced error of the second order model, the calibration of the force balance used this option.

As the intent of the calibration is to achieve the calibration matrix, the next step is to acquire the F and R vectors to solve for the coefficients, by applying known loads F to the force balance and collecting the data output from the sensing bars R. The best calibration is achieved when all possible combinations of loads are applied, but that is highly impractical, since the time needed would be unrealistic. Therefore, a set of specific load cases must be chosen to provide a close estimate of the loads the force balance is expected to register. In turn, this requires a regression to better fit the coefficients to all the load cases. One of the most appropriate methods for the regression is the Least Squares Method.

8.2.2 Least Squares Method

The Least Squares Method (LSM) [63] is a procedure which defines the best fit line to a data set. In the case of the calibration, the method takes a more generic approach, where given several functions, $f_1, \ldots, f_K$, the method finds the coefficients, $a_1, \ldots, a_K$, which forces the linear combination in Equation (8.4) to be the best fit to the data.

$$y = a_1 f_1(x) + \cdots + a_K f_K(x) \tag{8.4}$$

This method is usually chosen for calibration procedures, since it yields consistent and unbiased results while it is relatively simple and easy to comprehend. The best fit minimizes the sum of the squared errors. Given the calibration method defined in Equation (8.3), the error is given by

$$\epsilon = F - CR \tag{8.5}$$

which can be used to define a function, S, which the LSM intends to minimize.

$$S_i = \epsilon_1^2 = \left(f_i - \sum_{m=1}^{27} r_m c_{i,m} \right)^2 \tag{8.6}$$

To minimise the function, its gradient has to be zero at the minimum point. As such,

$$\frac{\partial S_i}{\partial c_{i,m}} = 0 \tag{8.7}$$

which yields a separate equation for each of the 27 outputs, r_i. These equations can be written in matrix form as

$$S = \epsilon^T \epsilon = (F - CR)^T (F - CR) = F^T F - 2C^T R^T F + C^T R^T RC \tag{8.8a}$$

$$\frac{\partial S}{\partial C} = -2R^T F + 2R^T RC = 0 \tag{8.8b}$$

$$C = (R^T R)^{-1} R^T F \tag{8.8c}$$

Equation (8.8c) is the estimator of the coefficients matrix. However, this estimator has a massive flaw, since the error ϵ was assumed constant for all the tests, which unreachable due the fact that the testing conditions change due to the hand made process and other external factors that influence the result.

8.2.3 Weighted Least Squares Method

To address the problems found in the LSM, a new matrix, W, can be introduced to add individual weights to each data point. A similar process can followed in order to achieve the estimator of the Weighted Least Squares method [64], resulting

$$S_W = \epsilon^T W \epsilon \tag{8.9a}$$

$$C = (R^T W R)^{-1} R^T W F \tag{8.9b}$$

There are multiple ways to define the weighted matrix. The simplest initial approach is to just assume that $W = I$, where I is the identity matrix. This process replicates the original LSM, which provides a general sense of the data. After a first iteration, several models could be used to construct the weights matrix. One model, described by Reis et al. [64], creates the W matrix as

$$W = V_W + D V_R D^T\ , \tag{8.10}$$

where the V_W matrix is related to the error due to the application and placement of the loads during the calibration and another matrix, V_R, relates to the uncertainties of the load cells.

V_W Matrix

The matrix V_W is a diagonal matrix of dimensions $N \times N$, where N represents the number of individual load steps on the calibration process. According to Reis et al. [64], the construction of this matrix should introduce the uncertainties related to the weights employed during the calibration, as well as errors from the resolution of the calibration system. Although the former is relatively simple, the latter is far more complex, requiring more instruments to measure the accuracy of the whole system. This step would not only add more time to the process but it would also add expenses. Therefore, an alternative approach was proposed by Ferreira [52].

This method aims at statistically approximating the contributions of the weight errors to the overall uncertainty using the standard deviation, σ_i, of each load step to the fitted value. This value can be calculated using equation 8.11, where $\hat{f}$ is the fitted values and m represents the number of inputs on the R vector

$$\sigma_i^2 = \frac{1}{N-m} \sum_{p=1}^{N} \left(f_{i,p} - \hat{f}_{i,p} \right)^2 \tag{8.11}$$

In a first iteration, the fitted values are calculated assuming $W = I$, allowing the values of the V_W matrix to be calculated for the second iteration. Once the standard deviations are calculated, the N values are placed on the diagonal the matrix.

V_R Matrix

The V_R matrix is a $6N \times 6N$ matrix which defines the uncertainty due to the readings from each sensing bar. The matrix requires repeated testing of the load cases in order to evaluate discrepancies between readings. To build this matrix, a new one containing the outputs of the load cells is required. This new matrix E, of dimensions $6N \times 3$, is composed of three columns, each one with the outputs from all the load steps, which must be repeated three times. To build each of the columns, the data from load cell 1 for all the load steps is added, followed by the data from load cells 2 through 6. Once this matrix is constructed, the final V_R matrix can be created.

To define V_R, the covariance matrix of E is obtained ($V_R = cov(E)$). This results in a square and symmetric matrix which describes the variance and covariance between the outputs of the load cells. In the diagonal, the result is the variance between the same load cell outputs, while the remaining elements, the off-diagonal ones, represent the covariance between the respective outputs.

D **Matrix**

The sensitivity matrix, D, consists in the sensitivity coefficients of the fitted model, which is given by the partial derivatives of Equation (8.3). The result a different D matrix for each os the aerodynamic loads with dimensions $N \times 6N$. Effectively, each matrix is made of 6 individual matrices of dimensions $N \times N$, each one relating to one load cell.

The general matrix presents several coefficients, $\frac{\partial f_{i,m}}{\partial r_{j,n}}$, representing the partial derivatives, where i represents the aerodynamic load, j refers to the load cell and n, m define the load step. Although the result is complex, many elements prove to be null, since the derivatives will always null if $m \neq n$. Therefore, the matrix can be simplified to

$$D_i = \begin{bmatrix} \frac{\partial f_{i,1}}{\partial r_{1,1}} & 0 & \dots & 0 & \frac{\partial f_{i,1}}{\partial r_{2,1}} & \dots & 0 & 0 \\ 0 & \frac{\partial f_{i,2}}{\partial r_{1,2}} & \dots & 0 & 0 & \dots & 0 & 0 \\ \vdots & \vdots & \ddots & \vdots & \vdots & \ddots & \vdots & \vdots \\ 0 & 0 & \dots & 0 & 0 & \dots & \frac{\partial f_{i,N-1}}{\partial r_{6,N-1}} & 0 \\ 0 & 0 & \dots & \frac{\partial f_{i,N}}{\partial r_{1,N}} & 0 & \dots & 0 & \frac{\partial f_{i,N}}{\partial r_{6,N}} \end{bmatrix} \tag{8.12}$$

8.2.4 Goodness of Fit

To evaluate the quality of the fitting of the weighted LSM, the concept of goodness of fit (GoF) can be introduced. It is evaluated using the χ^2 quantity [64] and there is a distinct value for each one of the six aerodynamic loads. To calculate the values, the most practical manner is in matrix form using

$$\chi^2 = (F - \hat{F})^T W^{-1} (F - \hat{F}) \,, \tag{8.13}$$

where F is the matrix of the applied loads and $\hat{F}$ represents the fitted values of those same loads. As before, the W matrix represents the weighted matrix, calculated for the weighted LSM.

To understand the values provided by χ^2, it is important to first introduce the concept of degrees of freedom (DoF). The DoF in the LSM represent the independent residuals after fitting the model. Since there are more data points than there are numbers of coefficients N_c (or entries in the R matrix), the number of DoF, ν, is give by

$$\nu = N - N_c \tag{8.14}$$

The χ^2 value indicates a good fit when the values tend to ν. Therefore, it is possible to create a new value to characterise the GoF, reducing χ^2 to indicate a good fit when the value is approximately 1.

$$\chi_\nu^2 = \frac{\chi^2}{\nu} \tag{8.15}$$

The values for both χ^2 and χ_ν^2 can be evaluated for each individual aerodynamic load. Thus, the fitting procedure can prove to be effective in some load and not as effective in others. This could prove that either the calibration procedure had some constraints or that the fitting model is note the most appropriate. However, it is important to make a clear distinction between the GoF and the overall quality of the calibration. Ensuring a good fit is necessary but it is not sufficient for a good calibration. Even if the fit is good, that only ensures that the method worked for the data points that were given. Therefore, a good calibration requires the appropriate set of calibration points.

8.3 Setup and Procedure

The calibration requires a system which allows for the accurate application of all six components of loads on the attachment point.

Therefore, it was necessary to create a calibration jig, as shown in Figure 8.3. The jig is composed of $20 \times 20\,\mathrm{mm}$ extruded aluminium profiles, which provides enough rigidity while maintaining low cost. In addition, a steel arm was connected at the attachment point, in order to create the necessary arm for the moments.

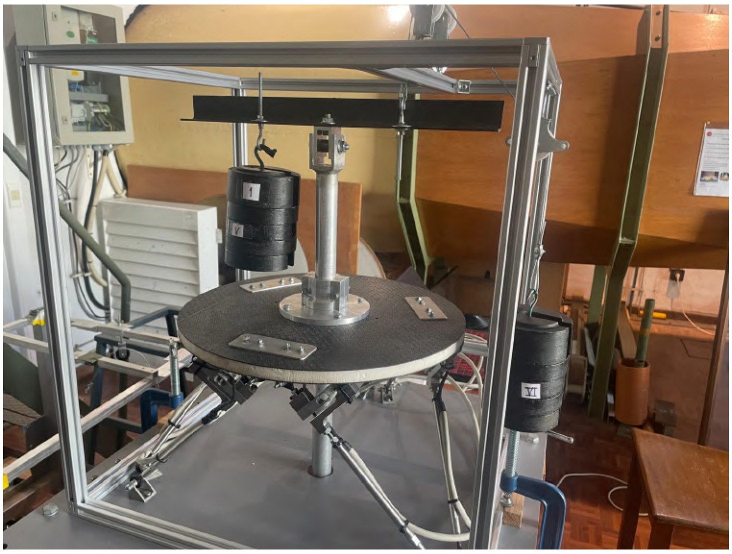

Figure 8.3: Force balance calibration jig.

Negative loads in Z are simple to apply by placing the weights, hanging from the steel arm. To apply the other force components, the pulleys and steel cables were required to pull in the required directions. To apply moments, applying a force at a certain distance from the attachment point results in a combined load, containing both force and moment. To apply pure moments, two forces are applied opposite each other at a certain distance from the centre point, as shown in Figure 8.3.

The calibration took into consideration the most common combined loads, such as those from the testing scenarios used to the define the requirements. When defining each of the load steps, it was also important to ensure that no single load cell would surpass the $50\,\mathrm{N}$ bar limit. To estimate the loads, calculations were made using the analytical model.

The load cases that were considered for this calibration were:

Pure Loads

1. Fx(+)
2. Fx(-)
3. Fy(+)
4. Fy(-)
5. Fz(+)
6. Fz(-)
7. Mx(+)
8. Mx(-)
9. My(+)
10. My(-)
11. Mz(+)
12. Mz(-)

Combined Loads

13. Fx(-) Fy(+)
14. Fx(-) Fy(-)
15. Fx(-) Fz(+)
16. Fx(-) Fz(-)
17. Fz(-) Mx(+)
18. Fz(-) Mx(-)
19. Fx(-) Mz(+)
20. Fx(-) Mz(-)
21. Fx(-) Fz(+) My(+)
22. Fx(-) Fz(+) My(-)
23. Fx(-) Fz(-) My(+)
24. Fx(-) Fz(-) My(-)

The complete load matrix, with each individual load step is in appendix E. For each individual load case, the calibration test was repeated three times without interruptions in between to reduce the chance of external interferences. For each load step, the acquisition started 10 seconds later for the readings settle, followed by 5 seconds of data acquisition. This methodical process was coordinated by the dedicated calibration user interface, which controls these times and the acquisition itself.

Once all the 72 (24×3) calibration tests were complete, the data had to be processed. A *Microsoft Excel* sheet was created to carry out this post-processing, where the initial offset was removed and averaged by individual load step. Once this step was concluded, the final data could be transported into a *MATLAB* script which complete the steps defined by the calibration model 8.2.1

8.3.1 Calibration Results

The calibration results in a calibration matrix, partially shown in Appendix E.1. Although this matrix is the most important output from the calibration, since it will allow the aerodynamic loads to be calculated, it does not directly provided any relevant information regarding the quality of the calibration.

To assess the fit of the calibrated model, the GoF was evaluated at multiple stages of the weighted LSM using the χ_ν^2 values, provided in Table 8.3. It is possible to divide the process described in 8.2.3 into three separate sections, the initial step when the original LSM is performed ($V = I$), an intermediate step where $V = V_W$ and the final step when the covariance matrix V_R is introduced $V = V_W + SV_RS^T$.

As previously mentioned, the model is considered to have a good fit when the χ_ν^2 values are close to 1. From the data, it is clear to see a decrease of these values as the iterations of the model progress, meaning that the iterated models provide a better fit than the previous ones. However, it is evident that both the F_y and F_z present values that are significantly higher than 1. This shows that the model presents a loose fit for these specific loads. Additionally, the moments present χ_ν^2 values which are much lower than the unit. Although this does not imply that the calibration is incorrect, the uncertainties on the V matrix could possibly be reduced to facilitate the fit for the forces.

To correct the aforementioned issues, multiple steps could be taken. On the model, a higher order approximation could be implemented to reduce the residual errors. Additionally, the weighted matrix could be reconsidered, applying higher costs to these loads, forcing the load to provide a closer fit for these loads in detriment of others. As previously mentioned, the GoF is not only dependent on the chosen model but is also heavily influenced by the chosen calibration points and the accuracy of the calibration process. Therefore, a more careful loading could prevent the unwanted uncertainties. However, these problem did not prove to be an issue during the testing of the force balance, as will be explored in Chapter 9.

Table 8.3: χ^2_ν values for various iterations of the weighted LSM.

Load	$W = I$	$W = V_W$	$W = V_W + DV_RD^T$
Fx	2.26	1.36	1.29
Fy	3.36	2.38	2.15
Fz	7.72	6.24	5.25
Mx	0.03	0.03	0.03
My	0.02	0.02	0.02
Mz	0.06	0.05	0.05

Calibrated Model Combined Uncertainty

The method used to calculate the uncertainty for each measurement was provided by Reis et al. [65], which aimed at defining the calibration uncertainty of a force balance. By applying this method in a *MATLAB* script, the associated uncertainty for each of the load measurements.

As an example, Table 8.4 presents the fitted value and associated uncertainty for load case 23.

Table 8.4: Fitted loads and combined uncertainties for load case 23.

Loads						Uncertainties					
Fx [N]	Fy [N]	Fz [N]	Mx [N.m]	My [N.m]	Mz [N.m]	u_{F_x} [N]	u_{F_y} [N]	u_{F_z} [N]	u_{M_x} [N.m]	u_{M_y} [N.m]	u_{M_z} [N.m]
0.00	0.00	0.00	0.00	0.00	0.00	0.11	0.12	0.16	0.04	0.04	0.02
-0.86	-0.01	-1.00	0.00	0.16	0.00	0.11	0.12	0.17	0.04	0.04	0.02
-11.53	0.09	-11.57	0.01	1.65	-0.07	0.13	0.11	0.28	0.07	0.07	0.06
-21.77	0.17	-21.88	0.02	3.13	-0.10	0.15	0.12	0.47	0.09	0.10	0.08
-31.56	0.25	-31.82	0.01	4.64	-0.11	0.17	0.14	0.67	0.12	0.12	0.10
-41.15	0.19	-51.57	-0.01	7.63	0.03	0.26	0.25	1.20	0.20	0.22	0.19
-49.65	-0.01	-70.35	-0.05	10.74	0.32	0.45	0.45	1.78	0.38	0.41	0.37

The uncertainties present an increase in magnitude as the loads also increase. This is in conformity with the expected. The results also demonstrate that the uncertainty should not be considered constant through the entire measurement range. Additionally, it is noticeable that the decoupling of the loads components is not perfect, even though the discrepancies are minute.

Chapter 9

Testing

Four distinct models were tested to evaluate the performance of the force balance. The first was a rectangular flat plate, which will be studied in detail. The other three were a larger rectangular flat plate, a flat disk and a replica of the communications antenna, which will be used to study the limitations of the design. All of the tests were conducted in the AWT, where the force balance will be mainly used.

This section will mainly focus on the flat plat test. However, the remaining tests were useful to highlight some of the potential problems of the current design. Additionally, it was possible to devise strategies to mitigate these errors.

9.1 Testing Setup

The balance was placed underneath the tunnel, as shown in Figure 9.1, and properly aligned

Figure 9.1: Force balance installation underneath the AWT.

Firstly, the force balance was leveled which required the using of a digital inclinometer and adjusting its levelling feet. Secondly, the orientation of the force balance was corrected, ensuring that the xx axis of the force balance was aligned with the axis of the tunnel, through the use of a laser beam. Additionally, the support structure was oriented using the laser beam to ensure the proper β angle.

9.2 Testing Procedure

The rectangular plate model, built by Ferreira [52], is a commonly studied body with results mentioned on specialized literature. One advantage to studying a flat plate is that the separation region does not change with airspeed, thus providing consistent results. The model is a rectangular plate of dimensions $100.7 \times 150.7\,\mathrm{mm}$ ($AR = 1.5$). The shape is fixed at the centroid to the attachment point to ensure it only generates drag and no additional load. To ensure that the plate encounters undisturbed airflow, an additional support was added to connect the attachment point to the plate, moving it upstream of the support structure, as shown in Figure 9.2.

Figure 9.2: Rectangular flat plate mounted in the AWT.

The testing procedure followed the recommendations of the force balance's user guide [53]. The model was tested at multiple air speeds, ranging from $5\,\mathrm{m/s}$ to $30\,\mathrm{m/s}$. Each model was tested twice for each individual speed. Starting at the lower speed, increasing up in defined steps up to $30\,\mathrm{m/s}$ and returning to the lower speed in the same steps, where measurements were recorded for $30\,\mathrm{s}$ on each step. The steps considered in this study are presented in Table 9.1. Note that, since steps 8 and 9 are both at $30\,\mathrm{m/s}$, the speed was increased slightly above that value before reducing back to the target value.

Table 9.1: Velocity steps and respective target velocities.

Steps	1	2	3	4	5	6	7	8	9	10	11	12	13	14	15	19
U_∞ [m/s]	5.0	6.0	7.5	10.0	12.5	15.0	20.0	30.0	30.0	20.0	15.0	12.5	10.0	7.5	6.0	5.0

It is important to be able to estimate the support structure influence on the final results so that they can be removed. Two separate methods were considered: the support structure tested without the model or to place a fairing in front of the structure, to shield it from the air flow, minimizing it's interference in the final results. While one method requires additional testing, and assumes that the testing conditions are the same for both tests, the other introduces another obstacle in the airflow, which might impact the flow on the test model. Despite this, it was chosen to proceed with the latter, by surrounding the entire support structure with a PVC tube which was attached to the tunnel's lower surface, as in Figure 9.2.

9.3 Results

Figure 9.3 presents the measured drag force for the rectangular flat plate model.

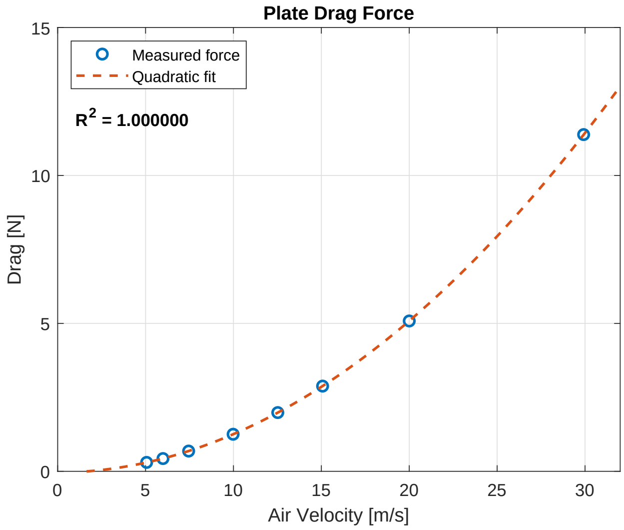

Figure 9.3: Measured drag force on the flat plate as a function of air speed.

The direct reading of the drag force allows to verify that the acquired data can be fitted with a quadratic curve with respect to the air velocity, as determined by Equation (4.1). The coefficient of determination, R^2, is higher than 0.999, proving that 99.9% of the variations in the drag force provided by variations in the air speed. However, the forces do not allow for accurate comparisons to other experimental results, since many variables can influence the actual aerodynamic loads, such as air speed, reference area or air density, which can be influenced by various factors. For this reason, it is necessary to evaluate the results using dimensionless values.

9.3.1 Dimensionless Analysis

To define the drag coefficient, C_D, it is required to define a reference area for the flat plate model. The simplest reference area and the most logical for this model is the frontal area ($S = l \times h$), which in this case has a value of $0.01518\,\mathrm{m}^2$.

Likewise, the air velocity can be analysed as a dimensionless quantity. The Reynolds number, Re, defines the ratio between inertial and viscous forces.

$$Re = \frac{\rho U_\infty L}{\mu} \tag{9.1}$$

To define Re, it is necessary to define the characteristic length L. Usually, this length is defined by a specific length of the model. In this case, the characteristic length was defined by the $\sqrt{S} = 0.1232\,\mathrm{m}$.

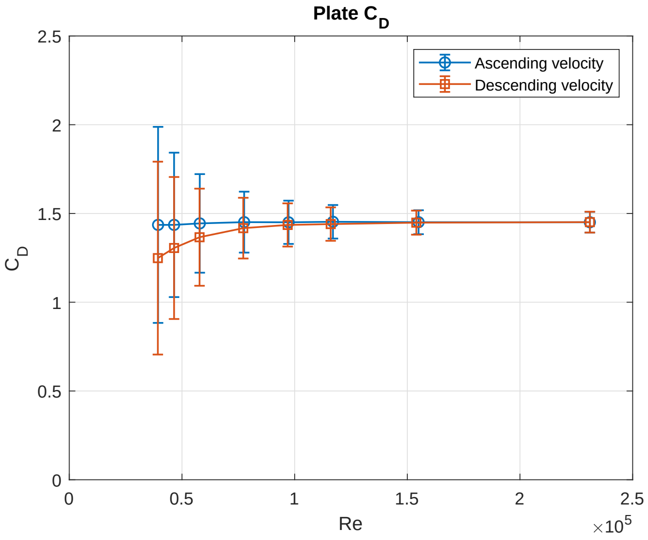

Figure 9.4: Drag coefficient of the flat plate as a function of Re.

From the results, shown in figure 9.4, it is apparent that the force balance presents a measurement error. As Re increases, the C_D values remain fairly constant, as would be expected for Re of this order os magnitude. However, as Re reduces, meaning that the air velocity is reducing, the coefficient of drag reduces, reaching significant differences at the lowest air speeds. Through the results from the other tests, it was possible to conclude that the error is systematic and will be explained later in further detail. Despite this, the results always fall within the margins of error, clearly having larger errors at lower speeds.

Given that the C_D values should remain constant, the data points acquired with ascending speeds proved to be more trustworthy than the ones in the unloading scenario. By taking the average of these points, a value of 1.45 was achieved. Classic references state that, for 3D finite rectangular flat plates, the coefficient tends to fall between 1.1 and 1.3 [50, 66, 67]. The actual value can vary depending on multiple factors, such as aspect ratio, roughness, blockage ratio, among others. However, as the support structure is placed aft of the model, its interference with the airflow can cause a change in the base pressure behind the flat plate, causing an increase in drag, as is demonstrated by several experimental tests [68, 69]. Despite this, the results proved to be consistent, highlighting the accurate and reliable performance of the force balance.

9.4 Operational Considerations

During testing, it became clear that some aspects must be taken into consideration when using the force balance. Additional models were tested, allowing a better understanding of the errors and ways to avoid them.

9.4.1 Sensitivity

One of the tested models was a flat disk plate, originally made by Ferreira [52], with $100\,\mathrm{mm}$ in diameter. The shape is fixed at the centroid to the attachment point to ensure the drag force does not create an additional moment. To ensure that the disk encounters undisturbed airflow, an additional support was added to connect the attachment point to the disk, moving it upstream of the support structure.

The testing procedure was the same as before, following the same speed steps. The dimensionless results of this test are shown in Figure 9.5b

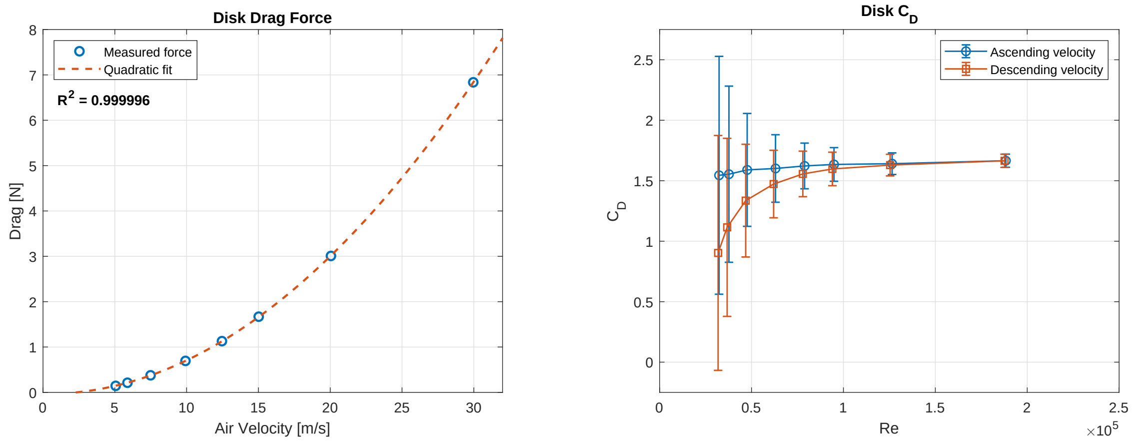

(a) Drag force as a function of air speed.

(b) Drag coefficient as a function of Re.

Figure 9.5: Results of the flat disk for various air speeds.

The results clearly show that the error associated with the measurements at low speeds is much larger than the previous ones. As the measurements reach smaller loads, the impact of the force measurement error is much greater in the final drag coefficient. Given that the disk was the smallest tested model, this problem became clearer in this test, where the smallest registered loads, shown in Figure 9.5a, were approximately $0.18\,\mathrm{N}$. As such, it is of the utmost importance to take into consideration the size of the model being tested, since minute loads will inevitably lead to untrustworthy results.

9.4.2 Reversibility Error

During the rectangular flat plate test, it was noted that the results presented an error, during the phase of descending speeds. With the additional tests of the remaining models, it is possible to conclude that the error is systematic. The most likely source of error is the force balance measurements, making the error systemic to the force balance itself.

While testing the larger rectangular plate, the air speed cycle was repeated three times to evaluate the repeatability of this error. The results, shown in Figure 9.6, present only the data from the first and second repetitions, since the third repetition's results closely matched the previous.

The results show that the response of the force balance is different in both repetitions, showing small differences between the ascending of both repetitions and descending of the second repetition,

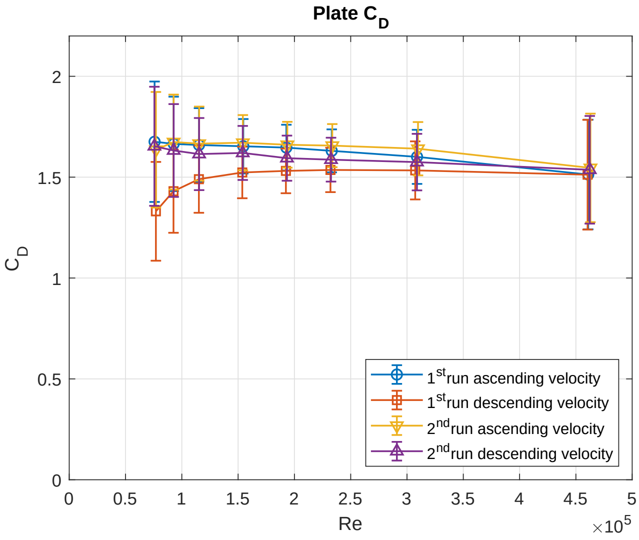

Figure 9.6: Drag coefficient of the large rectangular plate as a function of Re.

and relevant differences on the descending part of the first repetition. The first speed cycle presents a response which closely matches the previous results. On the descending part of this cycle, it was noted that the force balance presented a slight offset, which was not present when the test began and was removed before proceeding. The second cycle shows much more consistent results, similar to the results from the ascending speed of the first run and did not present an offset by the end.

One reason for this discrepancy could be the rod end bearings friction. To minimize this affect, it is recommended that, once the model is installed in the tunnel, a short cycle should be run to an air speed slightly higher than the maximum intended for the test.

9.4.3 Support Structure Interference

As previously mentioned, the support structure can influence the results, since it can also interfere with the airflow. The chosen method to prevent this interference was the introduction of a cylindrical fairing. However, through the testing of the flat plate test models, it became apparent that the fairing had an impact on the results, altering the base pressure behind the flat plate.

To verify the hypothesis, already supported by other experimental tests [68, 69], both the initial flat plat and the larger rectangular flat plate were tested using the same support configuration, which had a distance of $150\,\mathrm{mm}$ between the fairing and the plate. The two tests were then repeated with a shorter distance of $75\,\mathrm{mm}$ between the plate and the fairing, a reduction by half to replicate the results of the large plate using the smaller plate, given that the larger plate has a scale factor of 2. The comparison between the original and shorter mounting structures are shown in Figure 9.7.

The results from these tests, presented in Table 9.2, show that the reduction in length of the support structure led to an increase in the drag coefficient, proving that the interference of the fairing has a significant impact on the results. For this reason it is important to mitigate its effects.

Depending on the test model in question, the ideal strategy to mitigate the support structure's interference on the results can vary. In the tests where the model is placed directly above the support, such


(a) Original length.

(b) Shorter Length.

Figure 9.7: Comparison of the support lengths.

Table 9.2: Comparison between the test of the rectangular plate models with a shorter support.

	Rectangular Plate	Large Plate
Initial C_D	1.45	1.62
C_D with shorter support	1.55	1.64
ΔC_D	0.10	0.02

as the antenna, the fairing proved to be effective. In other tests where the model has to be placed in front of the support structure, the fairing will significantly impact the results. In these cases, other methods should be considered, such as the testing of the support structure without the model, to subtract from the final results.

9.4.4 Frequency Analyses

The antenna test model was created to test and reduce the vibrations due to wind interaction. As the air flows around the cylindrical shape, vortices are created on each side of the antenna, which detach at a specific frequency, in a phenomenon known as vortex shedding [70]. This phenomenon excites the structure by creating an oscillating lift force (F_y), which can be detected by the force balance. To determine the frequency and the amplitude of the force oscillations, the force balance has to be able to capture small vibrations at a sufficiently high frequency to capture the effects of the phenomenon.

The data acquisition from the antenna test was done at a sampling frequency $f_s = 180\,\mathrm{Hz}$. According to the Nyquist–Shannon Sampling Theorem [71], the sampling frequency should be at least twice as large as the maximum frequency in the signal. Knowing that the vortex shedding frequency is theoretically much lower than $90\,\mathrm{Hz}$ [70], the acquired data can accurately capture these oscillations. To extract the frequency and the amplitude of the force oscillations, the F_y data was introduced into *MATLAB* which performed a discrete Fourier transform of the signal, decomposing it into its sinusoidal components, giving the frequency and amplitude of each component. Figures 9.8a and 9.8b present the frequency analysis for the air speeds of $U_\infty = 6\,\mathrm{m/s}$ and $U_\infty = 30\,\mathrm{m/s}$, respectively.

From the results, it is clear that the force balance can acquire data with enough frequency and it is sufficiently sensitive to detect these oscillations. During the test of the antenna model, the structure

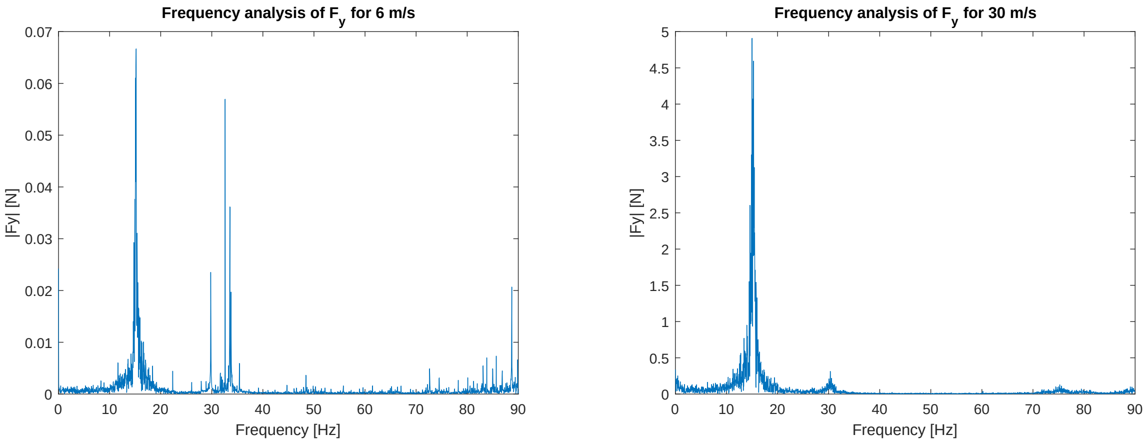

(a) $U_\infty = 6\,\mathrm{m/s}$.

(b) $U_\infty = 30\,\mathrm{m/s}$.

Figure 9.8: Frequency analysis of the amplitude of Fy for the antenna at multiple air velocities.

started to visually vibrate at $U_\infty = 10\,\mathrm{m/s}$ which progressively increased in intensity. However, as shown in the results from the test at $U_\infty = 6\,\mathrm{m/s}$, even though no vibration was visible, the force balance was able to detect two distinct frequencies on the F_y outputs. The first frequency, with larger magnitude, is roughly $15\,\mathrm{Hz}$ while the second frequency is its second harmonic with double the frequency. It is note worthy that the amplitude of these frequencies was approximately $0.06\,\mathrm{N}$, attesting to the sensitivity of the force balance.

Once the model starts to vibrate, the force balance also registers the forces related to its mechanical vibrations and not just the forces related to the vortex shedding, making it difficult to detect the shedding frequency.

Chapter 10

Conclusions

10.1 Achievements

This master's thesis aimed to design and develop a force balance for LNEC's wind tunnels, capable of measuring the six components of aerodynamic loads. One of the main constraints was adaptability, as the balance needed to operate in different tunnels and accommodate a wide range of test configurations. The result is an external force balance based on the Stewart Platform concept, which demonstrated remarkable performance throughout its full operational range.

The mechanical design emphasized minimizing manufacturing costs and reducing the mass of the components located above the load cells. To ensure compliance with the defined requirements while maintaining low mass, a finite element analysis was carried out. The results demonstrated sufficient reliability for the design purpose. However, since certain parts were reused from a previous prototype, the final configuration represents a compromise between optimal mass and the use of existing components.

Based on the defined testing scenarios, the load sensors were dimensioned using commercially available beam load cells. This choice enhanced adaptability, as the sensing range can be modified easily and at low cost. Furthermore, the use of commercial load cells and shielded cables contributed to a low measurement uncertainty. Through a metrological calibration procedure, the maximum expanded uncertainty of the load cells was determined to be below $0.2\,\mathrm{N}$, corresponding to approximately 0.4% of the FS.

The force balance was calibrated using a custom jig that applied known load cases through a system of weights, cables, and pulleys. The calibration model consists of a second-order weighted function fitted using the LSM. The weighting scheme accounts for the uncertainties of the calibration setup and the repeatability of the measurements. The uncertainty can be propagated through this model, resulting in a specific uncertainty for each load measurement.

The balance was validated using four models in six separate tests, demonstrating consistent and accurate performance. While some measured results deviated from theoretical values, these differences are attributed to the experimental setup rather than the balance itself. The testing process was facilitated by a custom-developed user interface, which enables the user to export data files efficiently, simplifying post-processing and analysis.

The final prototype is based on the Stewart platform design concept and was tailored to LNEC's needs, which would have been prohibitively expensive and less flexible if a commercial option had been selected.

In conclusion, all design requirements were met, resulting in a fully operational and adaptable force balance capable of supporting the diverse experimental needs of LNEC's wind tunnel facilities.

10.2 Future Work

Although the force balance fulfilled the defined requirements, there remain several aspects where its performance could be further enhanced.

Firstly, the technical report containing the user guide and the technical drawings of the force balance should be concluded. Only after this step is complete can the force balance be considered operational for any user.

As mentioned, the rod-end bearings should be replaced with alternative models. In addition to limiting the force balance's operational range, testing indicated that these components likely contributed to the higher than expected reversibility error. Similarly, acquiring and instrumenting load cells with higher capacity would increase the system's adaptability and extend its usable range.

The calibration process already represented a significant improvement over previous works, particularly due to the inclusion of pure moment load cases and additional calibration points. However, further refinements could be achieved with additional time and resources. Specifically, new load cases should include a wider range of combined loads, and some cases should be repeated with smaller load magnitudes to improve accuracy in the lower measurement range.

During the experimental tests, a fairing was installed to reduce the drag force acting on the model supporting structure. However, the relatively large diameter of this fairing introduced measurable aerodynamic effects. A meaningful improvement would be to design a dedicated fairing optimized for aerodynamic performance and compatibility with various test configurations.

Finally, the wind tunnel's speed control system is currently being upgraded to implement closed-loop control using a hot-wire anemometer. An effective enhancement would be to automatically record the air speed directly within the DAQ. Furthermore, integrating the tunnel control and force balance acquisition systems would allow automatic triggering and data collection for multiple speed steps, significantly streamlining the testing process.

Bibliography

[1] A. R. J. Borges. *O túnel aerodinâmico do Laboratório Nacional de Engenharia Civil.*, volume M 319 of *Memórias*. LNEC, 1969.

[2] H. Barkla. Benjamin robins and the resistance of air. *Annals of Science*, 30(1):107–122, 1973.

[3] J. Green and J. Quest. A short history of the european transonic wind tunnel etw. *Progress in Aerospace Sciences*, 47(5):319–368, 2011. doi: 10.1016/j.paerosci.2011.06.002.

[4] R. Gebbink, G. Wang, and M. Zhong. High-speed wind tunnel test of the CAE aerodynamic validation model. *Chinese Journal of Aeronautics*, 31(3):439–447, 2018. doi: 10.1016/j.cja.2018.01.010.

[5] H. Li, S. Laima, Q. Zhang, N. Li, and Z. Liu. Field monitoring and validation of vortex-induced vibrations of a long-span suspension bridge. *Journal of Wind Engineering and Industrial Aerodynamics*, 124:54–67, 2014. doi: 10.1016/j.jweia.2013.11.006.

[6] X. Li and Q. Li. Monitoring of wind effects on a super-tall building during multiple typhoons and validation of wind tunnel testing techniques. *Structure and Infrastructure Engineering*, 17(11):1535–1551, 2021. doi: 10.1080/15732479.2020.1815806.

[7] J. B. Barlow, W. H. Rae, and A. Pope. *Low-Speed Wind Tunnel Testing*. John Wiley & Sons, 3rd edition, 1999. ISBN 9780471557746.

[8] D. Bie, D. Li, J. Xiang, H. Li, Z. Kan, and Y. Sun. Design, aerodynamic analysis and test flight of a bat-inspired tailless flapping wing unmanned aerial vehicle. *Aerospace Science and Technology*, 112:106557, 2021. doi: 10.1016/j.ast.2021.106557.

[9] M. Liu, T. Maruyama, K. Sasaki, M. Inoue, M. Iguchi, and E. Fujita. Measurement of aerodynamic characteristics using cinder models through free fall experiment. *Atmosphere*, 12(5), 2021. doi: 10.3390/atmos12050608.

[10] H. Qian, Y. Niu, Y. Jiang, and P. Yan. Aerodynamic and aeroacoustic characteristics of rocket sled under strong ground effect. *International Journal of Aeroacoustics*, 23(5-6):494–514, 2024. doi: 10.1177/1475472X241259101.

[11] M. J. M. Mulkens and A. O. Ormerod. Steady-state experiments for measurements of aerodynamic stability derivatives of a high incidence research model using the college of aeronautics whirling

arm. Technical Report CoA-9014 CoA-9014, College of Aeronautics, Cranfield Institute of Technology, Cranfield, Bedford, England, August 1990. Also available via NTIS: ETN-91-99017.

[12] G. Bernardini, G. Pierfederici, J. Serafini, M. Gennaretti, and C. Ficuciello. Aerodynamic boundary element method for bluff bodies with wind tunnel data correlation. *Aerotecnica Missili & Spazio*, 95: 111–121, 2016.

[13] A. A. Fontaine, W. A. Straka, R. S. Meyer, and M. L. Jonson. A 1: 8.7 scale water tunnel verification & validation test of an axial flow water turbine. Technical report, Sandia National Lab.(SNL-NM), Albuquerque, NM (United States), 2014.

[14] W. Von Funck, T. Weinkauf, H. Theisel, and H.-P. Seidel. Smoke surfaces: An interactive flow visualization technique inspired by real-world flow experiments. *IEEE Transactions on Visualization and Computer Graphics*, 14(6):1396–1403, 2008. doi: 10.1109/TVCG.2008.163.

[15] K. Tse, P. Hitchcock, and K. Kwok. Time domain analysis technique for aerodynamic wind tunnel model studies. *Journal of Wind and Engineering*, 5:1–16, 08 2008.

[16] G. C. Rufolo, M. Marini, P. Roncioni, and S. Borrelli. In flight aerodynamic experiment for the unmanned space vehicle ftb-1. In *1st CEAS European Air and Space Conference*, Berlin, Germany, September 2007. CEAS. No DOI found / not available online.

[17] R. Sheng, L. Perret, I. Calmet, F. Demouge, and J. Guilhot. Wind tunnel study of wind effects on a high-rise building at a scale of 1:300. *Journal of Wind Engineering and Industrial Aerodynamics*, 174:391–403, 2018. doi: 10.1016/j.jweia.2018.01.017.

[18] A. R. Wittwer and S. V. Möller. Characteristics of the low-speed wind tunnel of the UNNE. *Journal of Wind Engineering and Industrial Aerodynamics*, 84(3):307–320, 2000. doi: 10.1016/S0167-6105(99)00110-5.

[19] S. A. Berry, M. N. Rhode, and K. T. Edquist. Supersonic retropropulsion experimental results from NASA Ames 9×7 foot supersonic wind tunnel. *Journal of Spacecraft and Rockets*, 51(3):724–734, 2014. doi: 10.2514/1.JSR.51.3.724.

[20] K. M. Casper, S. J. Beresh, J. F. Henfling, R. Spillers, B. Pruett, and S. P. Schneider. Hypersonic wind-tunnel measurements of boundary-layer pressure fluctuations. In *Proceedings of the 39th AIAA Fluid Dynamics Conference*, page 4054, San Antonio, TX, June 2009. American Institute of Aeronautics and Astronautics (AIAA). doi: 10.2514/6.2009-4054.

[21] R. I. Emori and D. J. Schuring. *Scale Models in Engineering: Fundamentals and Applications*. Elsevier, Oxford, UK, 1st edition, December 2013. ISBN 978-0-08-020860-2.

[22] S. Mauro, S. Brusca, R. Lanzafame, F. Famoso, A. Galvagno, and M. Messina. Small-scale open-circuit wind tunnel: Design criteria, construction and calibration. *International Journal of Applied Engineering Research*, 12(23):13649–13662, December 2017. doi: 10.37622/IJAER/12.23.2017.13649-13662.

[23] M. Jiménez-Portaz, L. Chiapponi, M. Clavero, and M. A. Losada. Air flow quality analysis of an open-circuit boundary layer wind tunnel and comparison with a closed-circuit wind tunnel. *Physics of Fluids*, 32(12):125120, December 2020. doi: 10.1063/5.0031613.

[24] F. Catalano. The new closed circuit wind tunnel of the aircraft laboratory of the university of são paulo, brazil. In *Proceedings of the 24th International Congress of the Aeronautical Sciences (ICAS 2004)*, Yokohama, Japan, August 2004. Optimage.

[25] L. Jin, X. Deng, X. Wang, J. Zhang, and W. Zeng. Review of mechanisms and suppression methods for low-frequency pressure fluctuations in open-jet wind tunnels. *Applied Sciences*, 13:10808, 09 2023. doi: 10.3390/app131910808.

[26] T. P. Chong, P. F. Joseph, and P. Davies. Design and performance of an open jet wind tunnel for aero-acoustic measurement. *Applied Acoustics*, 70(4):605–614, April 2009. doi: 10.1016/j.apacoust.2008.06.011.

[27] A. Smith, D. Mee, W. Daniel, and T. Shimoda. Design, modelling and analysis of a six component force balance for hypervelocity wind tunnel testing. *Computers & Structures*, 79(11):1077–1088, April 2001. doi: 10.1016/S0045-7949(01)00005-0.

[28] H. Psolla-Bress, H. Haselmeyer, A. Hedergott, G. Höhler, and H. Holst. High roll experiments on a delta wing in transonic flow. In *Proceedings of the 19th International Congress on Instrumentation in Aerospace Simulation Facilities (ICIASF 2001)*, page 369, Cleveland, Ohio, USA, August 2001. IEEE.

[29] B. Liu, S. Li, H. Gao, Z. Dai, and X. Hong. Suspension force measuring system for hypersonic wind tunnel test: Design and tests. *Measurement*, 143:226–233, July 2019. doi: 10.1016/j.measurement.2019.06.027.

[30] T. J. Lambert, B. Vukasinovic, and A. Glezer. A six degrees of freedom dynamic wire-driven traverse. *Aerospace*, 3(2):11, June 2016. doi: 10.3390/aerospace3020011.

[31] D. D. Cin. Design and construction of a force balance for bicycle wheel wind tunnel testing. Master's thesis, Politecnico di Milano, Milan, Italy, October 2024.

[32] A. Sextos, A. Crewe, M. Dietz, and G. Wardrop. Design of a high-performance hexapod shaking table to meet the requirements in the latest seismic qualification codes. In *17th World Conference of Earthquake Engineering*, pages 1–12, 2020.

[33] J. Fernandes. Design of a wind tunnel force balance. MSc Thesis in Aerospace Engineering, Instituto Superior Técnico, Lisboa, Portugal, June 2018.

[34] J. Pacheco. Wind tunnel testing of a complete formula student vehicle. MSc Thesis in Mechanical Engineering, Instituto Superior Técnico, Lisboa, Portugal, June 2022.

[35] A. Oliveira. Design, construction, calibration and testing of a wind tunnel force balance. MSc Thesis in Aerospace Engineering, Instituto Superior Técnico, Lisboa, Portugal, September 2020.

[36] B. Dasgupta and T. Mruthyunjaya. The stewart platform manipulator: A review. *Mechanism and Machine Theory*, 35(1):15–40, January 2000. doi: 10.1016/S0094-114X(99)00006-3.

[37] G. A. Peterson. A kinematical investigation of some external wind tunnel force measurement systems. Master's thesis, Embry-Riddle Aeronautical University, Daytona Beach, Florida, USA, October 1988.

[38] J. W. S. III. *Calibration and Uncertainty Analysis Method for a Pyramidal External Balance*. Ph.d. dissertation, Texas A&M University, College Station, Texas, USA, May 2016.

[39] K. Hoffmann. *An introduction to stress analysis and transducer design using strain gauges*. HBM Darmstadt, Germany, 2012.

[40] K. Hoffmann. *Applying the wheatstone bridge circuit*. HBM Darmstadt, Germany, 1974.

[41] C. Tropea, A. Yarin, and J. Foss. *Springer Handbook of Experimental Fluid Mechanics*. 01 2007. ISBN 9783540251415. doi: 10.1007/978-3-540-30299-5.

[42] B. Bera and M. D. Sarkar. Piezoelectric effect, piezotronics and piezophototronics: A review. *Imperial Journal of Interdisciplinary Research (IJIR)*, 2(11):1407–1410, November 2016.

[43] K. Kim, J. Kim, X. Jiang, and T. Kim. Static force measurement using piezoelectric sensors. *Journal of Sensors*, 2021, 2021. doi: 10.1155/2021/6664200.

[44] H. R. Taylor. *Data Acquisition for Sensor Systems*, volume 5. Springer Science & Business Media, Boston, MA, USA, 1997. ISBN 978-1-4419-4729-1.

[45] O. S. Vaidya and S. Kumar. Analytic hierarchy process: An overview of applications. *European Journal of Operational Research*, 169(1):1–29, February 2006. doi: 10.1016/j.ejor.2004.04.028.

[46] R. Ben-Horin, M. Shoham, and S. Djerassi. Kinematics, dynamics and construction of a planarly actuated parallel robot. *Robotics and Computer-Integrated Manufacturing*, 14(2):163–172, April 1998. doi: 10.1016/S0736-5845(97)00035-5.

[47] J. Lee. *Investigation of quality indices of in-parallel platform manipulators and development of Web-based analysis tool*. University of Florida, 2000.

[48] Laboratório Nacional de Engenharia Civil (LNEC). Wind tunnels – research infrastructures. Online at: `https://www.lnec.pt/research/research-infrastructures/wind-tunnels`. Accessed: October 2025.

[49] F. M. da Silva. Aerodynamic characterization of the 516 arouca pedestrian suspension bridge over the paiva river. *Wind*, 3(1):79–96, February 2023. doi: 10.3390/wind3010006.

[50] NASA Glenn Research Center. Shape effects on drag — drag coefficient. Accessed: October 2025.

[51] J. C. Musto. The safety factor: Case studies in engineering judgment. *International Journal of Mechanical Engineering Education*, 38(4):286–296, 2010. doi: 10.7227/IJMEE.38.4.2.

[52] M. Ferreira. Design of a six-component external wind tunnel balance. MSc Thesis in Mechanical Engineering, Instituto Superior Técnico, Lisboa, Portugal, July 2015.

[53] Balança aerodinâmica de forças de 6-componentes: Guia de utilizador. Technical report, Laboratório Nacional de Engenharia Civil, Lisboa, Portugal, 2026. Technical report, to be published.

[54] R. G. Budynas and J. K. Nisbett. *Shigley's Mechanical Engineering Design*. McGraw-Hill Series in Mechanical Engineering. McGraw-Hill Education, New York, NY, USA, 9th edition, 2011. ISBN 978-0-07-352928-8.

[55] igus GmbH. igubal® earm series rod end bearings — datasheet / product information. `https://www.igus.eu/igubal/rod-end-bearings`. Accessed: October 2025.

[56] SKF AB. Sakb 5 f rod ends with male thread — datasheet / technical specifications. `https://docs.rs-online.com/5203/A700000007406440.pdf`. Accessed: October 2025.

[57] A. Silva, J. Dias, C. T. Ribeiro, and L. Sousa. *Desenho Técnico Moderno*. Lidel, Lisboa, Portugal, 2004. ISBN 9789727573370.

[58] Dassault Systèmes. Solid mesh (SolidWorks 2024 Documentation). Available online at: `https://help.solidworks.com/2024/english/SolidWorks/cworks/c_Solid_Mesh.htm?id=56bd5f6764fb4a89926d43b50a9b49ef#Pg0`. Accessed: October 2025.

[59] Simac Electronics GmbH. Hx711-05 load cell amplifier module — datasheet. Available online at: `https://www.simac-gmbh.de/en/downloads/datasheets/HX711-05.pdf`. Accessed: October 2025.

[60] F. V. P. de Oliveira. *Sistemas semi-ativos para a mitigação de vibrações estruturais*. Tese de doutoramento em engenharia mecânica, Instituto Superior Técnico, Universidade de Lisboa, Lisboa, Portugal, 2015.

[61] BIPM, IEC, IFCC, ILAC, ISO, IUPAC, IUPAP, and OIML. Evaluation of measurement data — Guide to the expression of uncertainty in measurement. Joint Committee for Guides in Metrology (JCGM), JCGM 100:2008, 2008.

[62] National Instruments. Ni-9237 specifications / datasheet. Available online at: `https://www.ni.com/docs/en-US/bundle/ni-9237-specs/page/specs.html`. Accessed: October 2025.

[63] S. J. Miller. The method of least squares. 2006.

[64] M. Reis, R. Castro, and O. Mello. Calibration uncertainty estimation of a strain-gage external balance. *Measurement*, 46(1):24–33, 2013. doi: 10.1016/j.measurement.2012.07.019.

[65] M. L. C. C. Reis, O. A. F. Mello, and S. Uyeno. Calibration uncertainty of an external six-component wind tunnel balance. In *Proceedings of the 33rd AIAA Fluid Dynamics Conference and Exhibit*, Orlando, FL, USA, June 2003. American Institute of Aeronautics and Astronautics (AIAA). doi: 10.2514/6.2003-3884.

[66] R. Fail, J. Lawford, and R. Eyre. Low-speed experiments on the wake characteristics of flat plates normal to an air stream. *Aeronautical Research Council Reports & Memoranda*, 3120, 1957.

[67] S. F. Hoerner. *Fluid-Dynamic Drag: Theoretical, Experimental and Statistical Information*. Hoerner Fluid Dynamics, Brick Town, New Jersey, USA, 2nd edition, 1965. ISBN 9991194444. First published 1958 (1st ed.), Library of Congress Catalog Card Number 64-19666.

[68] S. G. Powers, J. K. Huffman, and J. Charles H. Fox. Flight and wind-tunnel measurements showing base drag reduction provided by a trailing disk for high reynolds number turbulent flow for subsonic and transonic mach numbers. NASA Technical Publication (NASA-TP-2638) 2638, National Aeronautics and Space Administration, Scientific and Technical Information Branch, Edwards, California / Hampton, Virginia, USA, November 1986. Dryden Flight Research Facility, Ames Research Center; Langley Research Center.

[69] B. Hetherington. *Interference of Supports Used for Ground Vehicle Wind Tunnel Testing*. PhD thesis, Durham Thesis, Durham University., (2006).

[70] R. King. A review of vortex shedding research and its application. *Ocean Engineering*, 4(3):141–171, 1977. doi: 10.1016/0029-8018(77)90002-6.

[71] C. E. Shannon. Communication in the presence of noise. *Proceedings of the IRE*, 37(1):10–21, 1949. doi: 10.1109/JRPROC.1949.232969.

Appendix A

Requirements Definition

Table A.1: Requirements and Respective Verification and Validation Processes.

ID	**Level**	**Subsystem**	**Component**	**Type**	**Requirement**	**Design Verification**	**Validation Process**
O.C.1	System	-	-	Concept	The force balance needs to measure 6 degrees of freedom (3 forces and 3 moments).	-	-
O.C.2	System	-	-	Concept	The force balance should be based on the stewart platform concept.	-	-
O.A.1	System	-	-	Adaptability	The force balance needs to be usable in LNEC's aeronautical and boundary layer wind tunnels.	-	-
O.P.1	System	-	-	Performance	The force balance must have a minimum resolution of 0.2N for all forces.	Load cells adequate for the loads at the sensing bars according to FEM analysis	Testing after calibration
O.P.1	System	-	-	Performance	The force balance must have a minimum resolution of 0.04Nm for all moments.	Load cells adequate for the loads at the sensing bars according to FEM analysis	Testing after calibration
E.C.1	Subsystem	Electrical	-	Concept	The load sensors must be commercially available load cells.	-	-
M.A.1	Subsystem	Mechanical	-	Adaptability	The mechanical attachment needs to be usable for multiple models.	-	-
M.A.2	Subsystem	Mechanical	-	Adaptability	The force balance needs to allow for adjustments in the angle of attack and the yaw angle up to 45 degrees in each direction.	CAD	Measurement after construction
M.P.1	Subsystem	Mechanical	-	Performance	The linear displacement of the model must have a maximum of $10\,\mathrm{mm}$ when any of the load cases are applied.	FEM Analysis	Validation of load cases 1 and 2 during calibration
M.P.2	Subsystem	Mechanical	-	Performance	The angular displacement of the model must have a maximum of 2 degrees when any of the load cases are applied.	FEM Analysis	Validation of load cases 1 and 2 during calibration
M.S.1	Subsystem	Mechanical	-	Safety	The safety factor to be applied on all load cases for the FEM analysis must be 1.45.	-	-
M.S.2	Component	Mechanical	Sensing Bars	Safety	The maximum axial force on a sensing bar should not exceed 60% of the yield force.	FEM Analysis	Data collected from the load cells during
M.S.3	Component	Mechanical	Sensing Bars	Safety	The maximum axial force on a sensing bar should not exceed 70% of the critical buckling force.	FEM Analysis	Data collected from the load cells during

Table A.2: Calculation of the weights of the criteria.

	A	B	C	D	E	F	G	H	I	J	K	L	Weight
A	1	2	1/3	1	1/2	6	1/5	1/4	1/2	1/7	1/2	1/7	0.035
B	1/2	1	1/3	1/4	1/2	5	1/5	1/4	1/3	1/6	2	1/7	0.031
C	3	3	1	3	2	5	1/3	1/2	1/2	1/5	2	1/5	0.065
D	1	4	1/3	1	1/4	4	1/5	1/3	1/3	1/5	2	1/6	0.040
E	2	2	1/2	4	1	6	1/3	1/3	1	1/2	4	1/3	0.072
F	1/6	1/5	1/5	1/4	1/6	1	1/6	1/7	1/5	1/7	1/3	1/7	0.014
G	5	5	3	5	3	6	1	1/3	1/2	1/3	3	1/4	0.102
H	4	4	2	3	3	7	3	1	1	1/3	4	1	0.123
I	2	3	2	3	1	5	2	1	1	1/3	5	1/3	0.091
J	7	6	5	5	2	7	3	3	3	1	6	2	0.215
K	2	1/2	1/2	1/2	1/4	3	1/3	1/4	1/5	1/6	1	1/6	0.029
L	7	7	5	6	3	7	4	1	3	1/2	6	1	0.186

$$\begin{bmatrix} 1 & 1/2 & 1/7 & 1/4 & 1/3 & 1/4 \\ 2 & 1 & 1/4 & 1/3 & 1 & 1/4 \\ 7 & 4 & 1 & 3 & 4 & 2 \\ 4 & 3 & 1/3 & 1 & 2 & 1 \\ 3 & 1 & 1/4 & 1/2 & 1 & 1/3 \\ 4 & 4 & 1/2 & 1 & 3 & 1 \end{bmatrix}$$

(a) Robustness

$$\begin{bmatrix} 1 & 4 & 8 & 7 & 3 & 2 \\ 1/4 & 1 & 5 & 4 & 1/2 & 1/3 \\ 1/8 & 1/5 & 1 & 1/3 & 1/5 & 1/7 \\ 1/7 & 1/4 & 3 & 1 & 1/3 & 1/5 \\ 1/3 & 2 & 5 & 3 & 1 & 1/3 \\ 1/2 & 3 & 7 & 5 & 3 & 1 \end{bmatrix}$$

(b) Simplicity

$$\begin{bmatrix} 1 & 4 & 6 & 5 & 7 & 4 \\ 1/4 & 1 & 5 & 4 & 6 & 3 \\ 1/6 & 1/5 & 1 & 1/3 & 2 & 1/4 \\ 1/5 & 1/4 & 3 & 1 & 3 & 1/3 \\ 1/4 & 1/6 & 1/2 & 1/3 & 1 & 1/5 \\ 1/3 & 1/3 & 4 & 3 & 5 & 1 \end{bmatrix}$$

(c) Fabrication

$$\begin{bmatrix} 1 & 1/2 & 3 & 3 & 1/3 & 1/4 \\ 2 & 1 & 2 & 2 & 1/3 & 1/3 \\ 1/3 & 1/2 & 1 & 1 & 1/5 & 1/5 \\ 1/3 & 1/2 & 1 & 1 & 1/5 & 1/5 \\ 3 & 3 & 5 & 5 & 1 & 1/2 \\ 4 & 3 & 5 & 5 & 2 & 1 \end{bmatrix}$$

(d) Instrumentation

$$\begin{bmatrix} 1 & 2 & 4 & 3 & 9 & 9 \\ 1/2 & 1/4 & 3 & 3 & 9 & 9 \\ 1/4 & 1/3 & 1 & 1/2 & 8 & 8 \\ 1/3 & 1/3 & 2 & 1 & 9 & 9 \\ 1/9 & 1/9 & 1/8 & 1/9 & 1 & 1 \\ 1/9 & 1/9 & 1/8 & 1/9 & 1 & 1 \end{bmatrix}$$

(e) Structurally Adaptable

$$\begin{bmatrix} 1 & 1/2 & 1/4 & 1/5 & 1/8 & 1/7 \\ 2 & 1 & 1/3 & 1/4 & 1/7 & 1/6 \\ 4 & 3 & 1 & 1/2 & 1/6 & 1/5 \\ 5 & 4 & 2 & 1 & 1/5 & 1/4 \\ 8 & 7 & 6 & 5 & 1 & 1/2 \\ 7 & 6 & 5 & 4 & 2 & 1 \end{bmatrix}$$

(f) Innovative Design

$$\begin{bmatrix} 1 & 4 & 8 & 8 & 5 & 4 \\ 1/4 & 1 & 5 & 5 & 4 & 3 \\ 1/8 & 1/5 & 1 & 1/2 & 1/3 & 1/5 \\ 1/8 & 1/5 & 2 & 1 & 1/2 & 1/3 \\ 1/5 & 1/4 & 3 & 2 & 1 & 1/2 \\ 1/4 & 1/3 & 5 & 3 & 2 & 1 \end{bmatrix}$$

(g) Cost

$$\begin{bmatrix} 1 & 3 & 3 & 3 & 8 & 7 \\ 1/3 & 1 & 1 & 1 & 7 & 6 \\ 1/3 & 1 & 1 & 1 & 6 & 5 \\ 1/3 & 1 & 1 & 1 & 6 & 5 \\ 1/8 & 1/7 & 1/6 & 1/6 & 1 & 1/2 \\ 1/7 & 1/6 & 1/5 & 1/5 & 2 & 1 \end{bmatrix}$$

(h) Wind Tunnel Attachment

$$\begin{bmatrix} 1 & 1 & 1/2 & 1/2 & 1/2 & 7 \\ 1 & 1 & 1/2 & 1/2 & 1/2 & 7 \\ 2 & 2 & 1 & 1 & 1/3 & 5 \\ 2 & 2 & 1 & 1 & 1 & 8 \\ 2 & 2 & 3 & 1 & 1 & 7 \\ 1/7 & 1/7 & 1/5 & 1/8 & 1/7 & 1 \end{bmatrix}$$

(i) Support Versatility

$$\begin{bmatrix} 1 & 1/5 & 1/6 & 1/5 & 1/2 & 1/4 \\ 5 & 1 & 1/2 & 1 & 4 & 3 \\ 6 & 2 & 1 & 2 & 4 & 3 \\ 5 & 1 & 1/2 & 1 & 3 & 2 \\ 2 & 1/4 & 1/4 & 1/3 & 1 & 1/3 \\ 4 & 1/3 & 1/3 & 1/2 & 3 & 1 \end{bmatrix}$$

(j) Measurement Accuracy

$$\begin{bmatrix} 1 & 1/6 & 1/7 & 1/7 & 1/2 & 1 \\ 6 & 1 & 1/2 & 1/2 & 3 & 2 \\ 7 & 2 & 1 & 1 & 3 & 2 \\ 7 & 2 & 1 & 1 & 3 & 2 \\ 2 & 1/3 & 1/3 & 1/3 & 1 & 1 \\ 1 & 1/2 & 1/2 & 1/2 & 1 & 1 \end{bmatrix}$$

(k) Force and Torque Decoupling

$$\begin{bmatrix} 1 & 1/2 & 1/2 & 3 & 1 & 1 \\ 2 & 1 & 1 & 4 & 2 & 2 \\ 2 & 1 & 1 & 3 & 2 & 2 \\ 5 & 1/5 & 1/4 & 1 & 1/2 & 1/2 \\ 1 & 1/2 & 1/2 & 2 & 1 & 1 \\ 1 & 1/2 & 1/2 & 2 & 1 & 1 \end{bmatrix}$$

(l) Results Processing

Figure A.1: AHP criteria evaluation matrices.

Table A.3: AHP final scores for each design.

Design	A	B	C	D	E	F	G	H	I	J	K	J	Final Score
Platform	0.04	0.38	0.43	0.12	0.39	0.03	0.46	0.40	0.13	0.04	0.05	0.14	0.217
Rotating Platform	0.08	0.12	0.24	0.13	0.24	0.05	0.23	0.18	0.13	0.23	0.20	0.25	0.205
Pyramidal	0.38	0.03	0.05	0.06	0.14	0.09	0.04	0.17	0.19	0.34	0.28	0.24	0.197
Pyramidal Platform	0.18	0.06	0.09	0.06	0.18	0.13	0.05	0.17	0.24	0.20	0.28	0.12	0.152
Innovative 1	0.09	0.14	0.04	0.28	0.03	0.33	0.08	0.03	0.28	0.07	0.09	0.13	0.106
Innovative 2	0.22	0.27	0.16	0.37	0.03	0.37	0.14	0.04	0.03	0.13	0.10	0.13	0.123

$\alpha[°]$	NACA 2414				NACA 6516			
	C_L	C_D	C_m	X_{C_p}	C_L	C_D	C_m	X_{C_p}
0	0.2396	0.00548	-0.0524	0.4674	0.7695	0.00696	-0.1800	0.4819
1	0.3480	0.00528	-0.0516	0.3955	0.8788	0.00705	-0.1796	0.4508
2	0.4531	0.00526	-0.0495	0.3557	0.9856	0.00723	-0.1788	0.4262
3	0.5689	0.00566	-0.0499	0.3333	1.0891	0.00746	-0.1774	0.4062
4	0.7098	0.00634	-0.0565	0.3244	1.1810	0.00725	-0.1734	0.3888
5	0.8135	0.00729	-0.0553	0.3118	1.2718	0.00801	-0.1695	0.3738
6	0.9051	0.00856	-0.0515	0.2998	1.3603	0.00895	-0.1654	0.3606
7	0.9993	0.01002	-0.0486	0.2905	1.4416	0.01022	-0.1603	0.3486
8	1.0962	0.01135	-0.0463	0.2829	1.5160	0.01183	-0.1544	0.3376
9	1.1919	0.01270	-0.0439	0.2762	1.5804	0.01402	-0.1472	0.3272
10	1.2841	0.01417	-0.0411	0.2700	1.6300	0.01715	-0.1385	0.3172
11	1.3671	0.01608	-0.0370	0.2635	1.6694	0.02111	-0.1294	0.3078
12	1.4461	0.01766	-0.0324	0.2572	1.6971	0.02631	-0.1200	0.2990
13	1.5065	0.01996	-0.0254	0.2500	1.7226	0.03233	-0.1118	0.2912
14	1.5413	0.02421	-0.0170	0.2424	1.7442	0.03922	-0.1047	0.2841
15	1.5849	0.02851	-0.0120	0.2370	1.7636	0.04689	-0.0988	0.2778
16	1.6094	0.03528	-0.0083	0.2324	1.7775	0.05564	-0.0939	0.2723
17	1.6142	0.04529	-0.0071	0.2293	1.7867	0.06513	-0.0898	0.2673
18	1.5956	0.05962	-0.0092	0.2283	1.7898	0.07594	-0.0870	0.2630
19	1.5545	0.07844	-0.0147	0.2294	1.7834	0.08807	-0.0851	0.2595
20	1.4896	0.10253	-0.0240	0.2335	1.7709	0.10125	-0.0845	0.2568
21	1.4145	0.12966	-0.0363	0.2406	1.7626	0.11420	-0.0854	0.2548
22	1.3410	0.15849	-0.0517	0.2512	1.7398	0.12936	-0.0882	0.2541
23	1.2760	0.18857	-0.0699	0.2652	1.7119	0.14546	-0.0929	0.2546
24	1.2121	0.22278	-0.0918	0.2845	1.7041	0.15901	-0.0984	0.2549
25	1.0696	0.31369	-0.1391	0.3440	1.6874	0.17439	-0.1061	0.2568

Table A.4: Aerodynamic coefficients of different foils for the half wing model.

Variable		B = VG	B = G	B = F	B = P
A = VG	C = VG	1.10	1.30	1.50	1.70
	C = G	1.20	1.45	1.70	1.95
	C = F	1.30	1.60	1.90	2.20
	C = P	1.40	1.75	2.10	2.45
A = G	C = VG	1.30	1.55	1.80	2.05
	C = G	1.45	1.75	2.05	2.35
	C = F	1.60	1.95	2.30	2.65
	C = P	1.75	2.15	2.55	2.95
A = F	C = VG	1.50	1.80	2.10	2.40
	C = G	1.70	2.05	2.40	2.75
	C = F	1.90	2.30	2.70	3.10
	C = P	2.10	2.55	3.00	3.45
A = P	C = VG	1.70	2.15	2.40	2.75
	C = G	1.95	2.35	2.75	3.15
	C = F	2.20	2.65	3.10	3.55
	C = P	2.45	2.95	3.45	3.95

Table A.5: Values for the N_1 factor for Pugsley's method.

Characteristic	E = NS	E = S	E = VS
D = NS	1.0	1.0	1.2
D = S	1.2	1.3	1.4
D = VS	1.4	1.5	1.6

Table A.6: Values for the N_2 factor for Pugsley's method.

Appendix B

Technical Drawings

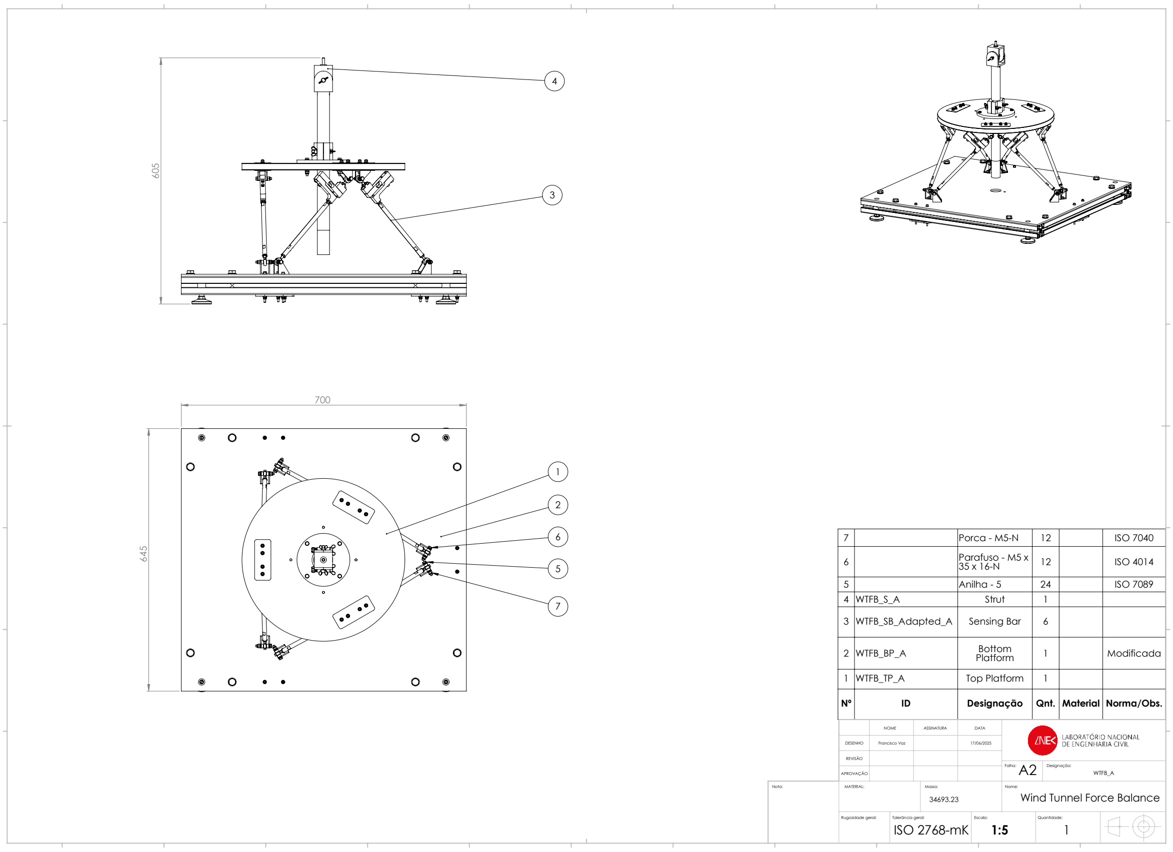

Nº	ID	Designação	Qnt.	Material	Norma/Obs.
7		Porca - M5-N	12		ISO 7040
6		Parafuso - M5 x 35 x 16-N	12		ISO 4014
5		Anilha - 5	24		ISO 7089
4	WTFB_S_A	Strut	1		
3	WTFB_SB_Adapted_A	Sensing Bar	6		
2	WTFB_BP_A	Bottom Platform	1		Modificada
1	WTFB_TP_A	Top Platform	1		

	NOME	ASSINATURA	DATA
DESENHO	Francisco Vaz		17/06/2025
REVISÃO			
APROVAÇÃO			

LABORATÓRIO NACIONAL DE ENGENHARIA CIVIL

Folha: A2

Designação: WTFB_A

Nota:

MATERIAL:

Massa: 34693.23

Nome: Wind Tunnel Force Balance

Rugosidade geral:

Tolerância geral: ISO 2768-mK

Escala: **1:5**

Quantidade: 1

Figure B.1: Technical drawing of the force balance assembly.

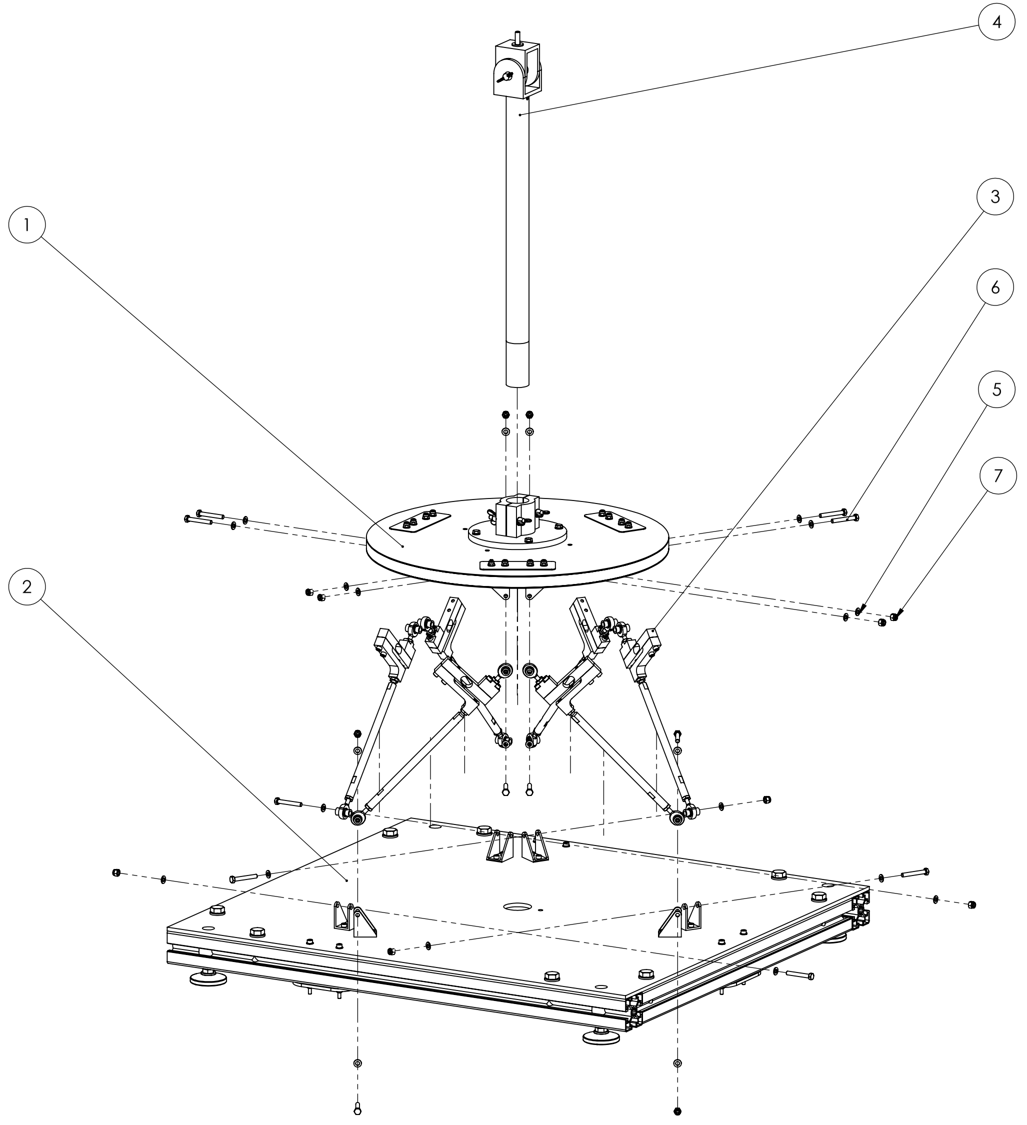

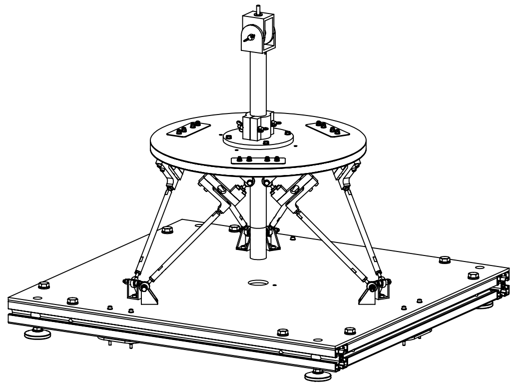

Nº	ID	Designação	Qnt.	Material	Norma/Obs.
7		Porca - M5-N	12		ISO 7040
6		Parafuso - M5 x 35 x 16-N	12		ISO 4014
5		Anilha - 5	24		ISO 7089
4	WTFB_S_A	Strut	1		
3	WTFB_SB_Adapted_A	Sensing Bar	6		
2	WTFB_BP_A	Bottom Platform	1		Modificada
1	WTFB_TP_A	Top Platform	1		

	NOME	ASSINATURA	DATA
DESENHO	Francisco Vaz		17/06/2025
REVISÃO			
APROVAÇÃO			

LABORATÓRIO NACIONAL
DE ENGENHARIA CIVIL

Folha: A2

Designação: WTFB_A

Nota:

MATERIAL:

Massa: 34693.23

Nome: Wind Tunnel Force Balance

Rugosidade geral:

Tolerância geral: ISO 2768-mK

Escala: 1:5

Quantidade: 1

Appendix C

FEM Results

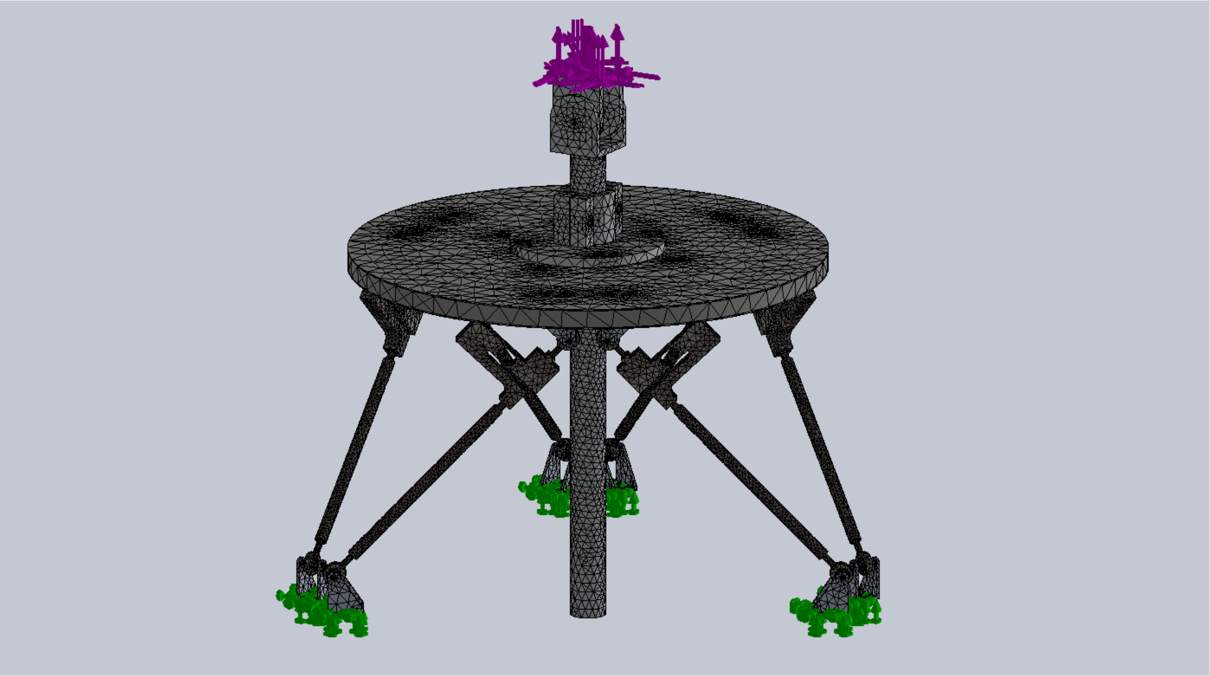

Figure C.1: Chosen mesh for the FEM simulations.

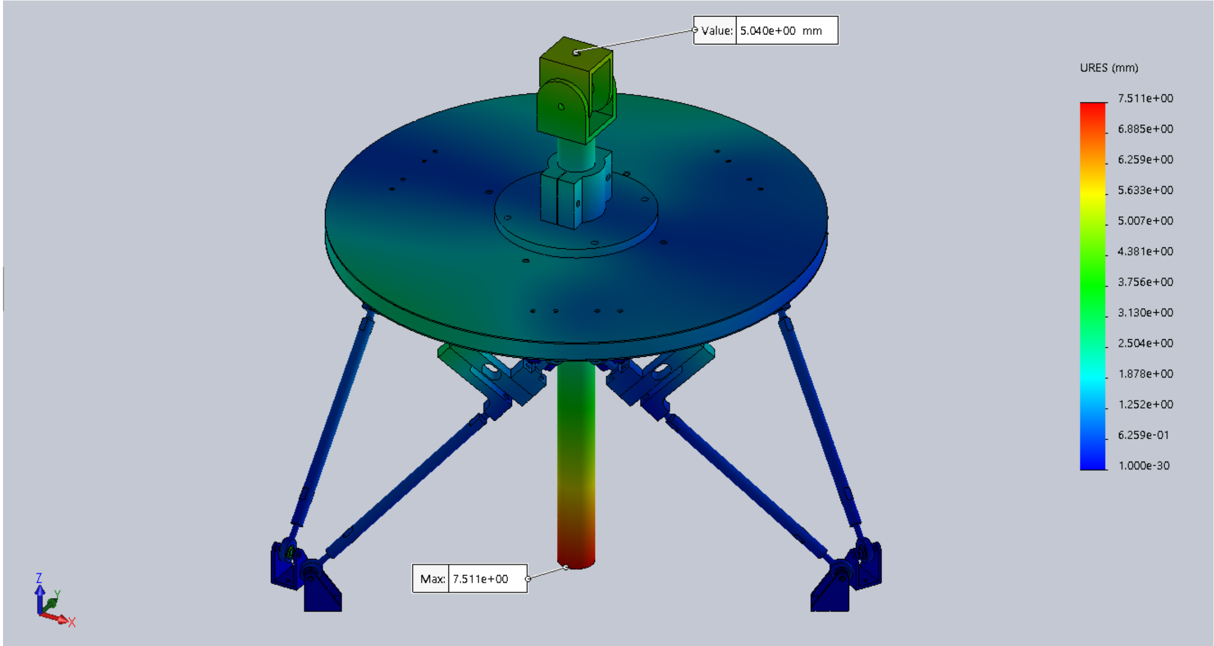

Figure C.2: Displacement plot for the wing load case.

Appendix D

Load Cell Characterisation

Load Cell 1

Table D.1: Uncertainty balance for load cell 1.

Sources of uncertainty	Estimate	Standard uncertainty	Sensitivity coefficient	DoF	Contribution
Slope	49.9200 N/mV/V	0.0225 N/mV/V	1.004 mV/V	2	0.023 N (9.5%)
Intercept	-0.0692 N	0.0128 N	1	2	0.013 N (3.0%)
Input Voltage	5 V	0.0056 V	-10.0239 N/V	50	0.056 N (33.2%)
Max Output Voltage	5.02 mV	0.0056 mV	9.9840 N/mV	50	0.056 N (33.8%)
Linearity	0 N	0.0306 N	1	2	0.031 N (18.6%)
Reversibility	0 N	0.0094 N	1	11	0.009 N (1.5%)
Repeatability	0 N	0.0074 N	1	23	0.007 N (0.3%)
Standard Load	50 N	0.0010 N	1	50	0.001 N (0.0%)
r(m,b)	-0.0029			22	0.001 N (0.0%)
Combined Uncertainty					0.090 N (100.0%)
Effective DoF					65
Expansion Factor					2.00
Expanded Uncertainty (95%)					0.179 N (0.36 %FS)

Load Cell 2

Table D.2: Uncertainty balance for load cell 2.

Sources of uncertainty	Estimate	Standard uncertainty	Sensitivity coefficient	DoF	Contribution
Slope	51.5337 N/mV/V	0.0230 N/mV/V	0.9740 mV/V	2	0.022 N (6.2%)
Intercept	-0.0524 N	0.0127 N	1	2	0.013 N (2.0%)
Input Voltage	5 V	0.0056 V	-10.0388 N/V	50	0.056 N (38.5%)
Max Output Voltage	4.87 mV	0.0054 mV	10.3067 N/mV	50	0.056 N (38.9%)
Linearity	0 N	0.0310 N	1	2	0.031 N (11.9%)
Reversibility	0 N	0.0075 N	1	11	0.007 N (0.7%)
Repeatability	0 N	0.0122 N	1	23	0.012 N (1.8%)
Standard Load	50 N	0.0010 N	1	50	0.001 N (0.0%)
r(m,b)	-0.0022			22	0.001 N (0.0%)
Combined Uncertainty					0.090 N (100.0%)
Effective DoF					65
Expansion Factor					2.00
Expanded Uncertainty (95%)					0.180 N (0.36 %FS)

Load Cell 3

Table D.3: Uncertainty balance for load cell 3.

Sources of uncertainty	Estimate	Standard uncertainty	Sensitivity coefficient	DoF	Contribution
Slope	53.2402 N/mV/V	0.0121 N/mV/V	0.9400 mV/V	2	0.011 N (1.9%)
Intercept	0.0111 N	0.0064 N	1	2	0.006 N (0.6%)
Input Voltage	5 V	0.0055 V	-10.0091 N/V	50	0.055 N (46.0%)
Max Output Voltage	4.70 mV	0.0053 mV	10.6480 N/mV	50	0.056 N (47.1%)
Linearity	0 N	0.0140 N	1	2	0.014 N (2.9%)
Reversibility	0 N	0.0068 N	1	11	0.007 N (0.7%)
Repeatability	0 N	0.0064 N	1	23	0.006 N (0.6%)
Standard Load	50 N	0.0010 N	1	50	0.001 N (0.0%)
r(m,b)	0.0000			22	0.000 N (0.0%)
Combined Uncertainty					0.081 N (100.0%)
Effective DoF					107
Expansion Factor					1.98
Expanded Uncertainty (95%)					0.162 N (0.32 %FS)

Load Cell 4

Table D.4: Uncertainty balance for load cell 4.

Sources of uncertainty	Estimate	Standard uncertainty	Sensitivity coefficient	DoF	Contribution
Slope	51.8930 N/mV/V	0.0189 N/mV/V	0.9660 mV/V	2	0.018 N (4.4%)
Intercept	-0.0614 N	0.0104 N	1	2	0.010 N (1.4%)
Input Voltage	5 V	0.0056 V	-10.0257 N/V	50	0.056 N (41.3%)
Max Output Voltage	4.83 mV	0.0054 mV	10.3786 N/mV	50	0.056 N (41.8%)
Linearity	0 N	0.0268 N	1	2	0.027 N (9.6%)
Reversibility	0 N	0.0060 N	1	11	0.006 N (0.5%)
Repeatability	0 N	0.0083 N	1	23	0.008 N (0.9%)
Standard Load	50 N	0.0010 N	1	50	0.001 N (0.0%)
r(m,b)	-0.0026			22	0.001 N (0.0%)
Combined Uncertainty					0.087 N (100.0%)
Effective DoF					79
Expansion Factor					1.99
Expanded Uncertainty (95%)					0.172 N (0.34 %FS)

Load Cell 6

Table D.5: Uncertainty balance for load cell 6.

Sources of uncertainty	Estimate	Standard uncertainty	Sensitivity coefficient	DoF	Contribution
Slope	50.7480 N/mV/V	0.0283 N/mV/V	0.9900 mV/V	2	0.028 N (8.6%)
Intercept	-0.0899 N	0.0159 N	1	2	0.016 N (2.8%)
Input Voltage	5 V	0.0056 V	-10.0481 N/V	50	0.056 N (34.3%)
Max Output Voltage	4.95 mv	0.0055 mV	10.1496 N/mV	50	0.056 N (34.5%)
Linearity	0 N	0.0418 N	1	2	0.042 N (19.1%)
Reversibility	0 N	0.0063 N	1	11	0.006 N (0.4%)
Repeatability	0 N	0.0054 N	1	23	0.005 N (0.3%)
Standard Load	50 N	0.0010 N	1	50	0.001 N (0.0%)
r(m,b)	-0.0032			22	0.002 N (0.0%)
Combined Uncertainty					0.096 N (100.0%)
Effective DoF					37
Expansion Factor					2.03
Expanded Uncertainty (95%)					0.194 N (0.39 %FS)

Appendix E

Force Balance Calibration

$$C = \begin{bmatrix} 0.627 & 0.643 & -0.635 & 0.009 & -0.003 & -0.644 & \ldots & 0.018 & 0.017 \\ 0.395 & -0.396 & 0.383 & 0.694 & -0.711 & -0.400 & \ldots & 0.019 & -0.014 \\ -0.812 & -0.722 & -0.750 & -0.755 & -0.710 & -0.716 & \ldots & 0.211 & 0.029 \\ 0.198 & -0.205 & 0.003 & 0.204 & -0.208 & -0.005 & \ldots & -0.004 & 0.001 \\ -0.116 & -0.118 & 0.239 & -0.112 & -0.110 & 0.237 & \ldots & 0.001 & 0.002 \\ 0.104 & -0.108 & 0.106 & -0.107 & 0.111 & -0.108 & \ldots & -0.009 & 0.005 \end{bmatrix}_{6\times 27} \tag{E.1}$$

Table E.1: Pure forces (F_x,F_y) load cases

Load Case	Load Step	Fx [N]	Fy [N]	Fz [N]	Mx [N.m]	My [N.m]	Mz [N.m]
Fx(+)	1	0	0	0	0	0	0
	2	1.0	0	0	0	0	0
	3	11.0	0	0	0	0	0
	4	21.0	0	0	0	0	0
	5	31.0	0	0	0	0	0
	6	41.0	0	0	0	0	0
	7	51.0	0	0	0	0	0
	8	61.0	0	0	0	0	0
	9	71.0	0	0	0	0	0
Fx(-)	10	0	0	0	0	0	0
	11	-1.0	0	0	0	0	0
	12	-11.0	0	0	0	0	0
	13	-21.0	0	0	0	0	0
	14	-31.0	0	0	0	0	0
	15	-41.0	0	0	0	0	0
	16	-51.0	0	0	0	0	0
Fy(+))	17	0	0	0	0	0	0
	18	0	1.0	0	0	0	0
	19	0	11.0	0	0	0	0
	20	0	21.0	0	0	0	0
	21	0	31.0	0	0	0	0
	22	0	41.0	0	0	0	0
	23	0	51.0	0	0	0	0
	24	0	61.0	0	0	0	0
	25	0	71.0	0	0	0	0

Table E.2: Pure forces (F_y,F_z) load cases

Load Case	Load Step	Fx [N]	Fy [N]	Fz [N]	Mx [N.m]	My [N.m]	Mz [N.m]
Fy(-)	26	0	0	0	0	0	0
	27	0	-1.0	0	0	0	0
	28	0	-11.0	0	0	0	0
	29	0	-21.0	0	0	0	0
	30	0	-31.0	0	0	0	0
	31	0	-41.0	0	0	0	0
	32	0	-51.0	0	0	0	0
	33	0	-61.0	0	0	0	0
	34	0	-71.0	0	0	0	0
Fz(+)	35	0	0	0	0	0	0
	36	0	0	2.0	0	0	0
	37	0	0	22.0	0	0	0
	38	0	0	42.0	0	0	0
	39	0	0	62.0	0	0	0
	40	0	0	102.0	0	0	0
	41	0	0	142.1	0	0	0
	42	0	0	182.1	0	0	0
Fz(-)	43	0	0	0	0	0	0
	44	0	0	-2.0	0	0	0
	45	0	0	-22.0	0	0	0
	46	0	0	-42.0	0	0	0
	47	0	0	-62.0	0	0	0
	48	0	0	-82.0	0	0	0
	49	0	0	-122.0	0	0	0
	50	0	0	-162.0	0	0	0

Table E.3: Pure moments load cases

Load Case	Load Step	Fx [N]	Fy [N]	Fz [N]	Mx [N.m]	My [N.m]	Mz [N.m]
Mx(+)	51	0	0	0	0	0	0
	52	0	0	0	0.2	0	0
	53	0	0	0	2.2	0	0
	54	0	0	0	4.2	0	0
	55	0	0	0	6.2	0	0
	56	0	0	0	8.2	0	0
	57	0	0	0	12.2	0	0
	58	0	0	0	16.2	0	0
Mx(-)	59	0	0	0	0	0	0
	60	0	0	0	-0.2	0	0
	61	0	0	0	-2.2	0	0
	62	0	0	0	-4.2	0	0
	63	0	0	0	-6.2	0	0
	64	0	0	0	-8.2	0	0
	65	0	0	0	-12.2	0	0
	66	0	0	0	-16.2	0	0
My(+)	67	0	0	0	0	0	0
	68	0	0	0	0	0.2	0
	69	0	0	0	0	2.2	0
	70	0	0	0	0	4.2	0
	71	0	0	0	0	6.2	0
	72	0	0	0	0	10.2	0
	73	0	0	0	0	14.2	0
My(-)	74	0	0	0	0	0	0
	75	0	0	0	0	-0.2	0
	76	0	0	0	0	-2.2	0
	77	0	0	0	0	-4.2	0
	78	0	0	0	0	-6.2	0
	79	0	0	0	0	-10.2	0
	80	0	0	0	0	-14.2	0
Mz(+)	81	0	0	0	0	0	0
	82	0	0	0	0	0	0.2
	83	0	0	0	0	0	2.2
	84	0	0	0	0	0	4.2
	85	0	0	0	0	0	6.2
	86	0	0	0	0	0	8.2
	87	0	0	0	0	0	12.2
Mz(-)	88	0	0	0	0	0	0
	89	0	0	0	0	0	-0.2
	90	0	0	0	0	0	-2.2
	91	0	0	0	0	0	-4.2
	92	0	0	0	0	0	-6.2
	93	0	0	0	0	0	-8.2
	94	0	0	0	0	0	-12.2

Table E.4: Combined load cases

Load Case	Load Step	Fx [N]	Fy [N]	Fz [N]	Mx [N.m]	My [N.m]	Mz [N.m]
Fx(-) Fy(+)	95	0	0	0	0	0	0
	96	-1.0	4.9	0	0	0	0
	97	-1.0	5.9	0	0	0	0
	98	-11.0	15.9	0	0	0	0
	99	-11.0	25.9	0	0	0	0
	100	-21.0	35.9	0	0	0	0
	101	-21.0	45.9	0	0	0	0
Fx(-) Fy(-)	102	0	0	0	0	0	0
	103	-1.0	-4.9	0	0	0	0
	104	-1.0	-5.9	0	0	0	0
	105	-11.0	-15.9	0	0	0	0
	106	-11.0	-25.9	0	0	0	0
	107	-21.0	-35.9	0	0	0	0
	108	-21.0	-45.9	0	0	0	0
Fx(-) Fz(+)	109	0	0	0	0	0	0
	110	-1.0	0	1.0	0	0	0
	111	-11.0	0	11.0	0	0	0
	112	-11.0	0	21.0	0	0	0
	113	-21.0	0	31.0	0	0	0
	114	-31.0	0	41.0	0	0	0
	115	-41.0	0	61.0	0	0	0
Fx(-) Fz(-)	116	0	0	0	0	0	0
	117	-1.0	0	-2.0	0	0	0
	118	-11.0	0	-22.0	0	0	0
	119	-11.0	0	-42.0	0	0	0
	120	-31.0	0	-62.0	0	0	0
	121	-31.0	0	-102.0	0	0	0
Fz(-) Mx(+)	122	0	0	0	0	0	0
	123	0	0	-1.0	0.2	0	0
	124	0	0	-11.0	1.7	0	0
	125	0	0	-21.0	3.2	0	0
	126	0	0	-31.0	4.7	0	0
	127	0	0	-41.0	6.2	0	0
	128	0	0	-51.0	7.7	0	0
	129	0	0	-61.0	9.2	0	0
Fz(-) Mx(-)	130	0	0	0	0	0	0
	131	0	0	-1.0	0.2	0	0
	132	0	0	-11.0	-1.7	0	0
	133	0	0	-21.0	-3.2	0	0
	134	0	0	-31.0	-4.7	0	0
	135	0	0	-41.0	-6.2	0	0
	136	0	0	-51.0	-7.7	0	0
	137	0	0	-61.0	-9.2	0	0
Fx(-) Mz(+)	138	0	0	0	0	0	0
	139	0.0	0	0	0	0	0.0
	140	-10.0	0	0	0	0	1.5
	141	-20.0	0	0	0	0	3.0
	142	-30.0	0	0	0	0	4.5
	143	-30.0	0	0	0	0	7.5
Fx(-) Mz(-)	144	0	0	0	0	0	0
	145	0.0	0	0	0	0	0.0
	146	-10.0	0	0	0	0	-1.5
	147	-20.0	0	0	0	0	-3.0
	148	-30.0	0	0	0	0	-4.5
	149	-30.0	0	0	0	0	-7.5
Fx(-) Fz(+) My(+)	150	0	0	0	0	0.0	0
	151	-1.0	0	1.0	0	0.2	0
	152	-11.0	0	11.0	0	1.7	0
	153	-21.0	0	21.0	0	3.2	0
	154	-31.0	0	31.0	0	4.7	0
	155	-41.0	0	51.0	0	7.7	0
	156	-51.0	0	71.0	0	10.7	0
Fx(-) Fz(+) My(-)	157	0	0	0	0	0.0	0
	158	-1.0	0	1.0	0	-0.1	0
	159	-11.0	0	11.0	0	-1.1	0
	160	-11.0	0	21.0	0	-2.1	0
	161	-11.0	0	31.0	0	-3.1	0
	162	-21.0	0	41.0	0	-4.1	0
	163	-21.0	0	51.0	0	-5.1	0
	164	-21.0	0	71.0	0	-7.1	0
Fx(-) Fz(-) My(+)	165	0	0	0	0	0.0	0
	166	-1.0	0	-1.0	0	0.1	0
	167	-11.0	0	-11.0	0	1.6	0
	168	-21.0	0	-21.0	0	3.2	0
	169	-31.0	0	-31.0	0	4.7	0
	170	-41.0	0	-51.0	0	7.7	0
	171	-51.0	0	-71.0	0	10.7	0
Fx(-) Fz(-) My(-)	172	0	0	0	0	0.0	0
	173	-1.0	0	-1.0	0	-0.1	0
	174	-11.0	0	-11.0	0	-1.1	0
	175	-11.0	0	-21.0	0	-2.1	0
	176	-11.0	0	-31.0	0	-3.1	0
	177	-21.0	0	-41.0	0	-4.1	0
	178	-21.0	0	-51.0	0	-5.1	0